Tests of Perturbative and Non-Perturbative QCD from Identified Proton, Kaon and Pion Studies in Deep Inelastic Scattering *ep* Interactions at HERA

Glen R. White *MPhys.(Hons.)*
Department of Physics, Lancaster University

This thesis is submitted in part fulfillment
of the requirements for the degree of Ph.D
from Lancaster University.

No part of this thesis has been, or will be,
submitted to any other university.

November 14, 2000

Abstract

Measurements of kaons, pions and protons identified using the dE/dx technique have been made in deep-inelastic scattering ep interactions at HERA in the kinematic range $5 < Q^2 < 70$ and $10^{-5} < x < 10^{-2}$. Tests of QCD were made possible through the production of transverse momenta and pseudo-rapidity spectra with comparisons made to ARIADNE and LEPTO Monte Carlo models, utilising the JETSET hadronisation model with tuning taken from DELPHI experiments, and with HERWIG using the cluster fragmentation model. Further measurements were made of the proton-antiproton asymmetry $A_B = \frac{2.(N(p)-N(\bar{p}))}{N(p)+N(\bar{p})}$ and compared to measurements made elsewhere using photo-production data and recent theoretical results. A search for QCD instanton induced events was also made using the kaon and pion sample. Results from kaon and pion spectra show a preference for the ARIADNE model with the DELPHI tuned JETSET parameters. Models with the DELPHI tuning are preferred over LUND default values, which includes a lower than default value for the strangeness suppression parameter $\lambda_s = 0.23$. None of the Monte Carlo models tested agreed with the proton and antiproton measurements, all over-estimating the measured yields. The proton-antiproton asymmetry was found to be zero within experimental errors, in the kinematical range of the measurements. An excess in strange particle yield over standard DIS background was found in a set of events selected for their instanton-like properties, although not statistically significant enough to draw firm conclusions.

To my wife, Denise, and to my family. Thank you all for your support.

“Those to whom everything is clear are unhappy people.”

- Louis Pasteur

Contents

List of Figures

List of Tables

Acknowledgements

Firstly, I would like to thank the Lancaster University HEP group for giving me the opportunity to study for this PhD in the first place. I would especially like to thank Terry Sloan, my supervisor, and Rob Henderson for their patient help and guidance throughout my years at Lancaster, and for putting up with no end of stupid questions! Also, thanks go to the whole HEP group, most of whom I have had contact with in some form or other. Especially, thanks to Alex and Rob for keeping the computer network operational, and Tim for his help with some statistical questions.

An especially big thank you to Dave Milstead for his great guidance and patience, without which I may well have been still sat at DESY looking bemused in front of a computer screen to this day! I would also like to thank all who helped me during my stays at DESY, especially those in the Energy Flow and Spectra working group for listening to and commenting on my work over the years.

Good luck to Gareth (keep on having it large!), Nick (don't get lost on your way around the World!), Paul 'Raging' Buck (you'll get there eventually!) and the Daves. Thanks for a truely messy few Lancaster years! God Bless, and get Jiggy with it ...

I also better mention the DESY boys, without which I may have come back to the UK a whole lot earlier and with money; 'Pies' Dave, 'Mike' Mike and 'and another thing' Jon.

Many thanks to my wife, Denise for putting up with me over the last few years and my frequent trips everywhere. Also, many thanks for reading this thesis and correcting my terrible English! Thanks also to my Mother and Father for your love and support, and to my Sister- best of luck for your upcoming degree course.

Lastly, but not leastly, I must thank the Particle Physics and Astronomy Research Council (PPARC) for their financial support.

Preface

The purpose of this thesis was to use the newly available (at the time of writing) calibrated dE/dx information to identify charged kaons, pions and protons passing through the central tracking region of the H1 detector in deep-inelastic ep scattering events. Through differentially plotting spectra of these particles, tests of QCD are carried out through the comparison with QCD Monte Carlo models.

The kaon and pion results allow comparisons of different QCD parton evolution models, as well as tests of the fragmentation process; in particular of the strangeness suppression factor as utilised in the JETSET fragmentation model. Through the addition of further cuts developed elsewhere, a search for QCD instanton induced events is also performed using these identified kaon and pion samples.

The proton selection allows the testing of baryon production in these interactions. In particular, it allows the possibility of looking at potential proton-antiproton asymmetries where none is naively expected, many units of rapidity away from the proton fragmentation region.

Chapter one looks at the physics underpinning the analysis. i.e. that of the deep-inelastic lepton-proton scattering process and the theory that describes it. It also outlines the mechanisms proposed to be responsible for the production of kaons, pions and protons in the hadronic final state. Chapter two outlines the workings of the H1 detector within the HERA collider and the various subdetectors necessary for this analysis. Chapter three describes the dE/dx technique and the calibration work that has been done to allow it to be used. Chapter four details the selection procedure for events and tracks used in the analysis, whilst chapter five gives the physics results and chapter six the instanton search results. Conclusions are presented in chapter 7.

Chapter 1

Physics at HERA

The experimental environment at H1 involves the collision of counter-rotating beams of electrons or positrons and protons. This analysis is concerned with the strong interaction of the beam constituents and the hadronic final state of those interactions.

The H1 detector at HERA is described in Chapter 2. In this chapter, the relevant theoretical framework for this analysis is discussed.

1.1 The Theory Of Deep Inelastic Scattering

The dominant process at H1 is that of photo-production [1], where the beam lepton radiates a quasi-real photon which then interacts with the proton. Within QCD framework, the photon couples either directly with a parton in the proton or indirectly via the photon's own parton content. The first type of interaction is known as direct photo-production (figure 1.1a), while the second is referred to as resolved photo-production (figure 1.1b).

The framework for this analysis, however, is provided by the theory of Neutral Current Deep Inelastic Electron Scattering (DIS)[1]. Detailed reviews of the

---

[1] Unless otherwise stated, the generic term electron is also taken to mean positron

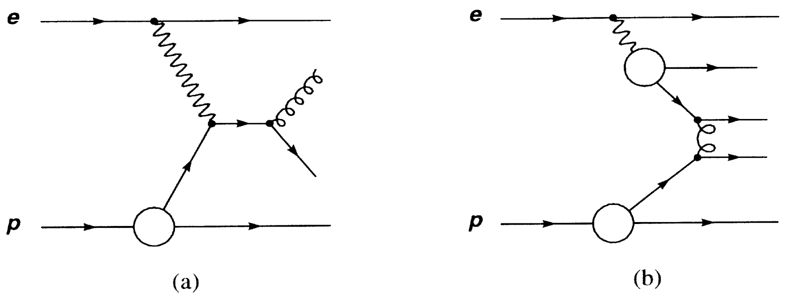

Figure 1.1: *Photo-production in lepton-proton scattering, (a)direct and (b) resolved processes shown.*

theoretical aspects of DIS are available, in for example [2]. Here, aspects of the theory are discussed such that the measurements presented in this analysis can be understood.

1.1.1 DIS Kinematic Variables

The simplest tree-level diagram for electron-proton DIS is shown in figure 1.2. The kinematics of this process can be described by two independent variables for

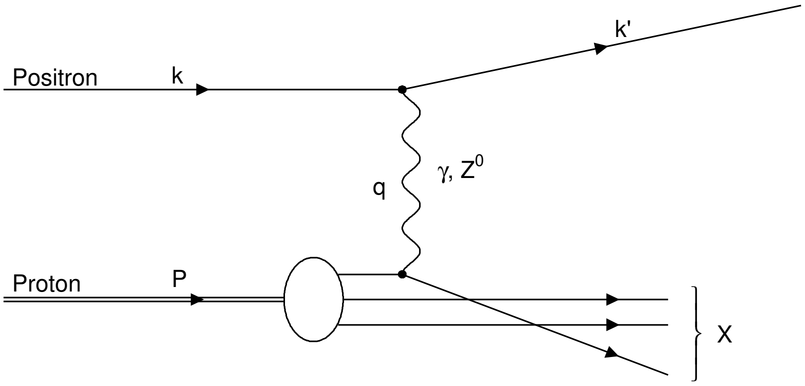

Figure 1.2: *Basic Deep Inelastic Scattering Picture.*

a fixed centre of mass energy $\sqrt{s}$. These are chosen from; Q^2, the negative four-momentum transfer squared between the incoming and outgoing lepton, which is also the invariant squared mass of the virtual exchanged boson and gives the probing power of the photon on the proton; x_{Bj} (Bjorken x), which is a dimensionless variable associated with the fraction of the incident proton momentum carried off by the struck parton in the quark parton model (see later); y_{Bj} is the fraction of energy transferred from the incident electron to the hadronic system in the proton rest frame; both x_{Bj} and y_{Bj} are confined to the range 0-1.

From the four-vectors of the incoming electron (k) and the proton (P), the centre of mass energy squared can be obtained thus:

$$s = (P + k)^2 \tag{1.1}$$

The kinematic variables are thus defined as:

$$\begin{aligned} Q^2 &= -q^2 = -(k - k')^2 && (1.2) \\ x &= \frac{Q^2}{2P.q} && (1.3) \\ y &= \frac{P.q}{P.k} && (1.4) \end{aligned}$$

where, k is the 4-momentum of the incident lepton, k' is the 4-momentum of the scattered lepton, q is the 4-momentum of the exchanged boson and P is the 4-momentum of the incident proton.

The invariant mass squared of the outgoing hadronic system is given by:

$$W^2 = (q + P)^2 \tag{1.5}$$

Neglecting the lepton and nucleon masses, the following relations hold:

$$Q^2 \approx sxy, \qquad W^2 \approx Q^2 \left(\frac{1-x}{x} \right), \qquad s \approx 4E_eE_p \tag{1.6}$$

Experimentally, the kinematics can be determined by either the electron alone, or from the measured hadronic system alone, or from a combination of both. In this analysis, the electron method is used. It can be shown from the above equations:

$$y_e = 1 - \frac{E'_e}{E_e} sin^2 \frac{\theta_e}{2}, \qquad Q^2_e = 4E'_eE_e cos^2 \frac{\theta_e}{2} \tag{1.7}$$

where, E_e and E'_e are the energies of the incident and scattered lepton respectively and θ_e is the scattering angle with respect to the proton beam direction, x can then be obtained from 1.6.

1.1.2 The Deep Inelastic *ep* Scattering Cross-Section

The fundamental process of DIS as shown in figure 1.2 is:

$$e \ + \ P \rightarrow e' \ + \ X \tag{1.8}$$

where e and e' are the incoming and scattered electron respectively, P is the incoming proton and the hadronic final state resulting from the DIS process is represented by X.

Here, the scattering takes place via the exchange of either a virtual photon or Z^0 boson. This is known as a neutral current (NC) process. Charged current (CC) processes also occur, where the exchanged boson is a $W^{\pm}$, although it is only the NC processes that are considered in this analysis. The NC cross-section is:

$$\sigma_{NC} = \sigma(\gamma) + \sigma(Z^0) + \sigma(\gamma Z^0) \tag{1.9}$$

The Z^0 and γZ^0 interference term only becomes significant at high Q^2 values. At relatively low values of Q^2 (compared to the Z^0 mass squared) studied in this analysis, these terms are highly suppressed.

The differential cross-section can now be written in terms of the two independent structure functions $F_1(x, Q^2)$ and $F_2(x, Q^2)$ [2]:

$$\frac{d^2\sigma_{ep}^{NC}(x, Q^2)}{dxdQ^2} = \frac{4\pi\alpha^2}{xQ^2}\left[xy^2F_1(x, Q^2) + (1-y).F_2(x, Q^2)\right] \tag{1.10}$$

here α is the electromagnetic coupling constant.

The two structure functions F_1, F_2 are required for the independent contributions from the absorption of transversely (σ_T) and longitudinally (σ_L) polarised virtual photons. $F_1(x, Q^2)$ describes σ_T while $F_2(x, Q^2)$ describes the sum $\sigma_T + \sigma_L$.

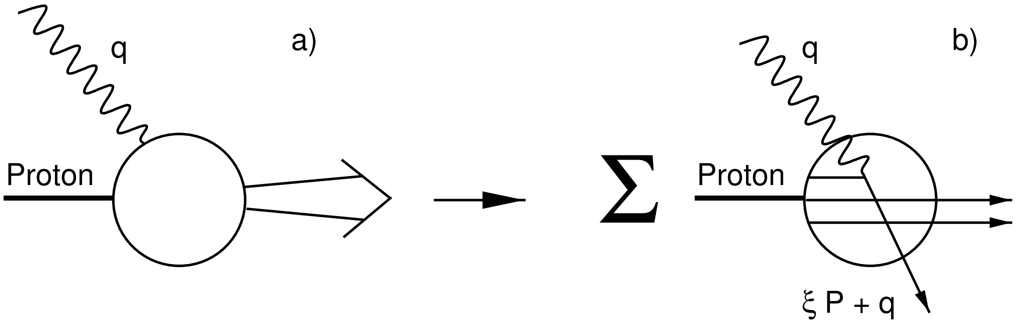

Figure 1.3: *The quark-parton model.*

The following longitudinal structure function $F_L(x, Q^2)$ and the ratio R are also commonly used:

$$F_L = F_2 - 2xF_1, \qquad R = \frac{F_L}{F_2 - F_L} = \frac{\sigma_L}{\sigma_T} \tag{1.11}$$

1.1.3 The Quark-Parton Model

The first experiments investigating DIS found that the structure function $F_2(x, Q^2)$ was independent of Q^2 for fixed x values. This scaling behaviour is known as Bjorken scaling and was interpreted as evidence that the proton consisted of point like 'partons'. These partons were then taken to be equivalent to the quarks introduced by Gell-Mann to explain the structure of hadrons [3].

The quark-parton model (QPM) was introduced by Feynman [4] to interpret this scaling behaviour of the structure functions, and was based on the following assumptions:

1. The hadron involved in the DIS process is constructed of quarks travelling in the direction of the hadron, with the momentum shared amongst them.
2. The interaction of photon-hadron is thus expressed as the sum of incoherent scatterings from the point-like quark constituents (figure 1.3).

Important results that are obtained from the QPM are:

1. The QPM provides a simple relationship between the structure functions and the parton density functions $f_i(x)$ which can be understood as the probability of finding a quark of flavour i in the proton with momentum fraction given by x_{Bj}.

$$\frac{F_2(x)}{x} = 2.F_1(x) = \sum_i e_i^2 f_i(x) \tag{1.12}$$

   where e_i is the charge of quark flavour i.

2. The structure functions do not depend on Q^2, only on x, which was consistent with predictions made by Bjorken and by measurements taken at SLAC [5].

3. The Callen-Gross relation:

$$F_2(x) = 2xF_1(x) \tag{1.13}$$

   which is a consequence of the spin 1/2 nature of quarks and is only valid for the case where quarks are the only constituents of the proton. From 1.13, the results $R = 0$ and $F_L = 0$ are obtained.

More recent measurements in DIS covering larger ranges of Q^2 have shown that the QPM cannot be the whole story however. For example, if quarks and anti-quarks are the only constituents of the proton, then their momenta fractions should add up to unity, where in actuality:

$$\sum_q \int_0^1 x(q(x) + \bar{q}(x))dx \simeq 0.5 \tag{1.14}$$

i.e. quarks only carry approximately half of the momentum of the proton as seen in DIS. The rest is carried by gluons in the framework of quantum chromodynamics.

1.1.4 DIS in Quantum Chromodynamics

The evidence for existence of other constituents of the proton apart from the quarks, as indicated by the deviation from unity in eq. 1.14 was also backed up by more recent measurements of F_2. With larger ranges of Q^2 available, it was soon seen that F_2 also depends upon Q^2 at smaller and larger values of x than previously reachable. This indicates that the scaling behaviour of the structure functions is violated (see figure 1.4).

The QPM is clearly not the whole truth, then, when dealing with DIS reactions involving the proton. Current models use the theory of quantum chromodynamics (QCD), which doesn't suffer from the above problems. The key aspects of this theory are outlined below:

- In addition to electric charge, quarks carry a colour charge (red, green, blue) which is the charge of the strong interaction.
- The gluon is the mediator of the strong force, of which there are eight bi-coloured varieties having spin 1 and zero electric charge.
- The quark-gluon colour interactions are computed by rules analogous to that of QED, with the substitution of $\sqrt{\alpha}$ for $\sqrt{\alpha_s}$ at each vertex and the introduction of colour factors.
- Unlike QED, the gauge bosons of this theory, the gluons, are able to interact with other gluons as they themselves carry colour charge.

Because of the self-coupling nature of the gluons in QCD, unlike QED, an anti-screening effect is present as a result of vacuum polarisation around a colour charge. This means that the closer one probes this charge, the less strong it appears to be.

When cross-sections are calculated within the QCD framework, integrals over the phase space of all quarks and gluons are found to diverge. A method to leave out these divergent parts of the integrals, called regularisation, is used. The re-calculated cross-sections become dependent on the energy scale μ_r^2 used in the regularisation. Renormalisation compensates for this unphysical effect by using an effective coupling constant and effective masses which absorb the divergent

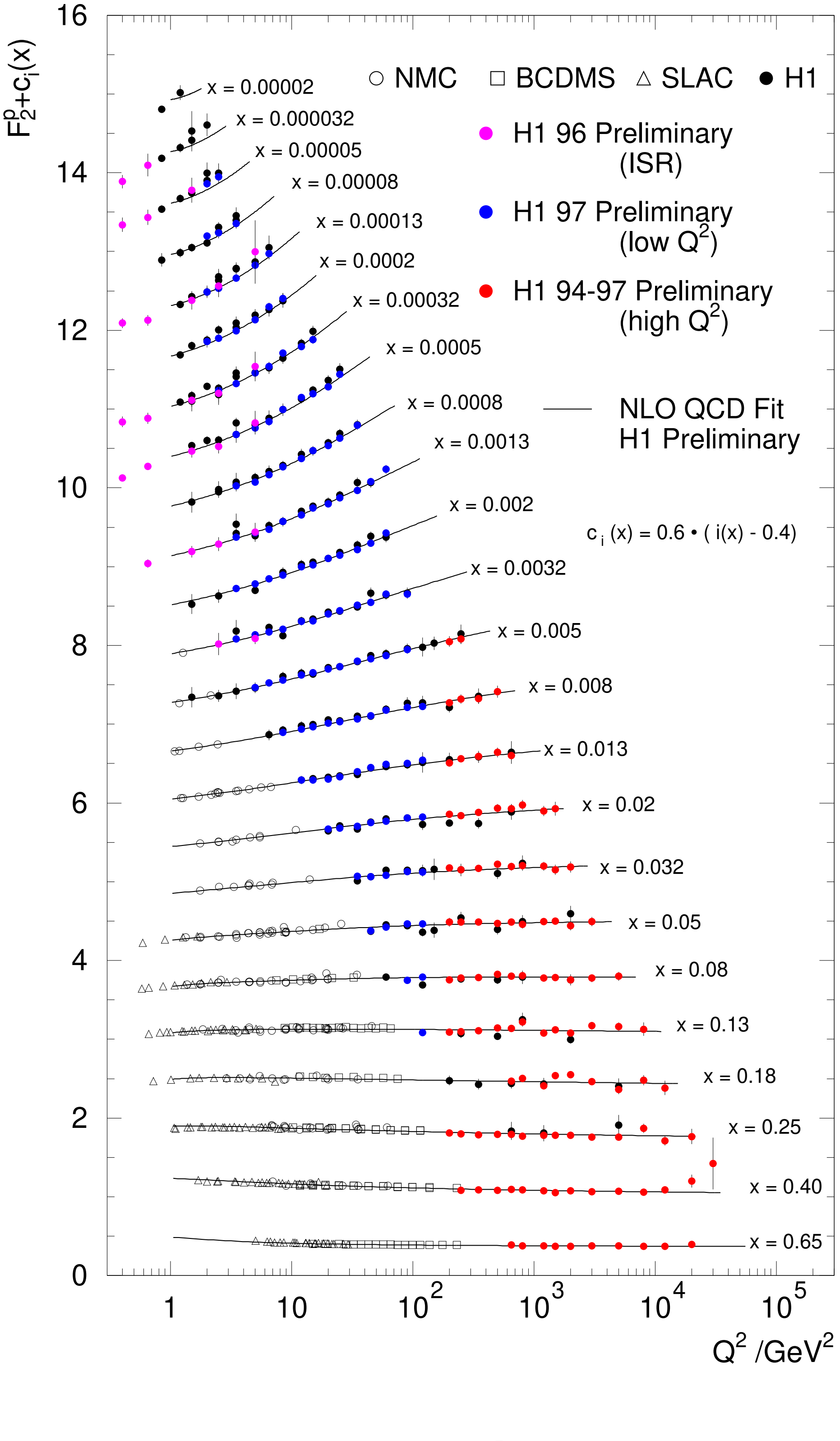

Figure 1.4: *The Proton structure function* $F_2^P(x, Q^2)$ *from H1 and from fixed target experiments [6].*

contributions. The coupling constant α_s is then dependent on the scale μ_r^2 known as the renormalisation scale. In DIS, this scale is set by the virtuality of the photon Q^2, and to first order, the coupling constant can be written as:

$$\alpha_s(Q^2) = \frac{12\pi}{(33 - 2N_f)ln(Q^2/\Lambda^2)} \tag{1.15}$$

where, N_f is the number of quark flavours and Λ is a free parameter only determinable experimentally. Λ governs the dependence of α_s on energy and marks the scale that calculable, perturbative QCD breaks down. Or, put another way, it represents the boundary between dealing with quarks and gluons and the world of physically measurable hadrons.

1.1.5 The Proton Structure In QCD

Gluon emission from quarks in QCD extends the QPM picture of the proton which can be viewed as the lowest order QCD process. Unlike before in the QPM picture, with QCD, the fractional momentum sum (equation 1.14) no longer deviates from unity. The missing momentum is carried by the electrically uncharged gluons.

The violation of Bjorken-scaling at high and low x is explained in terms of the ability of gluons to split into $q\bar{q}$ pairs. More and more of these fluctuations can be resolved with increasing Q^2 (shorter wavelength of photonic probe). Hence, with increasing Q^2, a depletion of quarks at large x and a corresponding enhancement at smaller x is seen (figure 1.5). It is actually the gluon content that governs the proton at low x, giving rise to the DIS cross-section via $q\bar{q}$ pair creation.

1.1.6 QCD Evolution Equations

Extending the structure of the proton to include QCD effects does of course mean that the relation in equation 1.12 no longer holds.

A more general formulation of the structure functions using the idea of fac-

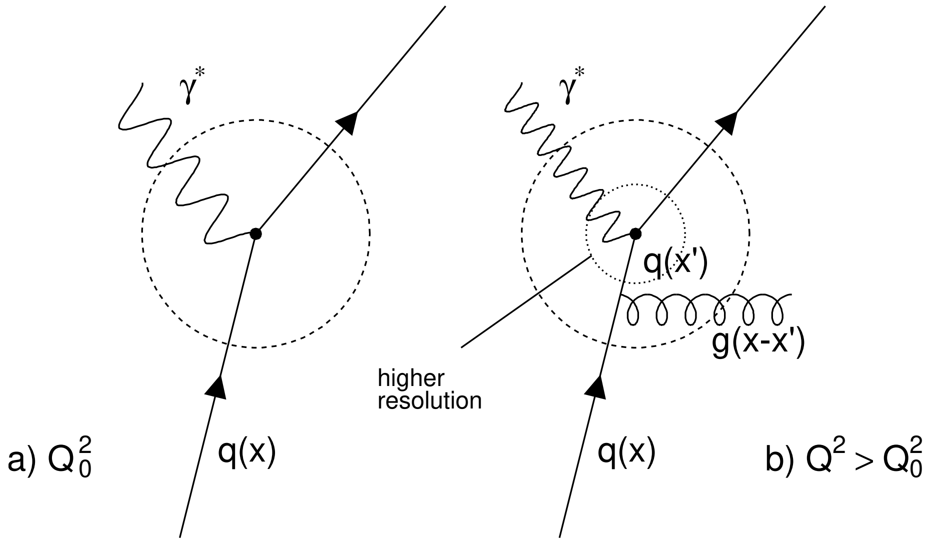

Figure 1.5: *Scaling violations: the photon can see more partons in (b) which carry a smaller fraction of the proton's momentum*

torisation to separate long and short range processes is:

$$F_2(x, Q^2) = \sum_{i=q,g} \int_x^1 d\xi C_i^V \left(\frac{x}{\xi}, \frac{Q^2}{\mu_r^2}, \mu_f^2, \alpha_s \right) .q_{i,h}(\xi, \mu_r^2, \alpha_s), \tag{1.16}$$

here, the sum encompasses all quark and gluon densities. C_i^V are the coefficient functions for each type of parton i and exchanged boson V (the virtual photon in this case), it does not depend upon the type of hadron involved. The factorisation scale μ_f^2 defines the point of separation between long and short range phenomena (figure 1.6). If the relevant scale (here, Q^2) is larger than μ_r^2, this process is calculable in perturbative QCD; whereas everything below this is absorbed into the parton densities $q_{i,h}$. These parton densities are specific to the hadron involved, h, but independent of the hard subprocess under consideration and are known as 'universal parton densities'.

Since these equations can, so far, not be solved exactly, several approximations of QCD are commonly used which are valid in different regions of phase-space. In the perturbative expansion, terms of the form $(\alpha_s ln(Q^2/Q_0^2))$, $(\alpha_s ln(1/x))$ and mixed terms $(\alpha_S ln(Q^2/Q_0^2)(ln(1/x)))$ appear. In the DGLAP

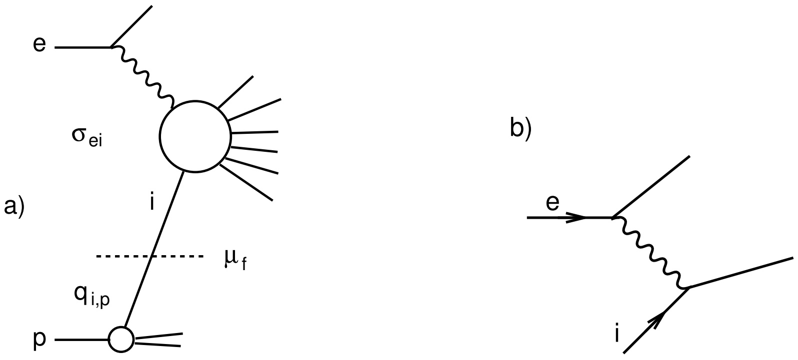

Figure 1.6: *(a) The ep cross-section factorised into lepton-parton cross-sections σ_{ei} and parton densities $q_{i,p}$. (b) Lowest order diagram contributing to σ_{ei} in (a)*

scheme, $(\alpha_s ln(1/x))$ terms are neglected, while the BFKL approach takes these terms to be dominant over the $(\alpha_s ln(Q^2/Q_0^2))$ terms used in the DGLAP approximation. The mixed terms start to become important as x decreases where Q^2 remains not too small.

1.1.7 DGLAP Evolution

In the region of large Q^2, the evolution of the quark and gluon densities is approximated by the DGLAP (Dokshitzer, Gribov, Lipatov, Altarelli, Parisi) evolution equations [7].

These are written in terms of quark and gluon splitting functions $P_{i,j}(z)$, which are calculable by perturbative expansion. These give the probability for the parton branchings $q \rightarrow qg$, $g \rightarrow q\bar{q}$, $g \rightarrow gg$, where the daughter parton i carries a fraction $(1-z)$ of its mothers (j) momentum (see figure 1.7).

The DGLAP equations are obtained using the leading log approximation (LLA) where in leading order α_s, the dominant contributions are $(\alpha_s ln(Q^2/Q_0^2))^n$ terms summed for all orders of n. Dokshitzer [7] showed that this is equivalent to the sum of ladder graphs as shown in figure 1.8. Important consequences of

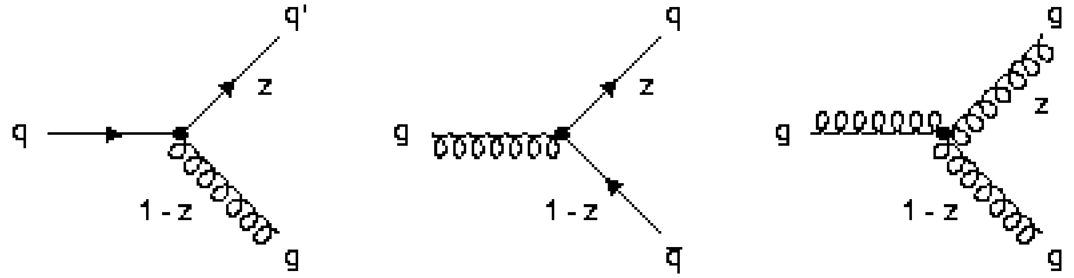

Figure 1.7: *The Feynman graphs for the splitting functions* (P_{qg}, P_{gq}), P_{qq} *and* P_{gg}

this scheme are, that in this gluon ladder:

- The transverse momenta $k^2_{T,i}$ of the emitted partons are strongly ordered such that, $k^2_{T,i} \ll k^2_{T,i+1} \ll \ldots \ll Q^2$.
- The longitudinal momenta x_i of the emitted partons satisfy $x_i \gg x_{i+1} \gg \ldots \gg x$.

The applicable region for the LLA is given by the use of perturbation theory ($\alpha_s(Q^2) \ll 1$) and by neglecting $ln(1/x)$ terms.

When moving towards smaller x, where contributions from $\alpha_s ln(1/x)$ and $\alpha_s ln(1/x) ln(Q^2/Q_0^2)$ become important, the LLA ceases to be valid. In this case, the Double LLA (DLLA) can be used. Here, in addition to the strong ordering in $k^2_{T,i}$, the longitudinal momenta of the emitted partons are also required to be strongly ordered: $x_i \gg x_{i+1} \gg \ldots \gg x$.

1.1.8 BFKL Evolution

In the region where x becomes small, but where Q^2 is not large enough for the DLLA to be valid, the DGLAP approximations cannot be used. Here, the BFKL (Balitsky, Fadin, Kuraev, Lipatov) equation [8] is used which sums diagrams leading in $ln(1/x)$ and independent of $ln(Q^2)$. With BFKL, the gluon ladder need not be ordered in k_T. The gluon distribution, then, is not integrated over

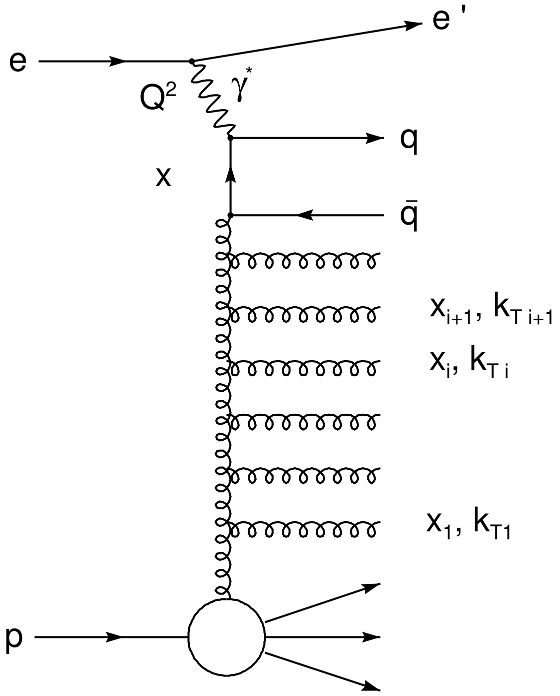

Figure 1.8: *Parton evolution in QCD (ladder diagram).* x_i *and* $k_{T,i}$ *represent the gluon longitudinal and transverse momenta*

k_T.

The different scope of the BFKL evolution leads to an ordering scheme for the parton emissions in LL(1/x) which is very different from the DGLAP type ordering:

- The transverse momenta $k_{T,i}^2$ of the emitted partons are unordered. The parton emissions perform a random walk in k_T^2 space.
- The longitudinal momenta x_i of the emitted partons are strongly ordered: $x_i \gg x_{i+1} \gg \ldots \gg x$.

The fact that the BFKL evolution is not ordered in k_T leads to a diffusion of k_T^2 which can extend into the infra-red region. This is usually avoided by introducing a cut-off parameter k_0^2, below which gluon emissions are not allowed. A side effect of this is that the results obtained show a dependence on k_0^2.

1.2 QCD Models

Model predictions of QCD DIS events have two parts to them: perturbative calculations of short range processes, and the long range non-perturbative effects of hadronisation. Perturbative QCD makes predictions for the **partonic** final state with fixed order (α_s) calculations of the matrix elements, or with parton showers, or a combination of both. Hadronisation turns the partonic final state into the observable particles we measure in the detector. For this, QCD models implement either the string fragmentation model or the cluster fragmentation model.

1.2.1 Matrix Elements

The tree level diagrams in figure 1.9(b) are the basic, first order α_s matrix elements, modelling the upper part of the DIS process in 1.9(a) and form the cornerstone of the QCD calculations shown in this thesis. Up to now, beyond this only NLO(α_s) (including virtual corrections from loop diagrams) calculations have been made available which, for example, have been able to predict dijet production to NLO(α_s). Although specialised calculations have been performed to NLO with regards to the hadronic final state, for example see [9], [10], such models are still not in a widely available format.

1.2.2 Leading Logarithmic Parton Showers

Higher order effects can be approximated using the leading log parton cascade idea [11]. Here, the quark struck by the virtual photon may emit partons both before and after this vertex corresponding to initial and final state parton showers (see figure 1.10). The initial state showering can be initiated by a parton close to its mass shell in the incoming proton. In each branching, one parton becomes increasingly space-like and the other is on-shell or has a time-like virtuality. The

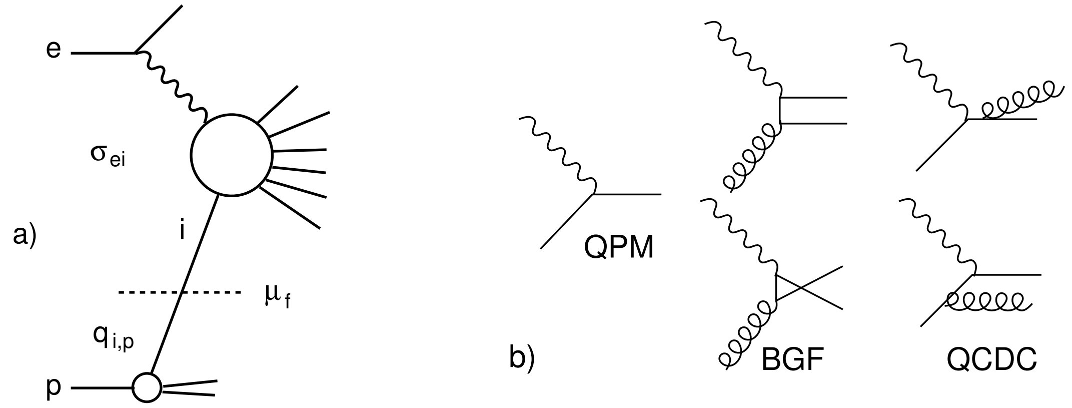

Figure 1.9: *Tree level diagram for ep scattering (b) contributing to σ_{ei} in (a).*

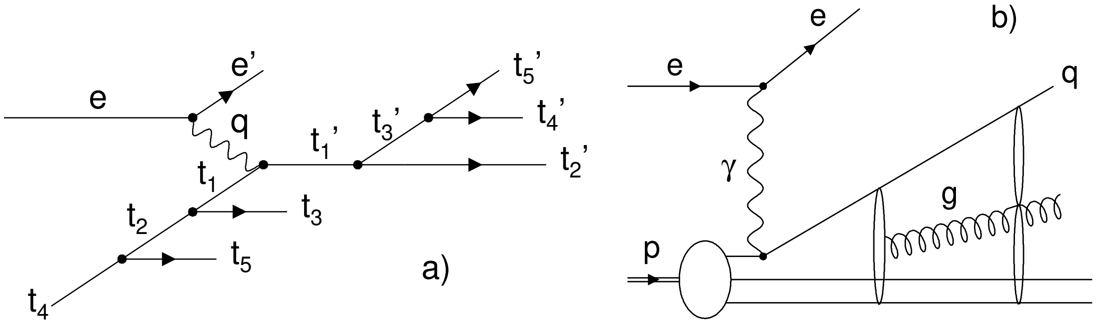

Figure 1.10: *The (a) Leading log parton shower and (b) colour dipole model in DIS*

initial state cascade results in a space-like quark interacting with the virtual photon. The outgoing quark is then either time-like or on-shell. If the outgoing quark is time-like, the off-shell mass is reduced by subsequent branching into daughter particles until all partons are on-shell.

These cascade processes are based on the branching described by the DGLAP splitting functions in the LL(Q^2) approximation of QCD (see section 1.1.7).

1.2.3 The Colour Dipole Model

The Colour Dipole Model [12] (CDM) gives an alternative description of parton showers by describing the gluon bremsstrahlung in terms of radiation from colour dipoles between partons (figure 1.10(b)).

Initially, a colour dipole is formed between the struck quark and the proton remnant. Subsequent gluon emission is formed between the newly created colour charges and the original ones. This is iterated until the available energy is used up. An additional complication arises from the fact that the proton, unlike its dipole partner, the struck quark, is an extended object. The CDM introduces a suppression factor here due to the fact that emissions of small wavelengths from an extended antenna are suppressed.

In the CDM, the boson-gluon fusion process (BGF, see figure 1.9) is not described at all and has to be inserted by hand.

The final gluon configuration in the CDM is unordered in k_T.

1.2.4 String Fragmentation

In the confinement picture of quarks, as a $q\bar{q}$ pair separates, a colour field dipole is formed between them. As the $q\bar{q}$ separation increases, so does the strength of the colour field. The colour field can be considered to be string-like with a constant energy density [13]. When the energy stored in the string (which in DIS can also form between struck quark and the proton remnant) is large enough, the string breaks up creating a new $q\bar{q}$ pair which forms new string pieces. This process iterates until the available energy is used up, with resulting string fragments combined into mesons and baryons (see figure 1.11). Gluons are realised as kinks in the string which receive the four-momentum of the gluon.

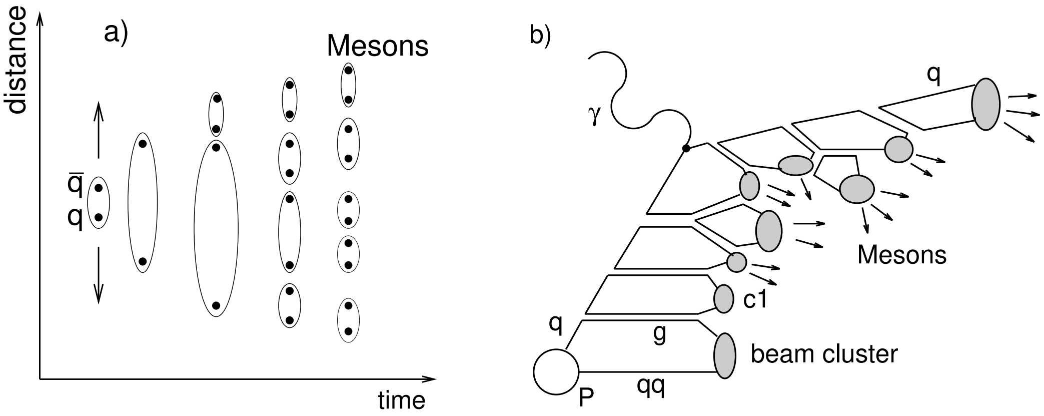

Figure 1.11: *Fragmentation models: (a) the string and (b) the cluster model*

1.2.5 Cluster Fragmentation

Colour singlets are formed from the perturbatively generated partons in the cluster fragmentation model [52]. Initially, all gluons are non-perturbatively split into $q\bar{q}$ pairs and combined into low mass colour neutral clusters. These clusters are taken to be superpositions of meson resonances and decay into mesons or baryons according to the available phase space (see figure 1.11).

1.3 Strangeness Production In DIS

In the DIS picture shown in figure 1.8, strange particles may be produced in different ways. A strange quark can be scattered out of the proton sea, or $s\bar{s}$ pairs can be created; either in BGF processes (shown in top part of figure 1.8) or during parton showering and hadronisation. Strange particles can also arise from heavy quark decays, or as discussed later, from non-standard processes like instantons.

Most of the strange particles are expected from hadronisation with small fractional energy. In the Lund hadronisation model, $q\bar{q}$ pairs are created in the colour field of the string from the vacuum. Here, $s\bar{s}$ production is suppressed with respect to the other light quarks as a consequence of their relative masses ($m_s > m_u \approx m_d$). This is normally expressed as the ratio $\lambda_s : 1 : 1$, where λ_s is known as the strangeness suppression factor. The Lund default value for λ_s is 0.3 which represents the experimental mean from [14] and the typical value seen in electron-positron annihilation and moderate to large x DIS experiments [15], [16].

1.4 Protons in DIS

The production of baryons away from the proton remnant region in the DIS picture shown in figure 1.8 occurs during the fragmentation process. This is a poorly understood area however. The simplest mechanism used in the Lund string model allows the introduction of a diquark in a colour anti-triplet state that can be treated like an ordinary antiquark in the string. The string can break by quark-antiquark or antidiquark-diquark pair production. The diquarks can then combine with a quark to form a baryon. A more complex scenario is the 'popcorn' model [23], in which diquarks are not produced and baryons appear from the successive production of several $q\bar{q}$ pairs.

At HERA, a net baryon number is present due to the beam proton. In collisions, the proton is disrupted and the majority of the momentum is carried by diquarks giving rise to leading baryon production in the forward proton fragmentation region. In this picture, which describes the bulk of the data studied on leading baryon production, baryon number transfer over large rapidity intervals is strongly suppressed.

There are a number of measurements however [24], [25], [26], [27] which are difficult to explain by this diquark picture. There are also some recent results from photo-production studies at H1 [28] in which there is evidence of a baryon asymmetry in events with large charged particle multiplicities several units of rapidity away from the proton remnant.

A gluonic mechanism for the propagation of baryon number proposed some 25 years ago [29], [30] is discussed in a recent paper [31] with reference to the recent H1 preliminary results. The gluonic mechanism discussed in [31] successfully predicts the results shown in [28], and is predicted to be valid in the DIS regime also.

As mentioned, the dominant source of baryon production in the measurable region of phase space arises from the hadronisation of the DIS partonic state. DIS interactions at low values of x_{Bj} ($< 10^{-2}$; as in this analysis) are dominated by the gluonic content of the proton. This leads to an octet-anti-octet colour configuration of the partonic final state. Thus, the standard description in terms of a system of triplet strings is likely to be inadequate. In relation to this, baryon production could be expected to be heavily suppressed in hadronisation of an octet-anti-octet field [33].

1.5 Instantons at HERA

Strangeness production in DIS at HERA at levels above that predicted by the QCD picture discussed up to now is possible through the non-perturbative mechanism introduced by QCD instanton theory.

Instantons [17] introduce into the standard model processes which cannot be described by perturbation theory. In the case of electroweak interactions, baryon and lepton number is violated; and chirality is violated in the case of the strong interaction. As the name suggests, instantons are non-perturbative fluctuations confined to an ‘instant’ in space-time and have no corresponding free particle solutions for $t \rightarrow \infty$.

Unlike in electroweak theory where high energies ($\mathrm{O} \gtrsim 10TeV$) are required, in QCD, instantons are expected to play a role at energies accessible by today’s colliders. DIS at HERA is particularly interesting due to the hard scale for the instanton sub-process provided by the virtual photon probe Q^2. This is needed for theoretically sound predictions [18], [19], [20]. While instanton effects have not as yet been experimentally observed, their discovery would be of fundamental significance for particle physics.

1.5.1 Instanton Theory

Instantons originate from the topological structure of the vacuum in non-abelian gauge field theories. Figure 1.12 shows the structure of the vacuum, where neighbouring vacua have the same minimal potential energy and are separated by a potential barrier of height E_B. The vacua are labelled by their Chern Simons winding numbers N_{CS}, defined as an integral over the gauge fields A^a_μ with coupling g,

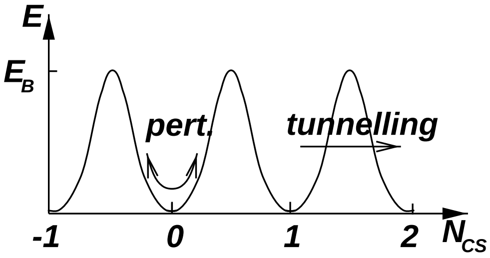

Figure 1.12: *The structure of the vacuum.*

$$N_{CS} = \frac{g^2}{16\pi^2}\int d^3x \epsilon_{ijk}(A^a_i \delta_j A^a_k - \frac{g}{3}\epsilon_{abc}A^a_i A^b_j A^c_k) \qquad (1.17)$$

Transitions between neighbouring minima in figure 1.12 are possible classically when the energy E is large enough $E > E_B$, or by quantum mechanical tunnelling when $E < E_B$. The latter corresponds to the instanton solutions of the classical field equations. This instanton induced tunnelling process has a transition amplitude which is exponentially suppressed $\propto exp(-4\pi/\alpha)$.

The barrier height in electroweak theory is given by $E_B \approx m_w/\alpha_w = \mathcal{O}(10TeV)$. Instanton transitions between vacua ΔN_{CS} apart violate baryon (B) and lepton

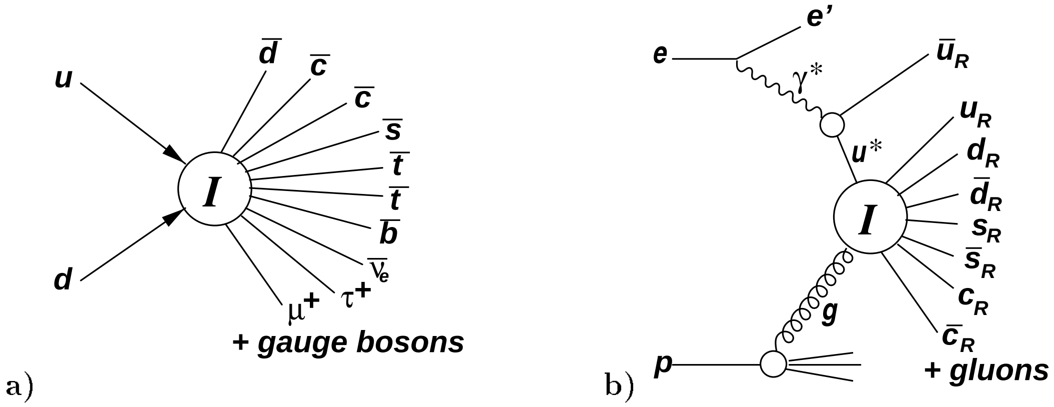

Figure 1.13: *instantons in a) the electroweak and b) the strong interactions.*

(L) numbers according to:

$$\Delta(B+L) = -2n_{gener}\Delta N_{CS}, \tag{1.18}$$

with the following conditions:

$$\Delta(B-L) = 0 \quad \Delta L_e = \Delta L_\mu = \Delta L_\tau = \Delta B/3, \tag{1.19}$$

$n_{gener} = 3$ being the number of fermion generations. Figure 1.13(a) shows an electroweak interaction with $\Delta(B+L) = -6$.

This kind of interaction may have played an important part in the early universe when energies were typically this high. Importantly, in this respect, instantons in the electroweak sector may have played a part in the setting of the asymmetry between matter and anti-matter.

Chirality is violated with instanton induced QCD reactions. Where chirality (Q_5) is the difference between the number of left- and right-handed fermions, $Q_5 = \#L - \#R$. For n_f active quark flavours, the selection rule is:

$$\Delta Q_5 = 2n_f.\Delta N_{CS} \tag{1.20}$$

Here, the hard scale of the process, e.g. $E_B = \mathcal{O}(Q)$ for DIS, selects the barrier height. Also, the exponential suppression is less than in the electroweak case because $\alpha_s \gg \alpha_w$.

1.5.2 Instantons in DIS

Events due to instantons I (and anti-instantons $\bar{I}$) in DIS are predominantly produced in a photon-gluon fusion process [19], [20] (figure 1.14):

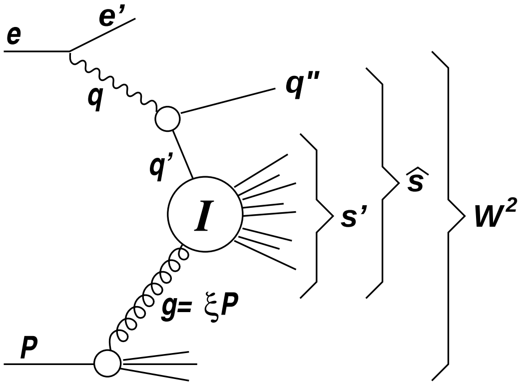

DIS variables:
$Q^2 := -q^2$
$x := Q^2 /(2P \cdot q)$
$W^2 := (q+P)^2 = Q^2 (1-x)/x$
$\hat{s} := (q+g)^2$
$\xi = x(1+\hat{s}/Q^2)$

Variables of instanton subprocess:
$Q'^2 := -q'^2$
$x' := Q'^2 /(2\, g \cdot q')$
$s' := (q'+g)^2 = Q'^2 (1-x')/x'$

Figure 1.14: *Kinematics of instanton induced processes in DIS*

$$\gamma^* + g \rightarrow^I \sum_{n_f} (\bar{q}_R + q_R) + n_g g \quad \gamma^* + g \rightarrow^{\bar{I}} \sum_{n_f} (\bar{q}_L + q_L) + n_g g \tag{1.21}$$

Quarks and anti-quarks of all n_f active flavours are found in each event as well as n_g gluons.

The kinematics of a DIS event with an instanton sub-process present is shown in figure 1.14. It can be seen that the instanton subprocess kinematics Q', x', s' are analogous to the standard DIS kinematic variables and are governed by the exchanged quark and gluon 4-momenta (q', g).

The instanton induced cross-section is given by a convolution of the probability to find a gluon in the proton, the probability that the virtual photon splits into a $q\bar{q}$ pair in the instanton background, and the cross-section of the instanton subprocess given by [20]:

$$\sigma^I_{q'g}(x', Q'^2) \approx \frac{\Sigma(x')}{Q'^2} \left(\frac{4\pi}{\alpha_s(\mu(Q'))} \right)^{\frac{21}{2}} .exp \left(\frac{-4\pi}{\alpha_s(\mu(Q'))} F(x') \right) \tag{1.22}$$

The cross-section depends critically on the functions $F(x')$ (called the 'holy grail' function), which modifies the exponent factor, and on $\Sigma(x')$, which depends on

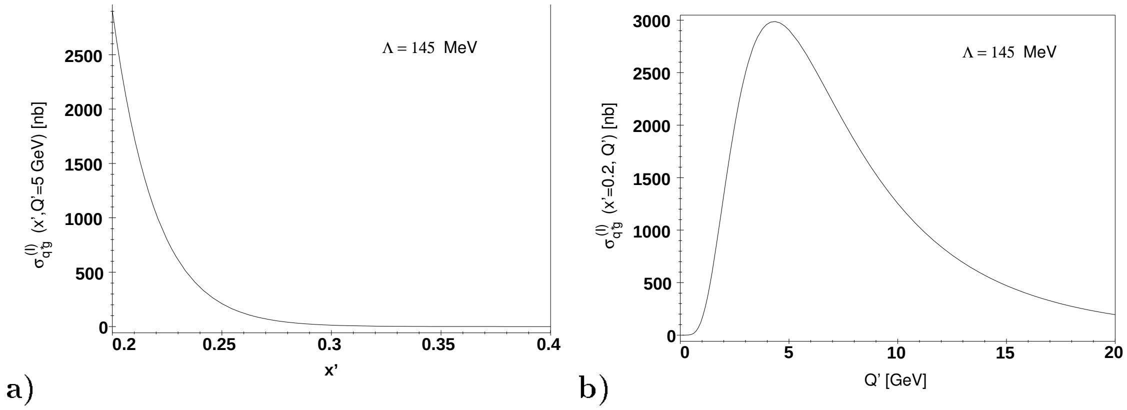

Figure 1.15: *The instanton cross-section as a function of a) x' for $Q' = 5GeV$ and b) Q' for $x' = 0.2$*

$F(x')$. There is also a scale dependence due to the choice of renormalisation scale $\mu(Q')$. $F(x')$ can be estimated reasonably well for x' not too small ($x' \gtrsim 0.2$) [20], the theory contains ambiguities below this. The cross-section grows towards low x' and is peaked at $Q' = 5GeV$ (see figure 1.15). In the more theoretically safe region $x' > 0.2$, the expected fraction of instanton events in all DIS events is of $\mathcal{O}(10^{-3} - 10^{-4})$.

Although the cross-section is subject to some uncertainties, the properties of the final states of instanton induced events are reliably calculable. Whilst the property of non-conservation of chirality is difficult to exploit experimentally, further properties allow for possible discovery signatures. Striking features of the hadronic final state would be present due to the fact that, in the $q'g$ rest frame, $2n_f - 1$ quark and anti-quarks and n_g gluons are emitted isotropically from the instanton subprocess. n_g follows a Poisson distribution, with [21], [22]:

$$< n_g > \approx \frac{2\pi}{\alpha_s} x'(1 - x') \frac{dF(x')}{dx'} \tag{1.23}$$

After hadronisation, this gives a high multiplicity spherical hadronic final state with the multiplicity depending on available centre of mass energy $\sqrt{s'}$. For a typical DIS kinematic event ($x' = 0.2$, $Q' = 5\ GeV \ \Rightarrow \ \sqrt{s'} = \ 10\ GeV,\ < n_g > = \mathcal{O}(2)$); about $n_p = 10$ partons and $n = 20$ hadrons would be expected.

Furthermore, with the decay into all kinematically allowed flavours of quark, another strong signature could be the excess of strange final state particles compared with the expected flux from DIS events.

Chapter 2

HERA and the H1 Detector

2.1 The HERA Collider

The **H**adron-**E**lectron-**R**ing-**A**ccelerator [34] at the **DESY** [35] facility in Hamburg is the first storage ring providing electron/positron-proton colliding beams. The two main accelerators providing these beams lie in a tunnel of circumference 6.3 km. They produce counter-rotating beams of 27.5 GeV (electrons) and 820 GeV (protons) giving a centre-of-mass energy of 300.3 GeV. The proton beam has now been upgraded to run at 920 GeV, an energy which it has run at since the start of the 1999 running period. During the 1996 and 1997 running periods considered in this analysis, positrons were used as the lepton beam.

HERA contains four interaction regions. H1 [36], situated in the North Hall and ZEUS [37] in the South Hall have been studying electron/positron-proton scattering events since 1992. HERA-B [38] (West Hall) uses tungsten wire targets inserted into the halo of the proton beam to study decay modes in the $B^0/\overline{B}^0$ system to investigate CP violation (this experiment started in 1999). Collisions of the positron beam operating in a polarised mode with a polarised gas target $(H_2, D,^3 He,^4 He)$ have been used by HERMES [39] (East Hall) since 1995 to study the origin of nucleon spin.

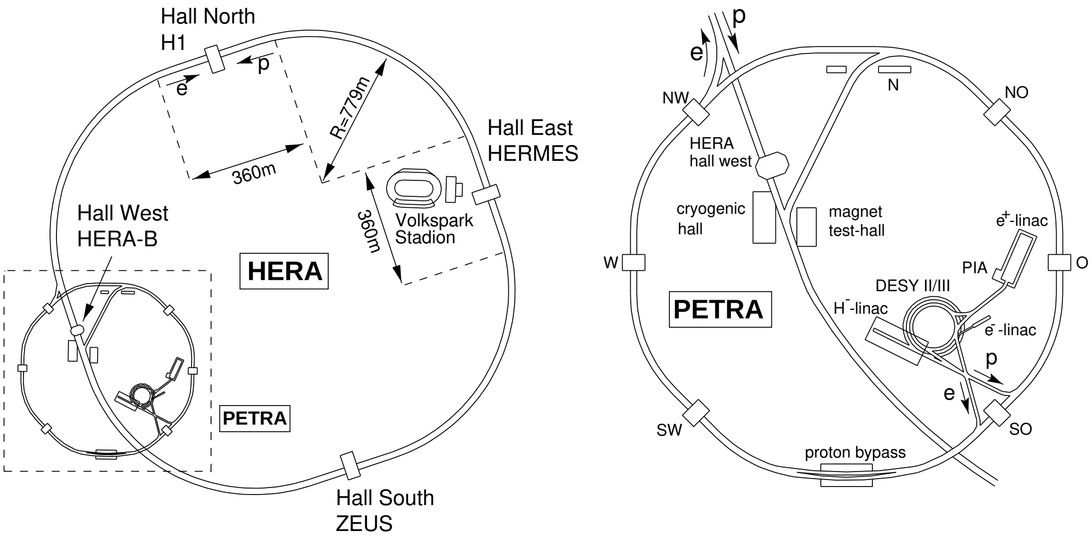

Figure 2.1: *The HERA collider.*

Figure 2.1 shows a schematic layout of the HERA accelerator complex. A chain of pre-accelerators (originally built for previous experiments) produces the electron/positron and proton beams at the required energy to inject into the main accelerators.

Using a 50 MeV linear accelerator, negatively charged hydrogen ions are stripped of their electrons and injected into DESY III. Here they are accelerated to 7.5 GeV before being transferred to PETRA. After a maximum of 70 bunches have been stored in PETRA, the protons are accelerated to 40 GeV and injected into HERA. Three iterations of this process are performed to complete a proton fill, leaving HERA with 210 proton bunches.

Electrons are accumulated and stored in a 60 mA single bunch from a 500 MeV linear accelerator. They are then fed into DESY II and accelerated to 7 GeV and transferred to PETRA (again with 70 bunches). PETRA accelerates the electrons to 11 GeV before injecting them into HERA. With the electrons, there are again 3 iterations of this procedure.

The proton beam is produced first in HERA and then ramped up to 820 GeV, then the electron beam is inserted and ramped to 27.5 GeV. Both beams are then optimised for maximum luminosity.

The electron beam was first replaced with positrons for the 1994 run. Positively charged ion clusters produced by getter pumps[1] had been found to reduce the lifetime of the beam. These ions are repelled by the positron beam, which therefore has a longer lifetime. Problems with the electron beam have been overcome lately, with electron beams included once more in the 1998 running period.

2.2 Overview of the H1 Detector

The H1 apparatus was constructed as a general purpose detector for ep collisions, based on a full coverage of the solid angle around the interaction point (with the exception of the beam holes).

From the isometric view of the H1 detector in figure 2.2, it can be seen that H1 is asymmetric in design. This is motivated by the asymmetric beam energies. The centre-of-mass frame is boosted with respect to the laboratory frame in the direction of the much more energetic proton beam (right to left in figure 2.2). As can be seen, the detector is considerably more massive and segmented in this region, where the highest particle and energy densities are expected.

H1 has the dimensions $12m \times 10m \times 15m$ approximately, and has a total weight of about 2800 tonnes.

The H1 detector is a group of devices providing complementary information on the various reaction products created at the interaction point. In the following sections, an overview is given of these components. A more detailed description is given in reference [36].

---

[1] Getter pumps maintain the high vacuum in the electron ring.

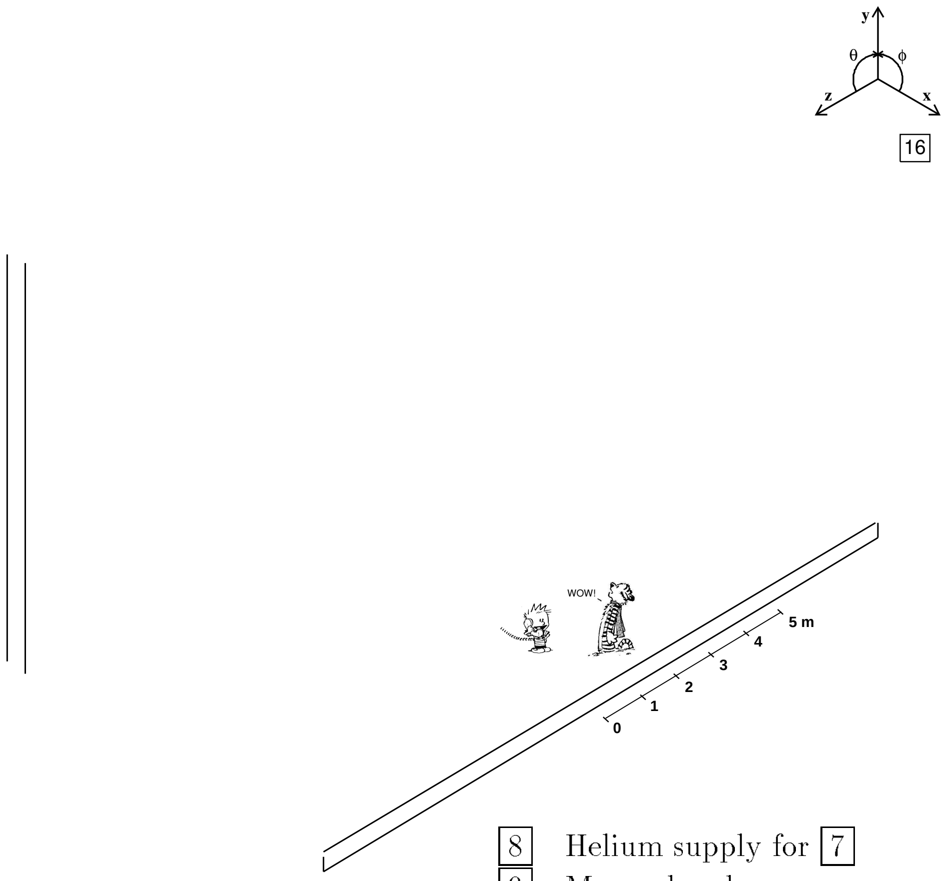

1	Beam pipe and beam magnets
2	Central track detectors
3	Forward track detectors
4	Electromagnetic LAr calorimeter
5	Hadronic LAr calorimeter
6	Superconducting coil (1.15 T)
7	Compensating magnet
8	Helium supply for 7
9	Muon chambers
10	Instrumented iron yoke
11	Forward muon toroid
12	SPACAL and Backward DC
13	PLUG calorimeter
14	Concrete shielding
15	Liquid argon cryostat
16	H1 coordinate system

Figure 2.2: *An isometric view of the H1 detector at HERA.*

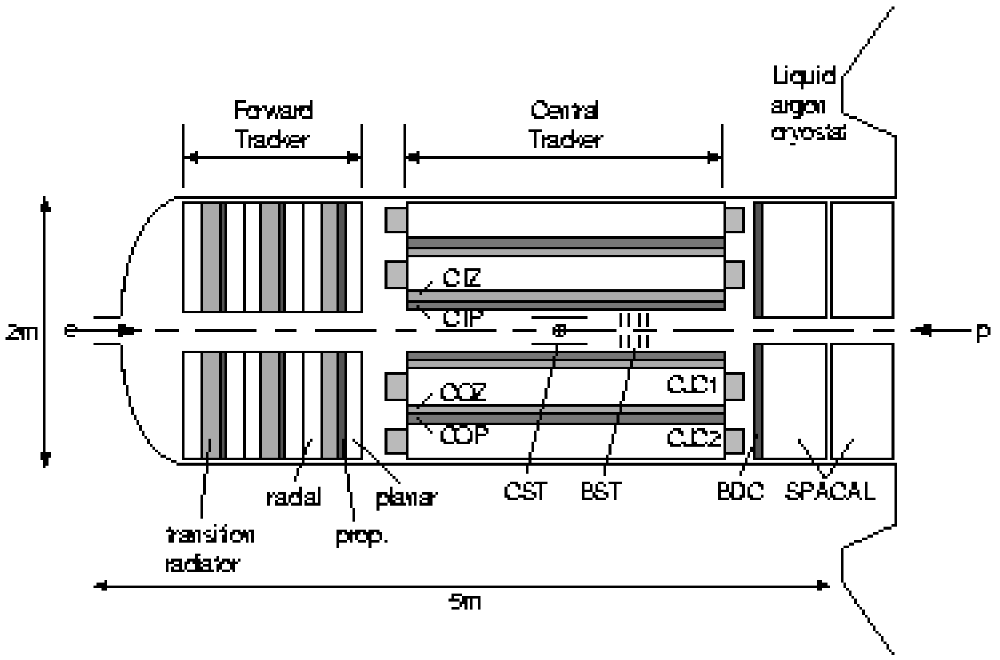

Figure 2.3: *The H1 tracking system.*

2.3 Tracking

The H1 tracking system (figure 2.3) is sub-divided into three major components: the central track detector (CTD), the forward track detector (FTD) and the backward drift chamber (BDC). Between them, the polar angular range from $5^o < \theta < 178^o$ is covered (with full azimuthal coverage).

It has been designed to cope with the high density particle environment whilst being able to reconstruct tracks with high efficiency and good momentum resolution. It also provides a trigger system for background rejection along with a fast event vertex determination.

The three major components are covered in more detail in the following sections. It should also be noted here that central and backward Si trackers also exist to provide tracking information close to the interaction region and for large polar angles respectively. However, no data from these devices is used in this analysis so they will not be discussed further here.

2.3.1 Central Track Detectors

The central tracking system of H1 is designed to detect tracks leaving the nominal interaction vertex over the polar angular range $25^o < \theta < 155^o$. The basis for the track reconstruction in this region are two large concentric drift chambers (central jet chambers), the inner CJC1 ($200mm < r < 453.5mm$), and the outer CJC2 ($527mm < r < 843mm$). Wires 2.2m long are strung parallel to the beam (z-direction). These consist of both sense wires and field wires inclined by about 30^o with respect to the radial direction (see figure 2.4). The CJC1 has 30 cells, each containing 24 sense wires, CJC2 has 60 cells with 32 sense wires each. The signals recorded from these chambers are used to determine the transverse track momentum and, in addition, to provide information on the specific energy loss dE/dx used for particle identification (essential for this analysis).

High momentum tracks will cross the sense wire plane at least once in CJC1 and CJC2. Particle passing times can be measured to an accuracy of $\sigma \sim 0.5ns$ allowing particles from different bunch crossings to be easily separated.

The space point resolution given in the $r - \phi$ plane is 170 μm. The z-coordinate is determined with a resolution of one percent of the wire length ($\sigma_z \approx 2-2.5cm$) by comparing signals read out at each end of the wire. This is sufficient to provide a link to the inner, CIZ ($173mm < r < 193mm$) and outer, COZ ($456mm < r < 480mm$) central z drift chambers to provide an accurate z coordinate for the charged tracks.

The CIZ and the COZ have polygon ring arrangements with 17 and 24 regions in ϕ respectively. Both contain 4 sense wires, arranged along lines inclined at 45^o to the chamber axis in the CIZ and strung around the COZ at constant z. This is because the COZ is at a greater radial distance with reduced polar angle coverage, meaning tracks will pass at larger angles. These two chambers achieve a typical resolution of $300\mu m$ in z and about five degrees in ϕ.

Finally, there are two Multi-Wire proportional chambers (MWPC). The Cen-

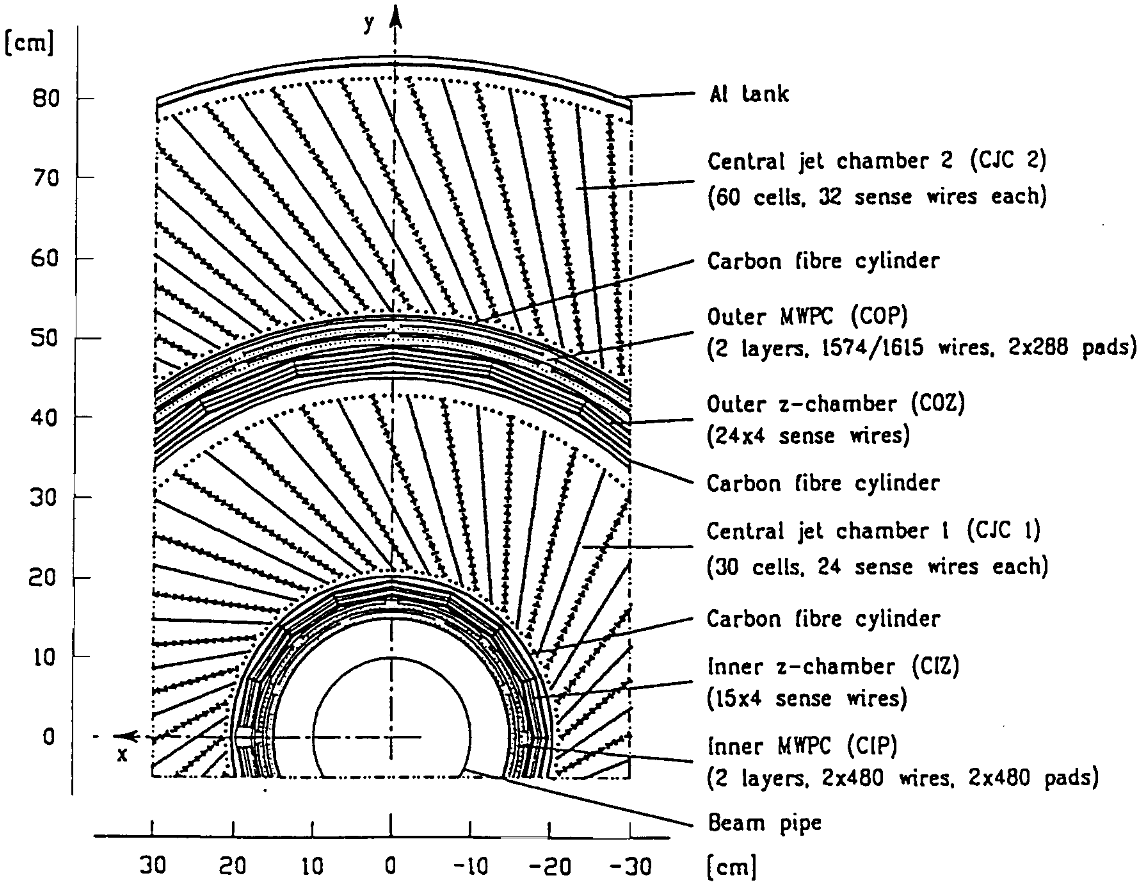

Figure 2.4: *Cross-section through the central track detector.*

tral Inner Proportional chamber (CIP) is located inside the CIZ, the Central Outer Proportional chamber (COP) fills the gap between the COZ and CJC2. These deliver a final timing signal (faster than two succeeding bunch crossings). Also, they are utilised by the first level trigger for fast charged track reconstruction using their ability to deliver moderately accurate space points. Both MWPCs have a double layer of cells with wires strung parallel to the beam axis. The available segmentation for the CIP is eightfold in ϕ with the two layers rotated by $\pi/16$ with respect to each other, and 60 pads in z in each ϕ sector. The segmentation of the COP is 18-fold in z and 16 fold in ϕ.

Using all chambers gives a resolution on the momentum of charged tracks of $\sigma_p/p^2 < 0.01\ GeV^{-1}$, with the polar angle measurable to $\sigma(\theta) \approx 1$ mrad.

2.3.2 The Forward Tracking Detector

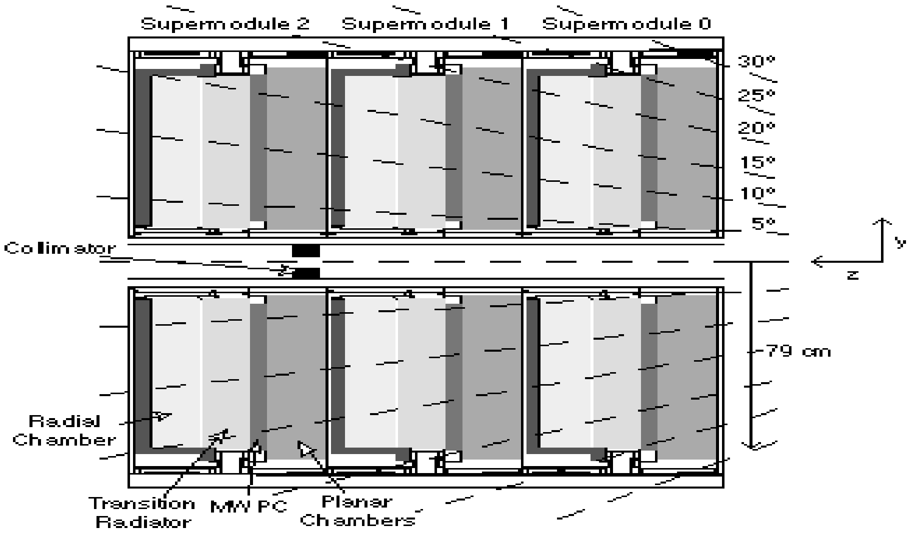

Figure 2.5: *The Forward Tracking Detector.*

The Forward Tracking Detector (FTD) at H1 covers the laboratory angles between 5^o and 30^o with respect to the forward proton beam direction. The detector exists in a very hostile region of H1, with a high primary track multiplicity ($\sim 10-15$). Also, material in the end wall of the CTD and around the beam pipe produce a large number of secondary tracks.

The FTD consists of three identical supermodules aligned along the z direction. Each supermodule has three layers of planar drift chambers (at 0^o, $+60^o and -60^o$ to the vertical), followed by a multi-wire proportional chamber (FMWPC), then a transition radiator and finally a radial drift chamber.

The drift chambers have wires of differing geometry, the planars, with 32 rectangular cells, have all their wires strung parallel with a readout at one end only which gives just the drift co-ordinate. The radial chambers have 48 wedge-shaped cells with the wires pointing radially outwards from the z-axis. Wires in pairs of wedges are connected together at the hub and read out at both ends, allowing measurement of the track co-ordinate along the wire by charge division. The planar chambers have a resolution $\sigma_{x,y} \sim 160 \mu m$, the radials have $\sigma_R \sim 2cm$.

To ensure that a track does not travel along a cathode wire plane in all 3 modules, the second and third radial modules are rotated by 3.75^o and 2.5^o (1/2 and 1/3 of a wedge).

The FMWPCs, mounted directly behind the planar chambers (in order to share the same gas mixture), are used to identify the correct bunch crossing and provide a fast trigger on tracks pointing to the primary interaction vertex (together with the CIP and COP). They contain two planes of pad readouts with wires orientated along the vertical (y) direction interleaved with three planes of ring shaped cathode readout pads.

The transition radiator consists of 400 polypropylene foils contained in its own gas volume. After passing through a mylar window, transition radiation photons are detected in the radial chamber. This is designed to produce up to 12 space track points from ionisation drift timing and charge division.

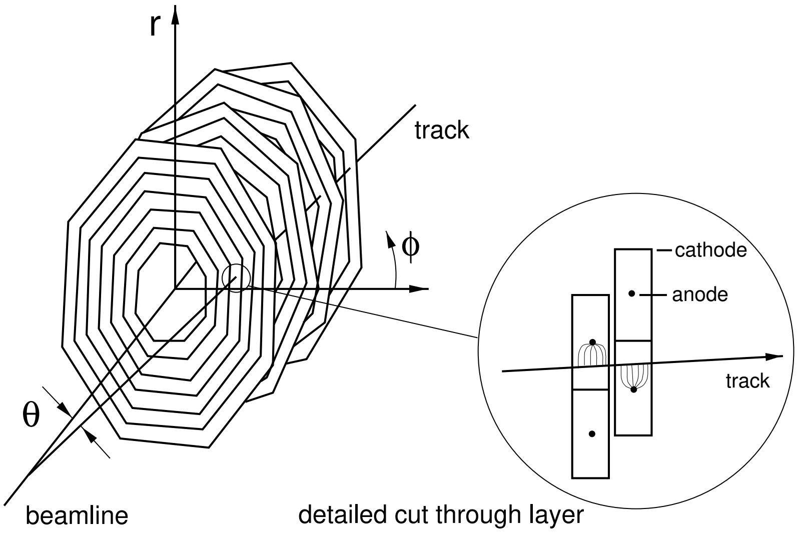

Figure 2.6: *The four BDC double layers.*

2.3.3 The Backward Drift Chamber

The Backward Drift Chamber (BDC) was constructed and installed as part of the last major upgrade of H1 in 1995. Its main purpose is to measure the direction of the scattered positron in the range $155^o < \theta < 178^o$ with full azimuthal coverage. This is then used for selection of deep inelastic scattering events and to determine the kinematics of these events.

The sense wires of the BDC are strung perpendicular to the beam axis, forming octagons of increasing size (figure 2.6). A positron scattering from the primary vertex travels through four double layers of drift cells, giving a maximum of eight space points for the track reconstruction. Because each layer contains parts insensitive to the positron path such as cell boundaries, each double layer is rotated by 11.25 degrees with respect to the previous one. To resolve left-right ambiguities in track reconstruction, every second layer is shifted by half a cell width in the radial direction.

Each octant has 16 small and 16 large drift cells, with a total of 2048 signal channels for all octants and layers. At small radii, the maximal drift distance is approximately 0.5cm which increases by a factor of three for cells more than

$\approx 25cm$ from the beam axis. This differing geometry is implemented to cope with the increased background rate at low radius from interactions between beam and beam pipe and with residual gas atoms.

2.4 The H1 Magnet

The magnetic field in H1 is provided by a superconducting solenoid situated outside the electromagnetic and hadronic calorimeters. Within this region, 3600 mm in length and 1600 mm in diameter, the average field is 1.15 T (this field varies by less than 3% over the sensitive tracking region).

The magnet mainly comprises of an aluminium clad superconductor wound on an aluminium former which supports the large electromagnetic forces generated. The superconducting material itself is a form of Niobium Titanium composite bound in copper. The octagonal iron barrel and its flat end-caps are the flux-return for the magnetic field. The field produces a force on the end-caps of the order of 1500 tonnes. The yoke is also laminated and interleaved with plastic streamer tubes which act as a 'tail catcher' for the hadronic calorimeter and also a muon detector system.

2.5 Calorimetry

The calorimetry in H1 is performed by four sub-detectors. The Liquid Argon calorimeter (LAr), covering polar angles $4^o < \theta < 154^o$, is the main calorimeter of H1. The SPACAL provides energy measurement in the backward direction ($150^o < \theta < 177^o$). Also there are the tail catcher (for leakage of energy from the LAr) and the plug calorimeters (measurement of energy flow close to the beam holes). These are not used in this analysis, therefore only LAr and SPACAL are discussed further below.

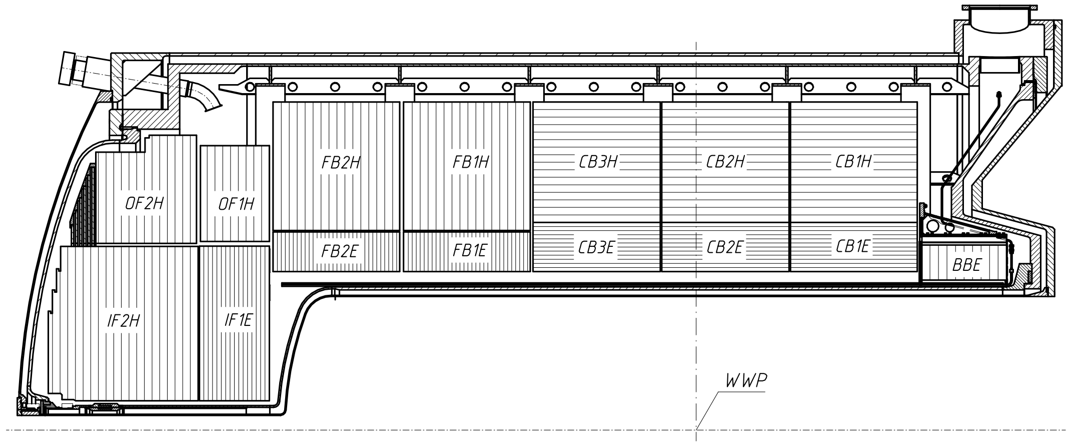

Figure 2.7: *Side view of the liquid argon calorimeter.*

2.5.1 The Liquid Argon Calorimeter

The LAr is a sampling calorimeter providing central and forward calorimetry for H1. It is housed in a cryostat inside the main solenoid. This minimises both the quantity of dead material in front of the calorimeter and its overall size and weight. The reasons for the use of the liquid argon technique are that of good stability, ease of calibration, homogeneous response and fine granularity.

The LAr calorimeter (figure 2.7) is subdivided into an inner electromagetic section and an outer hadronic section (with the exemption of the BBE which only has an electromagnetic part). These use lead and stainless steel plates respectively as absorbers. It is segmented into eight self-supporting wheels, with each of these further segmented in ϕ into eight identical stacks. To avoid dead regions arising from cracks, the two forward wheels (left side of figure 2.7) are assembled as two half-rings.

The thickness of the lead plates in the electromagnetic part are 2.4 mm with 2.35 mm of liquid argon as active material. The total thickness varies between 20 and 30 radiation lengths. Test beam measurements put the energy resolution at $\frac{0.12}{\sqrt{E}} \oplus 0.01(GeV)$.

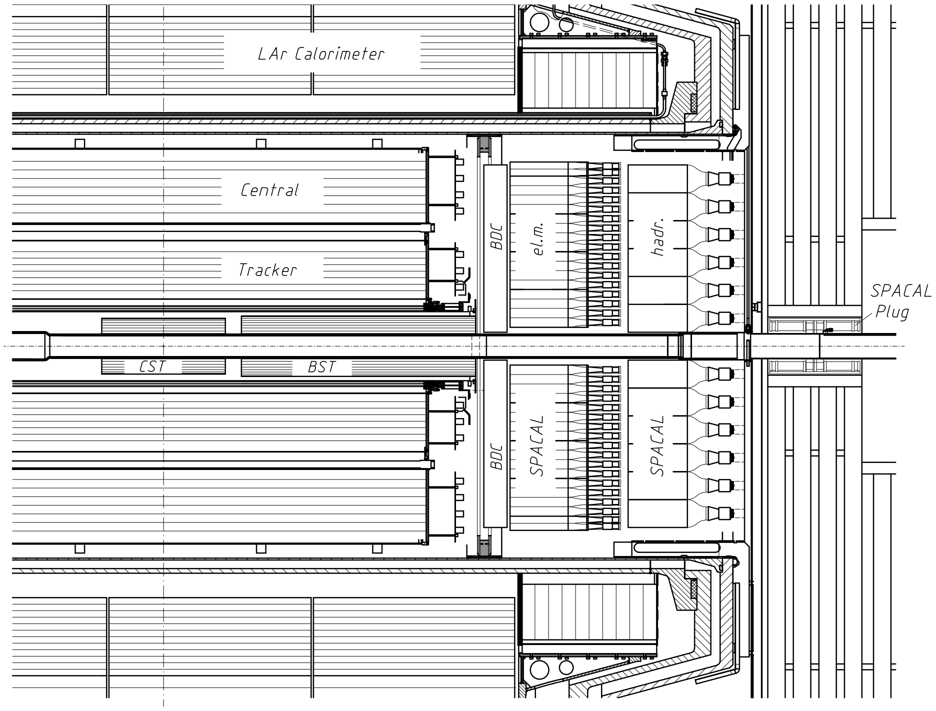

Figure 2.8: *Side view of H1 showing the positions of the SPACAL and BDC.*

The absorber plates of the hadronic cells have a thickness of 19 mm with a double gap of 2.4 mm liquid argon. This section represents between 5 and 8 interaction lengths in total. The energy resolution has been determined as $\frac{0.50}{\sqrt{E}} \oplus 0.02(GeV)$.

Since the response of the calorimeter to hadrons is about 30% smaller than that for positrons of the same energy, an off-line weighting procedure is applied to correct for this in hadronic energy measurements.

Using event properties such as transverse momentum balance, and using different event kinematic finding methods, the scale uncertainty is reduced to below 3% for the electromagnetic part. The hadronic scale is known to 4%.

2.5.2 Backward Calorimetry

Information of energy flow in the backward direction of H1 is mainly provided by a scintillating fibre Spaghetti Calorimeter (SPACAL) with lead absorbers.

The main purpose of this detector is for good detection and measurement of the scattered positron.

Particles incident on the SPACAL develop into a shower of secondary particles in the lead, causing the fibres to scintillate. Light from this process is collected by photo-multipliers. As with the LAr, the SPACAL comes in two parts- the electromagnetic part (nearest the interaction point) and the outer hadronic section (see figure 2.8).

This is complemented by the backward plug calorimeter, which is located in the iron yoke of the H1 magnet as can be seen in figure 2.8.

The active part of the electromagnetic part of the SPACAL is 28 radiation lengths deep, and for 30 GeV positrons, has negligible energy leakage. The SPACAL features good positron-pion separation as well as good positron resolution.

Mesh-type photo-multipliers read out a total of 1328 channels (1192 from the electromagnetic and 136 from the hadronic section), and achieve a time resolution of 1 ns while operating in the strong magnetic field of the H1 main solenoid. The signals are split into three branches: energy, timing and trigger. Time of flight information for both electromagnetic and hadronic sections is given by the excellent time resolution.

The uncertainty of the absolute energy scale has been demonstrated to be less than 1%. This was done originally with test beam measurements, and has been extensively checked by various methods such as; the study of QED compton processes and invariant mass reconstruction of π^0-mesons. Energies in the electromagnetic section can be measured with a resolution of $\frac{(7.1\pm0.2)\%}{\sqrt{E}} \oplus (1.0 \pm 0.1)\%(GeV)$.

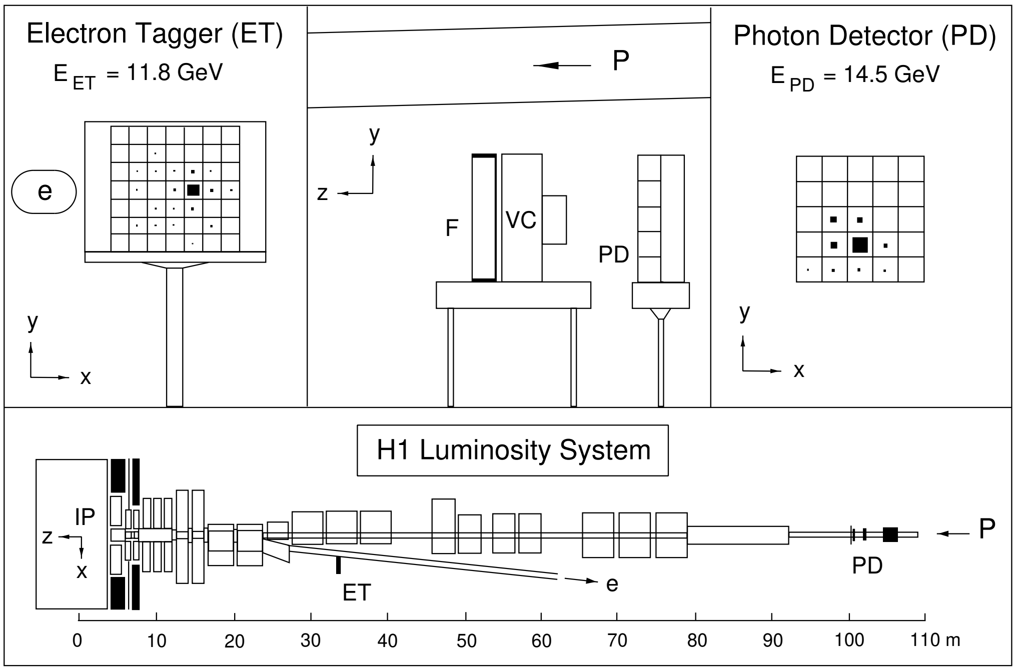

Figure 2.9: *The H1 luminosity system.*

2.6 Luminosity System

At H1, the Bethe-Heitler process $ep \to ep\gamma$, which has a large and precisely calculable cross-section, is used to determine the luminosity [40].

The layout of the luminosity system is shown in figure 2.9. The system contains two principle components: the Electron tagger (ET) lies close to the electron beampipe at $z = -33.4m$; the Photon Detector (PD) is next to the proton beam pipe at $z = -102.9m$. Both of these devices are hodoscopes of total absorption KRS-15 crystal Cerenkov counters. These were chosen on the grounds of their high radiation resistance, as well as their good energy, co-ordinate and time resolution.

Scattered electrons are deflected by low-beta quadrapoles and a bending magnet before passing an exit window at $z = -27.3m$ and hitting the ET. The photons leave the proton beam pipe where it bends upward at $z = -92.3m$ before reaching the PD. The PD is shielded from the high synchrotron radiation flux by a Pb filter ($2.2\chi_0$) followed by a water Cerenkov veto counter ($VC, 0.8\chi_0$). Both detectors are mounted on movable platforms which are retracted during beam injection to minimise radiation damage.

For luminosity determination, two different methods are used: the coincidence and single photon methods. The coincidence method requires the simultaneous detection of an electron and a photon. The information from the system in this mode is used during the beam steering phase to optimize luminosity. Later, the single photon method is used to measure the integrated luminosity $\mathcal{L}$ by counting Bethe-Heitler events with the photon energy above a certain threshold.

The main source of background is bremsstrahlung from residual gas in the beam pipe. The cross-section from this background process, $eA \rightarrow eA\gamma$, is larger than the Bethe-Heitler process with an almost identical signature. Thus, the background is measured experimentally using electron and proton pilot bunches.

The luminosity is then calculated as:

$$\mathcal{L} = \frac{R_{tot} - (I_{tot}/I_0).R_0}{\sigma_{vis}} \tag{2.1}$$

where R_{tot} is the total rate of the bremsstrahlung events, R_0 is the rate from the electron pilot bunches, I_{tot} and I_0 are the corresponding electron beam currents and σ_{vis} is the visible part of the $ep \rightarrow ep\gamma$ cross-section (with acceptance and trigger efficiencies taken into account).

In addition to the above, the ET is used to detect, and trigger on, scattered electrons at very low values of the four-momentum transfer $Q^2 < 0.01 GeV^2$.

2.7 Time-of-Flight Counters and the Veto Wall

Important parts of the H1 detector are the time of flight counters and the veto wall. These allow the influence of background emanating from interactions of the beam particles with, for example, residual gas particles to be minimised. These detectors are reliant upon precise timing information provided by the HERA machine (HERA clock). For each counter, a time window is set depending on its position. Particles arriving within this window originate from the nominal vertex. Particles are designated as background if they originate from elsewhere, as determined if they arrive at a counter outside its window.

The Time-of-Flight (ToF) counters are positioned in the backward (-z) direction between the return yoke and the beampipe (BToF), and in the forward direction around the beampipe at z=5.2 m (FToF). Also, gaps in the PLUG absorber have been instrumented in a similar way to the FToF and the BToF. These are the PLUG ToF (PToF).

The veto wall, positioned at z=-6.5 m and z= -8.1 m, is a double wall of scintillator counters (used for their good time resolution $\approx 2ns$).

Time-of-flight information is also provided by the SPACAL calorimeter close to the beampipe in the backward direction (see 2.5.2).

2.8 Triggering and Data Acquisition

The H1 detector is very complex, and with the short periods of time between the HERA bunch crossings, collecting the huge amounts of data supplied is a difficult task. The trigger system is used to select ep interactions of physics interest from this data flow and reject unwanted background. H1 has a multi level (L1-L5) trigger system for this task. At each level, the criteria used to select specific events increase in complexity.

The first level trigger (L1) is dead-time free and provides a trigger decision after $2.5\mu s$. Since the bunch crossings occur every 96 ns in HERA, the full event information is stored in pipelines until the L1 decision is reached. There are 128 L1 sub-triggers, each comprised of individual trigger elements from various detector components. Each element is essentially a logical statement; the sub-trigger is a logical combination of the elements that it contains. The event passes this trigger selection if one or more of the sub-triggers fire.

The second level trigger (L2) provides the opportunity to verify the L1 decision by using more sophisticated algorithms. The two L2 triggers used are the L2TT and L2NN: the topological and neural network based triggers. These provide a decision in $20\mu s$. No L2 condition is used in the analysis presented in this thesis.

Upon reaching a positive triggering decision at this stage, the entire event information is read out and transferred to the fourth level trigger (L3 is currently not used). L4 is a software trigger that runs on 32 RISC processor boards in parallel. The rate of accepted events entering L4 is typically $\mathcal{O}(10\text{Hz})$. At this stage, with full event information present, the background is further suppressed before being written to tape. Approximately 1% of the rejected events are written to a separate file for monitoring purposes.

At L5 (the last level) the events are fully reconstructed and categorised according to criteria put forward by the different H1 working groups. These events are then the starting point for physics analyses. Here also, about 1% of rejected events are kept for monitoring.

The data is arranged in separate 'runs' of events. The events in a specific run generally have been recorded with the same experimental set-up. Whenever conditions change, such as the trigger set-up, availability of sub-systems etc., a new run is started. An average run contains a few 10K events.

2.9 Detector Simulation

The H1 simulation program H1SIM [41], based on the GEANT [42] package, simulates all the physics processes associated with the passage of particles through the sub-detectors of H1. H1SIM outputs data banks of the same form as those produced by the detector itself. These are reconstructed using H1REC just as the real data banks are.

The full simulation process, then, can be summarised as follows: generated Monte Carlo (MC) → H1SIM → simulated MC → H1REC → reconstructed MC.

The detector has to be well understood, allowing for defects such as dead regions to be included in the reconstruction step.

The data can now be compared with the Monte Carlo and also unfolded for detector effects.

2.10 Quantities and Reference Frames Used

The laboratory and hadronic centre-of-mass (CMS) frames are used in this analysis. These are shown schematically in figure 2.10.

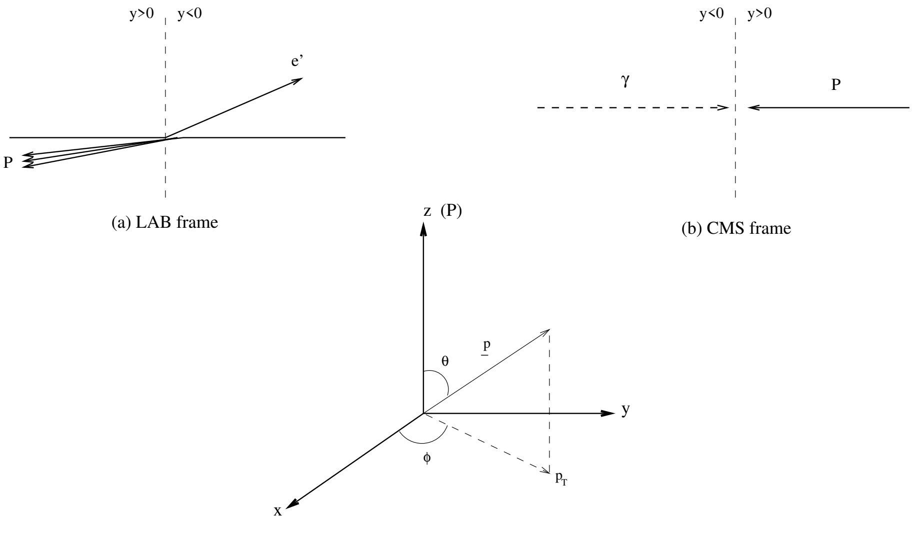

(a) LAB frame

(b) CMS frame

(c) H1 co-ordinate system

Figure 2.10: *The laboratory (a) and hadronic centre-of-mass (b) frames as used in this analysis and the co-ordinate system (c).*

The H1 laboratory frame is described by a right-handed co-ordinate system with the +z axis being the forward proton direction, and the origin as the nominal interaction point. The x-axis points inwards, towards the centre of the accelerator ring. The y-axis points upwards. A spherical co-ordinate system is also commonly used. The azimuthal angle (ϕ) is defined to be zero in the +z direction. The polar angle (θ) is measured from the z-axis.

Also, for relativistic particles, η (the pseudo-rapidity) is usually used instead of θ as the shape of the η distribution is Lorentz invariant:

$$\eta = -ln\left[tan\frac{\theta}{2}\right] \tag{2.2}$$

Which for massless particles is equivalent to rapidity:

$$y = \frac{1}{2}ln\left[\frac{E + P_z}{E - P_z}\right] \tag{2.3}$$

In the laboratory frame, y and η are defined to be positive in the forward proton direction.

Also used in this analysis is the quantity p_T the transverse momentum of tracks. This is (as can be seen from figure 2.10) the transverse component of a track's momentum with respect to the z-coordinate, which is the proton beam direction in the case of the LAB frame.

The CMS frame is defined to be the rest frame of the photon-proton interaction (figure 2.10(b)) with the z-axis pointing in the proton direction on the proton-photon axis. Rapidity and pseudo-rapidity is defined in this analysis to be positive in the forward PHOTON direction. And p_T in this frame is the transverse track momentum component with respect to the photon-proton axis.

Chapter 3

Particle Identification Technique (dE/dx)

The analysis for this thesis is principally concerned with the identification of charged kaons, pions and of protons.

In H1, this can be achieved by the simultaneous measurement of the momentum and rate of electromagnetic energy loss of the charged particle tracks passing through the central jet chambers[1].

The bulk of this chapter is a summary of work performed by Dr. J. Steinhart for his thesis [45] on which this thesis is largely reliant. It is shown here due to its integral part in this thesis and, as at the time of writing, no English write-up of his dE/dx analysis technique exists.

3.1 Track Momentum Measurement

The momentum information for the charged track is obtained from the curvature caused by the passage of the particle through the magnetic field present in the

---

[1] See 2.3.1 for more information on the CJC

central region of H1[2]. The trajectory of these particles with momentum p and charge Ze, passing through the magnetic field **B** is a helix with radius of curvature R and pitch angle λ. The radius of curvature and momentum component relative to **B** are related by:

$$pcos\lambda = 0.3z\mathbf{B}R \tag{3.1}$$

where p is measured in GeV, B in Tesla and R is in metres. The distribution of curvature measurements $k = \frac{1}{R}$ is roughly gaussian. The curvature error can be estimated by:

$$(\delta k)^2 = (\delta k_{res})^2 + (\delta k_{ms})^2 \tag{3.2}$$

where δk is the curvature error, δk_{res} is the error due to the finite measurement resolution and δk_{ms} is the curvature error due to multiple scattering.

For more detailed information on momentum measurement see the relevant chapter in [34] or see [43].

3.2 Ionisation Energy Loss dE/dx

The mean rate of energy loss of a charged particle traversing a specific medium (dE/dx) is given by the Bethe-Bloch equation [44]:

$$-\frac{dE}{dx} = 4\pi N_0 r_e^2 m_e c^2 z^2 \frac{Z}{A}\frac{1}{\beta^2}\left[ln\left(\frac{2m_e c^2\gamma^2\beta^2}{I}\right) - \frac{\delta}{2}\right] \tag{3.3}$$

Where, N_0 is Avogadro's number, Z and A are the atomic number and weight of the atoms in the medium, m_e is the mass of the atomic electrons, Z is the charge of the incident charged particle, r_e is the classical radius of the electron, and β and γ are $\frac{v}{c}$ and $(1-\beta^2)^{1/2}$. The product $4\pi N_0 r_e^2 m_e c^2$ is a constant equal to $0.307 MeV cm^2 g^{-1}$. I is an effective ionisation potential, given approximately by $I = 16Z^{0.9}(eV)$. The density effect correction δ gives rise to differences in energy loss behaviour at high energies.

---

[2] See Section 2.4

Figure 3.1 shows the form of the Bethe-Bloch equation plotted as a function of $\beta\gamma$. At low energies, the dE/dx formula is dominated by the $1/\beta^2$ term and decreases with increasing velocity. This decrease in dE/dx with respect to the increasing velocity is due to a decreasing interaction time (and thus less total energy transfer) between the traversing particle and the effective media.

As β approaches 1, the bracketed term in equation 3.3 increases, resulting in a broad minimum at a value of β of approximately 0.96 (or a kinetic energy of about 3.5 times the particle's rest mass). Particles with velocities corresponding to this region are termed 'minimum ionizing'. The value of dE/dx varies little from medium to medium for this minimum ionizing level ($1 - 1.5 MeV\ cm^2/gm$) since $Z/A \approx 0.5$ for most elements.

As β increases further, the $1/\beta^2$ term becomes essentially constant, dE/dx then steadily rises due to the bracketed term. The dE/dx rises as $2ln\gamma$ at first with the density term eventually limiting the slope to $ln\gamma$. Physically, these effects are attributable to the fact that the transverse electric field of the particle is proportional to γ, so that more and more distant atoms from the particle's path are ionized. Eventually, when distances are comparable to inter-atomic spacing, polarisation effects in the medium (associated with the dielectric constant) halt further increase. This Bethe-Bloch equation, as a function of $\beta\gamma = p/m$, is universal for all charged particles travelling through the same medium. As a function of momentum, it can be seen how separating out particle species with different masses becomes possible (see figure 3.12).

3.2.1 Measurement of the Energy Loss at H1

The calibration of the dE/dx values and general technique for their use in particle separation utilised in this analysis was developed by Dr.J.Steinhart, and although outlined in this section, more detail can be found in [45].

Energy loss measurements are taken using the sense wires in the CJC (Section

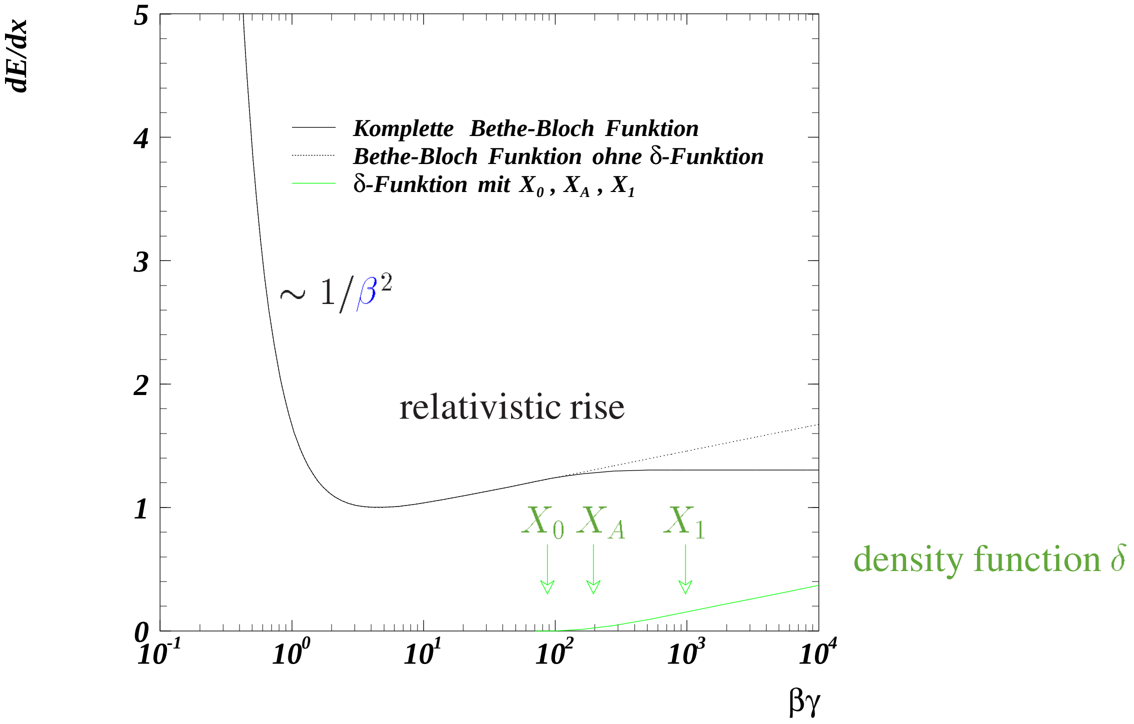

Figure 3.1: *The Bethe-Bloch Equation as a function of* $\beta\gamma$*.*

2.3.1). For a single sense wire, the energy loss is dE/dx_i. But, we want to measure the energy loss of a track left by a charged particle as it traverses the CJC. N_{dE/dx_i} is the number of sense wires used for the energy loss measurement for a given track.

The dE/dx_i of a track follow a Landau distribution [46]. If the dE/dx distribution followed a gaussian, the most probabilistic value could be easily taken as the arithmetic mean value of the constituent dE/dx measurements. The Landau distribution is more complex however, it has an asymmetric distribution with a high energy tail asymptotically extending to infinity as can be seen in fig.3.2. Different methods have been used to cope with this effect. One method often used is the truncation method, first proposed in [47], in which a new distribution is formed by cutting out the tail of the original dE/dx distribution. Another method is used by the H1 experiment [36]. In this method, the dE/dx value is given by the average of a transformed distribution in which the tail contribution

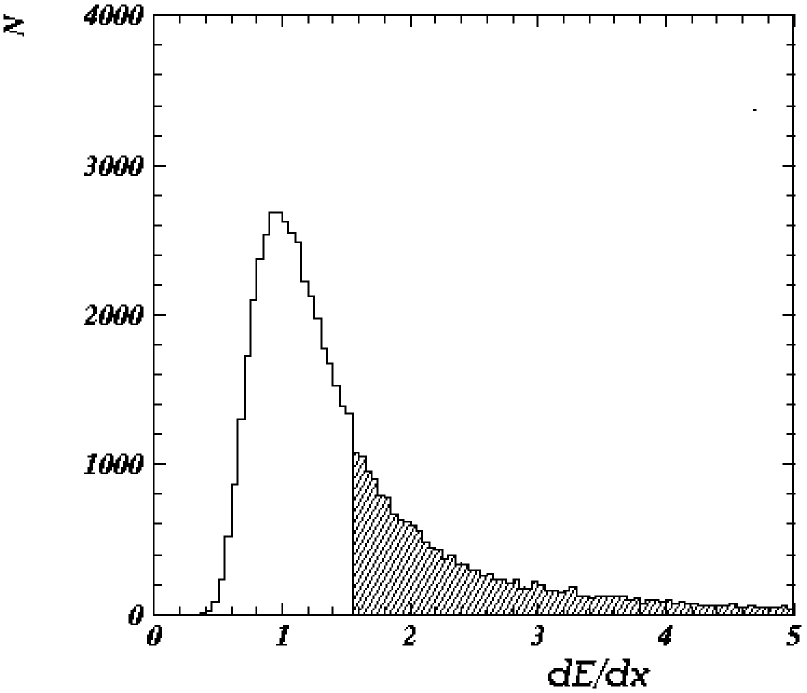

Figure 3.2: *The Landau distribution as observed for ionisation loss*

is suppressed.

$$dE/dx = \left(\frac{1}{N_{dE/dx_i}} \sum_{i=1}^{dE/dx_i} \frac{1}{\sqrt{dE/dx_i}} \right)^{-2} \tag{3.4}$$

The precision of the dE/dx measurement is governed by the width of the distribution and is largely dependent on N_{dE/dx_i}:

$$\sigma_{dE/dx} = p_1 . \frac{1}{\sqrt{N_{dE/dx_i}}} + p_2 + p_3 . N_{dE/dx_i} \tag{3.5}$$

taken from [45] where $p_{1,2,3}$ are parameters associated with gas densities and make-up of the CJC which are variable, and hence different values are used for these parameters for different time periods.

As special requirements ensuring good quality measurements of dE/dx values are required, only $\approx 80\%$ of hits used for track reconstruction (N_{track}) are also used for the dE/dx measurement. Always $N_{dE/dx} < N_{track}$, with a minimum of $N_{dE/dx} = 5$ required for the online reconstruction of the dE/dx. Although, a higher value is placed by this analysis for better quality dE/dx measurement (see discussion later in section 4.3.2).

3.2.2 Online Calibration of dE/dx Measurement

Calibration constants are calculated and stored during online reconstruction to account for the dependency of the dE/dx values with atmospheric pressure, lepton beam current and the high voltage settings of the CJC. This calibration is performed with minimum ionizing pions with: $0.3 \leqslant p \leqslant 0.7 GeV$; $N_{dE/dx,i} \geqslant 10$.

The calibrated measurement can then be normalised to unity:

$$dE/dx_{cal} = dE/dx_{meas} \cdot \frac{1}{ddx_{1,2}} \tag{3.6}$$

Where $ddx_{1,2}$ are the calibration constants for CJC1,2 respectively. The contributions to these constants can be seen in figs.3.3, 3.4, 3.5.

From fig.3.3 it can be seen that the dE/dx measurement changes with atmospheric pressure: higher atmospheric pressures give rise to higher dE/dx values.

Lepton beam current dependencies arise as the beam current gets smaller, for example, space charge effects are smaller causing a higher effective HV of the sense wires. The gas amplification is then higher, giving higher dE/dx values (fig.3.4).

All dE/dx corrections are also performed in run ranges with similar HV settings e.g. 4 ranges for 1996 (fig.3.5).

3.2.3 Off-line dE/dx Modifications

Due to several problems and software bugs, the online dE/dx calibration was found to be very slow and give inaccurate dE/dx values which were all too low when compared to theory.

Hence, a new off-line correction procedure is used [45] which calibrates the dE/dx measurement based on dependencies on different parameters:

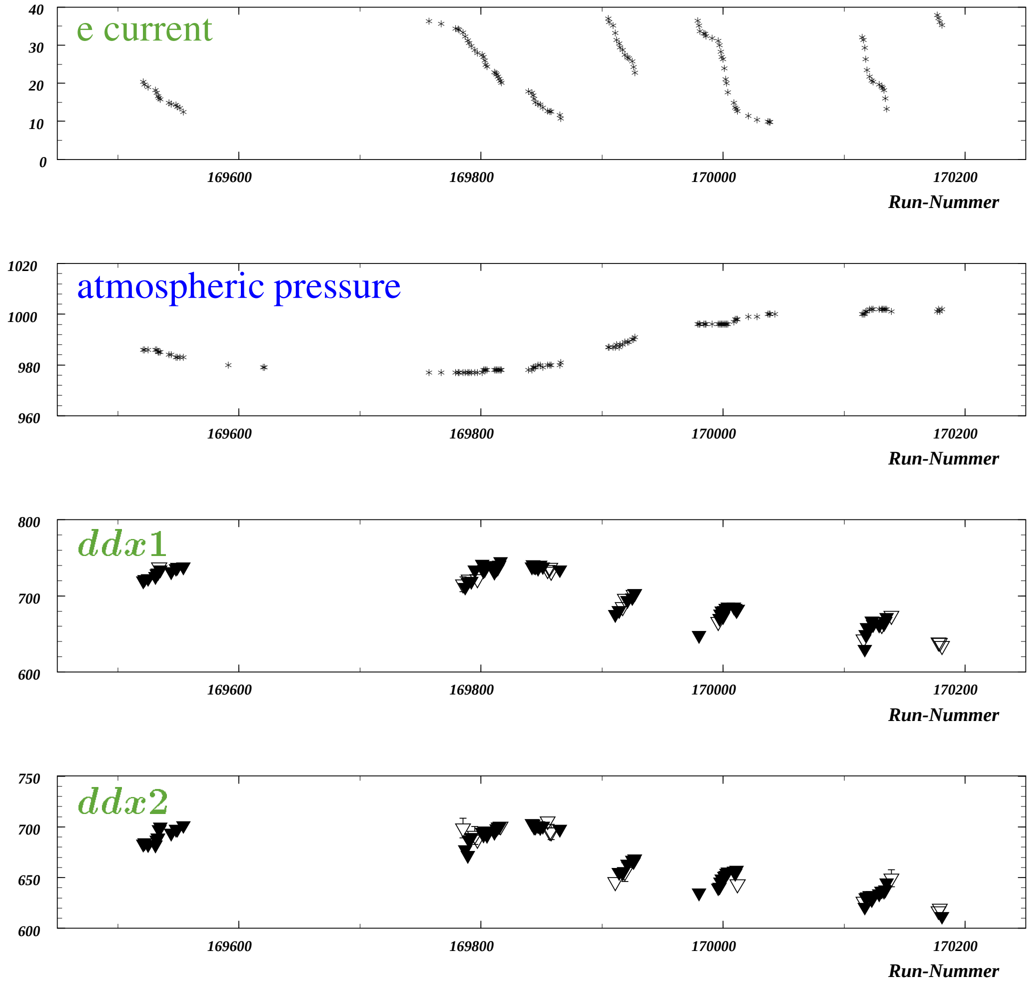

Figure 3.3: *dE/dx measurement dependence on atmospheric pressure from [45]*

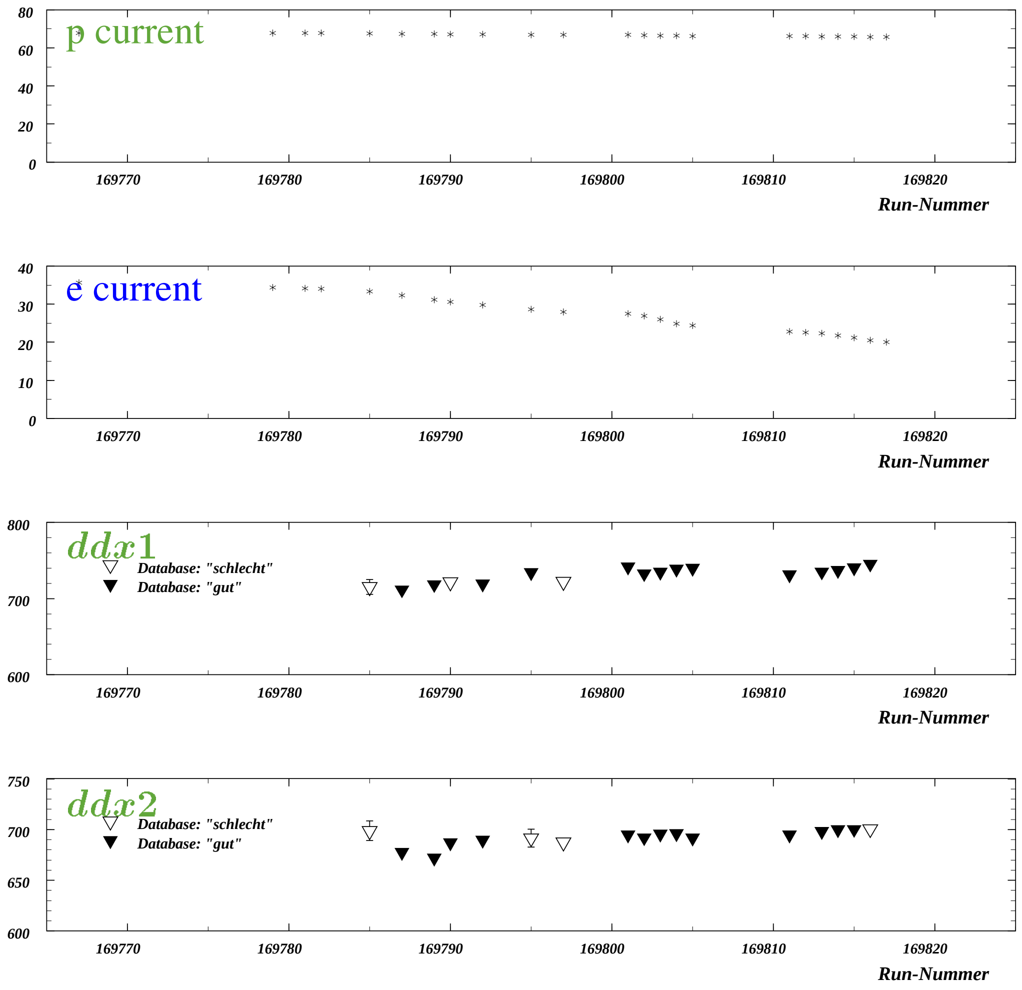

Figure 3.4: *dE/dx dependency on the lepton beam current from [45]*

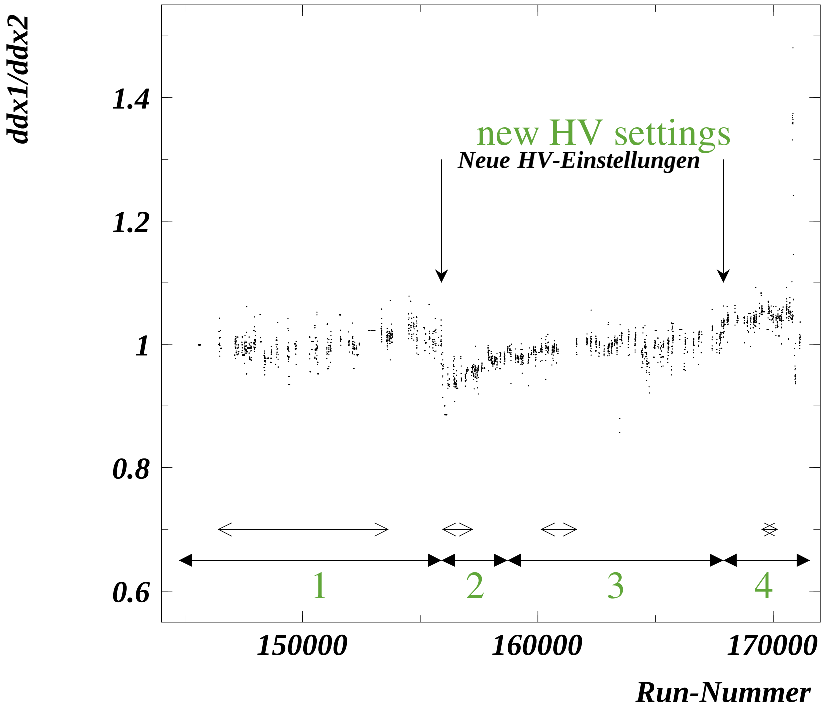

Figure 3.5: *Dependency of the dE/dx measurement on the HV settings, from [45]*

- Polar angle θ
- Ionisation $dE/dx_{uncorr.}$
- Charge q
- Azimuthal angle ϕ
- momentum p
- HV settings (run range)

Figure 3.6 shows the non-optimal description of the data by the quasi-empirical Bethe-Bloch formula shown below using the uncorrected dE/dx measurements.

$$-\frac{dE}{dx} = \xi z^2 \frac{1}{\beta^2}[K + ln(\beta^2\gamma^2) - \beta^2 - \delta(\beta, X_A, a)] \tag{3.7}$$

Where the Sternheimer and Peierls parameterisation of the density function is

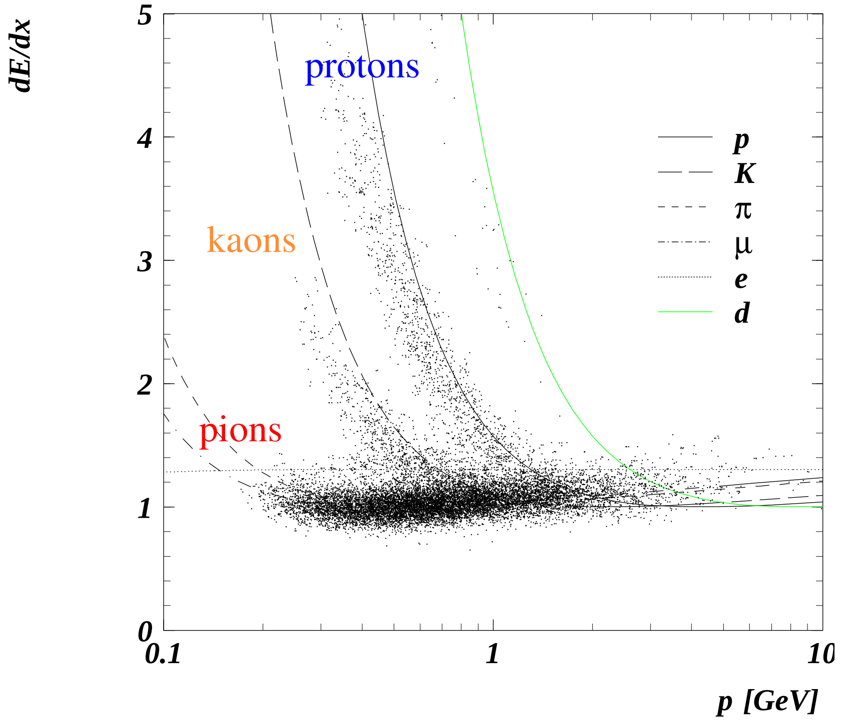

Figure 3.6: *Non-calibrated dE/dx data as a function of momentum p against theoretical values derived from equation 3.7, from [45]*

used [49]:

$$\delta = \begin{cases} 0 & : \; X < X_0 \\ b(X - X_A) + a(X_1 - X)^m & : \; X_0 \leq X \leq X_1 \\ b(X - X_A) & : \; X_1 \leq X \end{cases}$$

Where X, X_0, X_1 are the labelled points in fig 3.1. Kaons, pions and protons are used for the new corrections selected for $N_{dE/dx,i} \geqslant 15$ and sorted into 18 θ-bins and 40 p-bins for pions and 6 θ-bins and 40 p-bins for protons and kaons.

The measurement peak is found from $\frac{dE/dx}{dE/dx_{theo}}$ distributions for each particle candidate (r). Figure 3.7 shows r_{pion} in different θ bins. An example of the dependency of the dE/dx values on $cos\theta$ in the case of positively charged pions is shown in figure 3.8 for the first 20 p-bins. The error bars shown are taken from the widths of the distributions of r_{pion} shown in figure 3.7. The fit to these

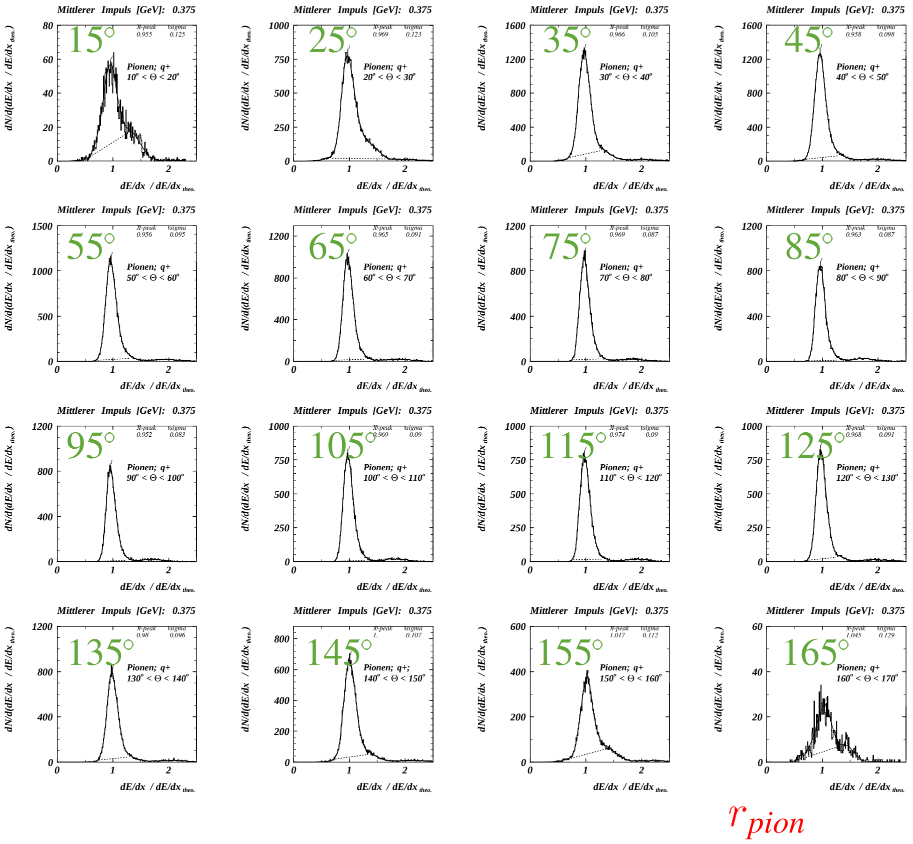

Figure 3.7: *dE/dx peak values taken from peak of shown distributions for calibration purposes- shown is for pions (r_{pion}) from [45]*

distributions shown is done with a quadratic function:

$$a + b.cos(\theta) + c.cos(\theta)^2 \tag{3.8}$$

A linear correlation of the fit parameters a and c was found (fig.3.9), which shows that at higher ionisations ($\sim a$) the θ dependency of the dE/dx measurement is stronger ($\sim c$). The dependence of the measured dE/dx value for pions on ϕ is seen in figure 3.10 where the ratio of measurements taken in different quadrants of the CJC is used. A new dE/dx parameterisation is introduced [45] which allows one 'norm function' to be used for all particles and charges (see fig. 3.11). This new parameterisation takes the form:

$$f_{dE/dx} = p_1.\frac{1}{\beta^{p_2}}\Big\{1.0 + [p_3.exp\{-p_4.log(0.25 + \beta\gamma)\}]\Big\} \tag{3.9}$$

The parameterisation is done using data points of protons, kaons, and muons

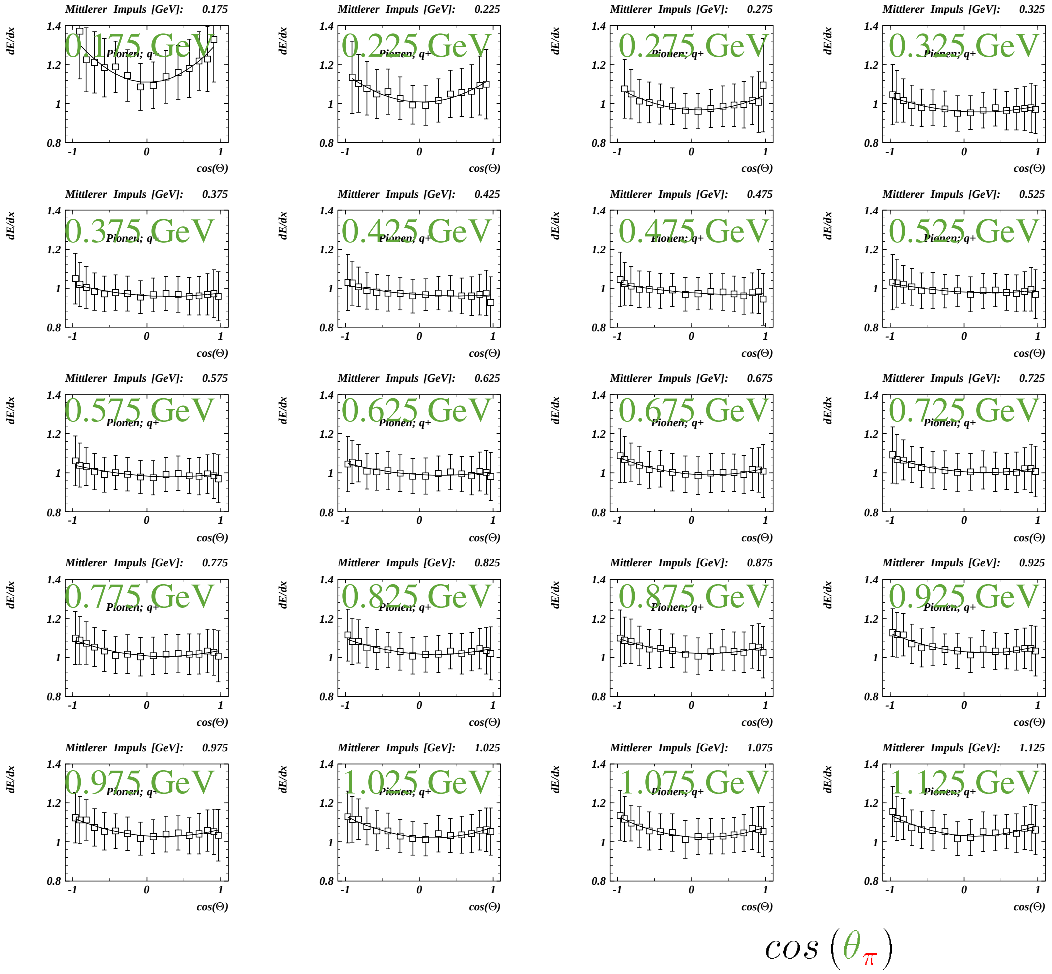

Figure 3.8: *Dependency of dE/dx values on $cos\theta$ from [45]*

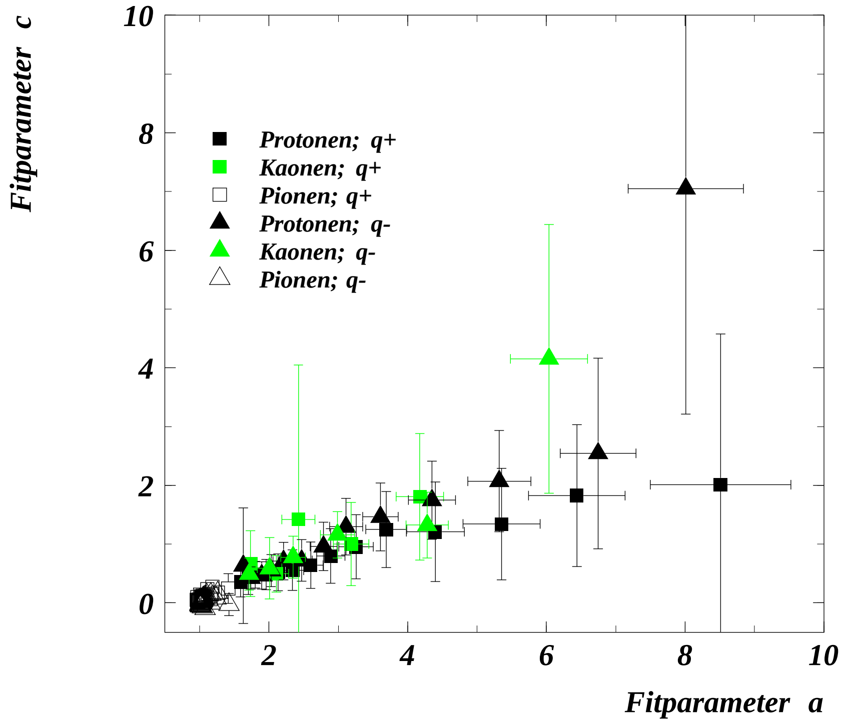

Figure 3.9: *Linear correlation of the fit parameters a and c from the function 3.8 from [45]*

with input values always taken at $\theta = 90^o$. The raw dE/dx values can now be corrected in a similar way to that in eq. 3.6 by the generation of a new correction function:

$$dE/dx_{cor} \equiv f_{cor}(\theta, dE/dx_{uncorr}, p, q, \phi, run) \tag{3.10}$$

Thus, the raw values are corrected to the 'norm function' (eq. 3.9); as well as the corrections in f_{cor} of the θ dependency by eq. 3.8 and the linear behaviour of the c parameter with dE/dx; a small correction to particles with very low momenta p; all done dependent on charge q, azimuthal angle ϕ and in several run ranges corresponding to different HV settings.

Using these corrections, the θ and ϕ dependencies are removed and a better agreement is seen between data and theory (the reference function 3.9) as shown in figure 3.12.

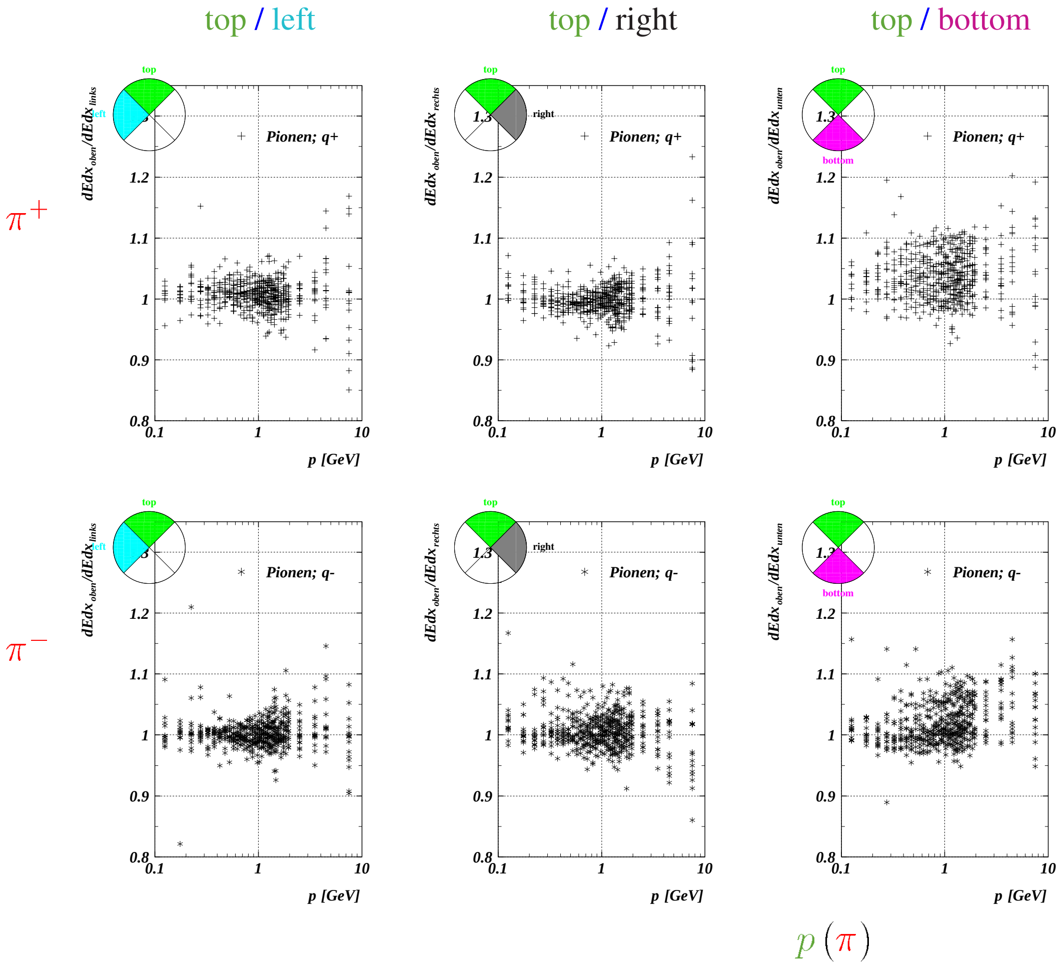

Figure 3.10: *dE/dx measurements of pions as a function of momentum p in different areas of ϕ in the CJC from [45]*

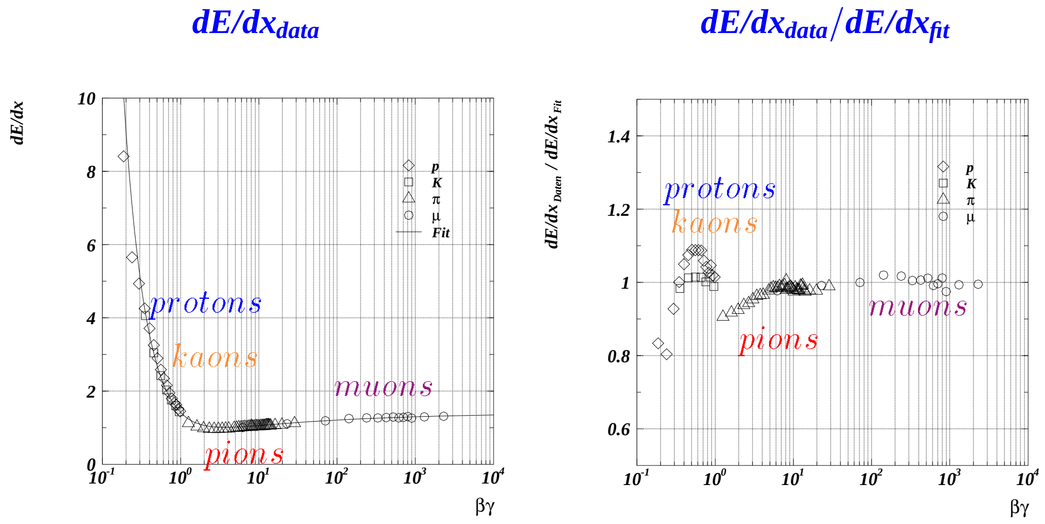

dE/dx_{data}

$dE/dx_{data}/dE/dx_{fit}$

Figure 3.11: *A single parameterization of all particle species, shown is the data points superimposed on the 'norm function' and the ratio of data to this function from [45]*

3.3 Particle Identification

After re-calibration and using the correction function 3.9, it is now possible to use the dE/dx for particle identification.

The resolution of the dE/dx measurement is good for well measured tracks, after re-calibration, as shown in figure 3.13. This, as can be seen in figure 3.12 enables particles to be readily separated at low momenta ($p \lesssim 1GeV$) for protons and charged kaons and pions. Such separations between particles is quantitatively handled by the following equation:

$$S = \frac{(dE/dx)_A - (dE/dx)_B}{\sigma_{dE/dx,B}} \tag{3.11}$$

This separation power for kaons, pions and protons is shown in figure 3.14. For the purposes of analysis, a selection cut criteria is required. For this, a selection cut for the separation of particles can be performed using visual cuts based on the graph in fig. 3.12. Or, more precisely, a log-likelihood method can be employed. Here, a χ^2 statistic based on the data points-theory curve graph is converted into a likelihood by integrating the χ^2 distribution for 1 degree of freedom. For

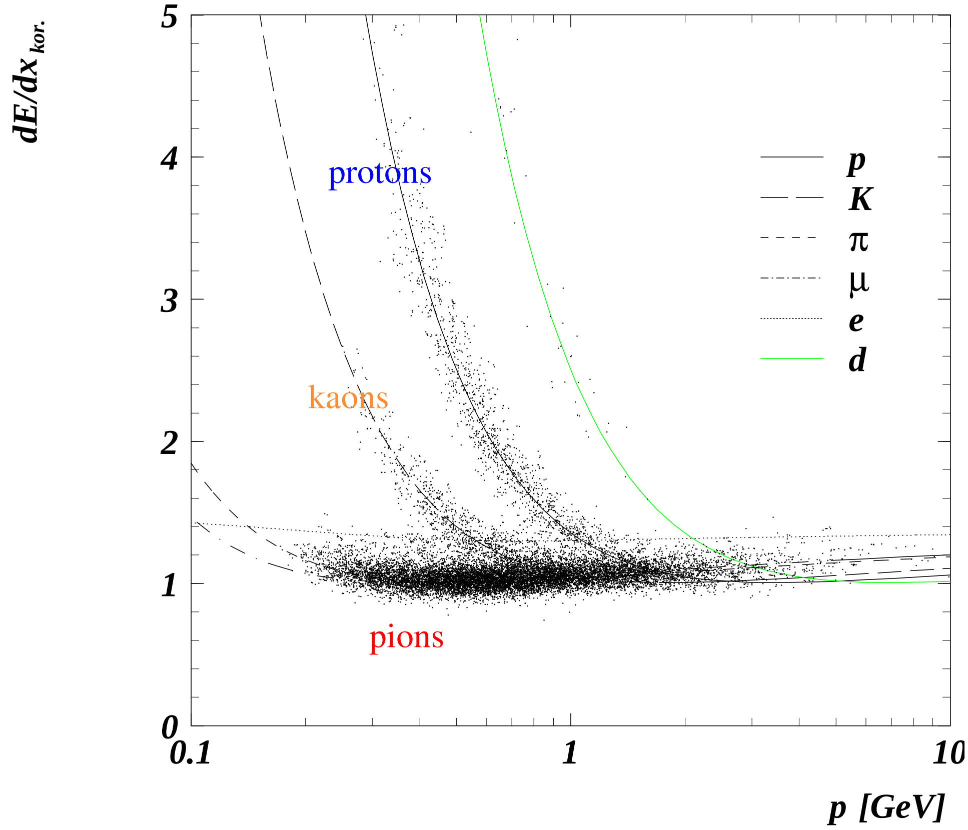

Figure 3.12: *Corrected dE/dx vs. momentum p with the theoretical curves from the standard reference function of eq. 3.9 superimposed for protons, kaons, pions, muons, electrons and deuterons (from [45])*

example see [48].

$$LH_i = \frac{1}{\sqrt{2}\Gamma(1/2)}.\int_{\chi_i^2}^{\infty} e^{-t/2}.\frac{1}{\sqrt{t}}.dt \tag{3.12}$$

$$\chi_i^2 = \frac{[dE/dx - f_{dE/dx,i}]^2}{\sigma^2} \tag{3.13}$$

Here, LH_i is the log-likelihood of the particle hypothesis i for the data point with its corresponding dE/dx value; $\Gamma(1/2)$ is the gamma function for 1 degree of freedom, t is the χ^2 being integrated; $f_{dE/dx,i}$ is the reference function (eq. 3.9) for particle hypothesis i; σ is the error on the dE/dx data measurement from eq. 3.5.

The log-likelihoods of different particle hypotheses for the data dE/dx points are then normalised to give a normalised log-likelihood value for the different

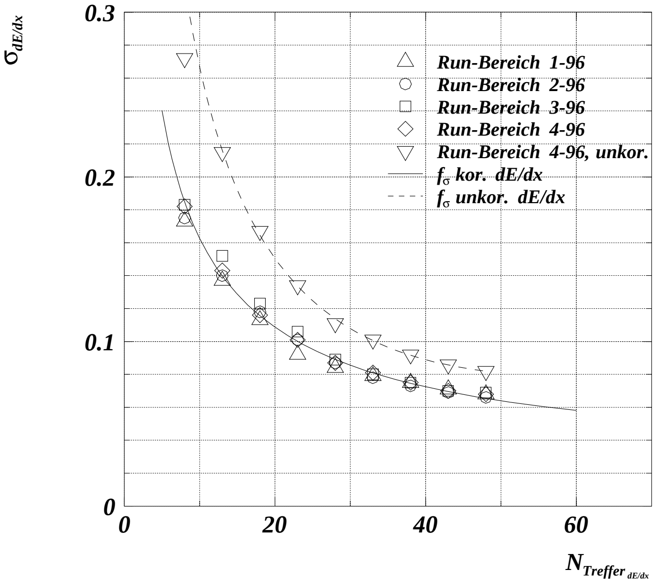

Figure 3.13: *Resolution of dE/dx measurement as a function of $N_{dE/dx}$ (from [45]).*

hypotheses based on kaons, pions, protons, deuterons, muons and electrons.

$$LN_i = \frac{LH_i}{\sum_{j=1}^{6} LH_j} \tag{3.14}$$

A selection criteria is now devised, based on a cut on the normalised log-likelihood value. A particle hypothesis is accepted if it passes that cut. For specific detail on the particle identification techniques used in this analysis based on the principles outlined in this chapter, see later in section 4.3.2.

3.3.1 Particle Identification in Monte Carlo

The dE/dx is simulated for each sense-wire in the CJC, the momentum, particle identity and track length in each drift-cell volume is inserted into the Bethe-Bloch function and smeared with the Landau distribution.

With no modification to the dE/dx simulation, the correction functions are produced in the same way as described for data with respect to the reference function $f_{dE/dx}$ (eq. 3.9). In this way, the handling of Monte Carlo and data with

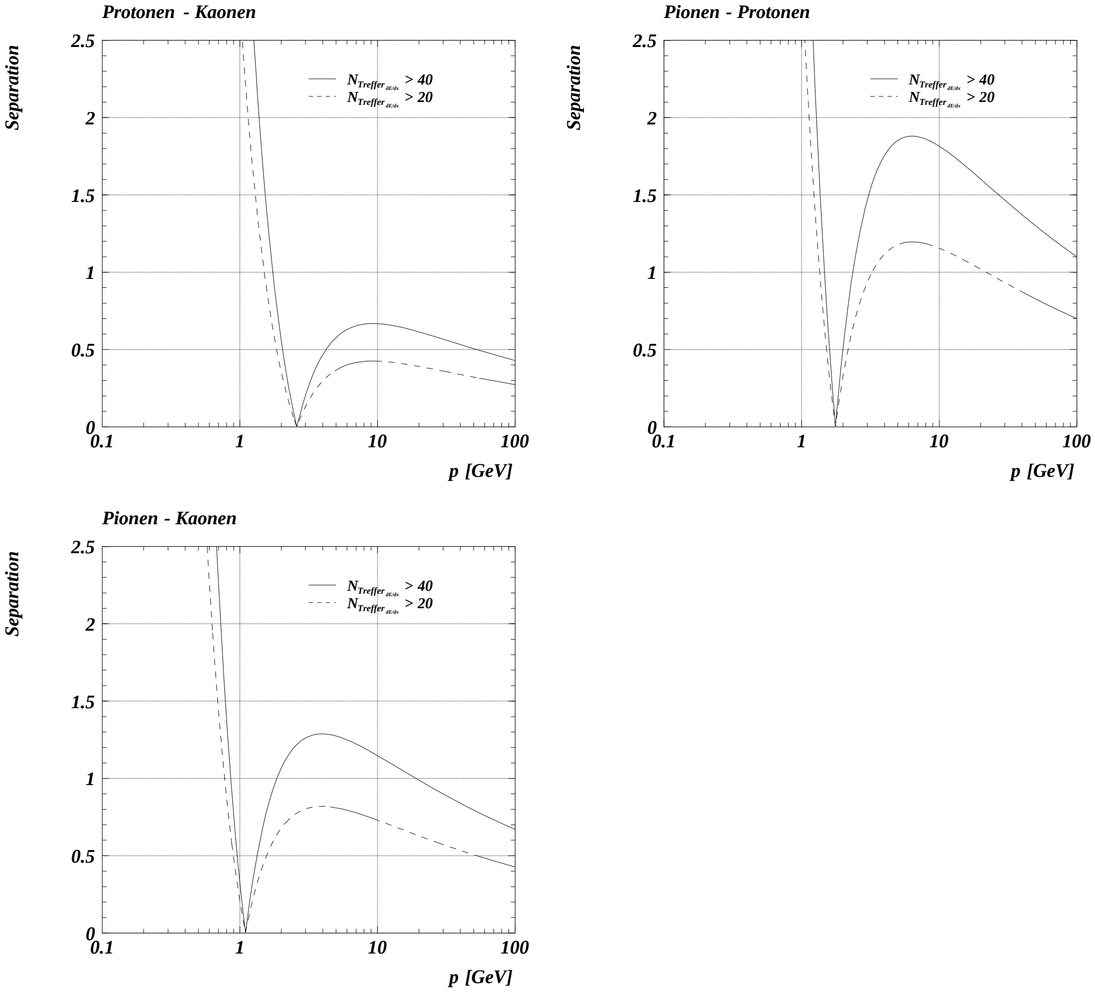

Figure 3.14: *Separation power as a function of momentum p based on eq. 3.11 for protons-kaons; pions-protons and pions-kaons (from [45]).*

respect to the dE/dx analysis can be done in the same way.

Although general agreement is good between Monte Carlo and data for various control plots associated with dE/dx analysis- there are differences where the modelling has not been perfect. The comparison of Monte Carlo and data in this respect has been studied within this analysis and some further refinements made where necessary. Details of which can be read in the discussion of event and track selections in section 4.3.

Chapter 4

Deep-Inelastic Scattering Event and Identified Particle Species Selections

This chapter describes the selection of DIS events from the available data sample used in this analysis. It also examines the use of various cuts to ensure the quality of this sample. It is then discussed how tracks are selected from this sample and how the dE/dx method described in Chapter 3 is employed to select charged kaons, pions and protons.

Unless otherwise stated, from here on a reference to a particle is also taken to refer to the anti-particle.

4.1 Selection of the *ep* Data Sample

The data for which this analysis is concerned was taken during the 1996 and 1997 running periods at H1. 1996 data is used for the bulk of the analysis, having a more reliable detector set-up which is well understood. The 1997 data sample is used for the Instanton analysis described in Chapter 6 due to the greater level of statistics available which is required due to the stringent cuts.

The first major effect to be taken into consideration during these running periods is a spot of beam related activity in the SPACAL (section 2.5.2) close to the beam pipe referred to as the 'hot spot'. This hot spot does not relate to interactions at the primary vertex and fires triggers related to the SPACAL with a high frequency. Thus, the SPACAL triggers were modified early in the 1996 running period to compensate for this. The range of *ep* data used in this analysis reflects this by only using data corresponding to the stable trigger settings after this change.

The data sample used is that starting from run 157877 (Aug. 31st 1996) to run 171155 (Nov. 29th 1996) and from run 177920 (Feb. 22nd 1997) to run 201519 (Oct. 13th 1997). The range 166000 to 168820 is omitted due to a drop in triggering efficiency which is not understood. Note that the first few weeks of the running years are used to optimise the detector performance.

Using this data sample, it is first filtered to obtain a sub-set of events that correspond to runs where the high voltage (HV) of the sub-systems important to this analysis were switched on. Namely, the central tracking system, the SPACAL and BDC, the liquid Argon calorimeters and the luminosity and time-of-flight/veto counters.

Events must also satisfy the conditions of the s001 L1 sub-trigger (see section 4.2.2) to enter the analysis. This requires an energy deposition of several GeV in the SPACAL as well as a well defined primary event vertex.

4.2 Low Q^2 DIS Event Selections

DIS events are defined by requiring the detection of a scattered positron in the SPACAL and BDC with considerable energy deposition. The kinematics of the event in terms of the Bjorken variables Q^2, x, y (see section 1.1.1) are calculated using the polar angle and energy of the scattered positron (equation 1.7).

Figure 4.1 shows the DIS phase space in terms of Q^2 and x. Requiring the use of the SPACAL to detect the scattered positron limits the data sample to the low Q^2 region ($\lesssim 100 GeV$), as can be seen in figure 4.1 by the curves corresponding to the acceptance limits of the SPACAL ($156^o < \theta_e < 177^o$).

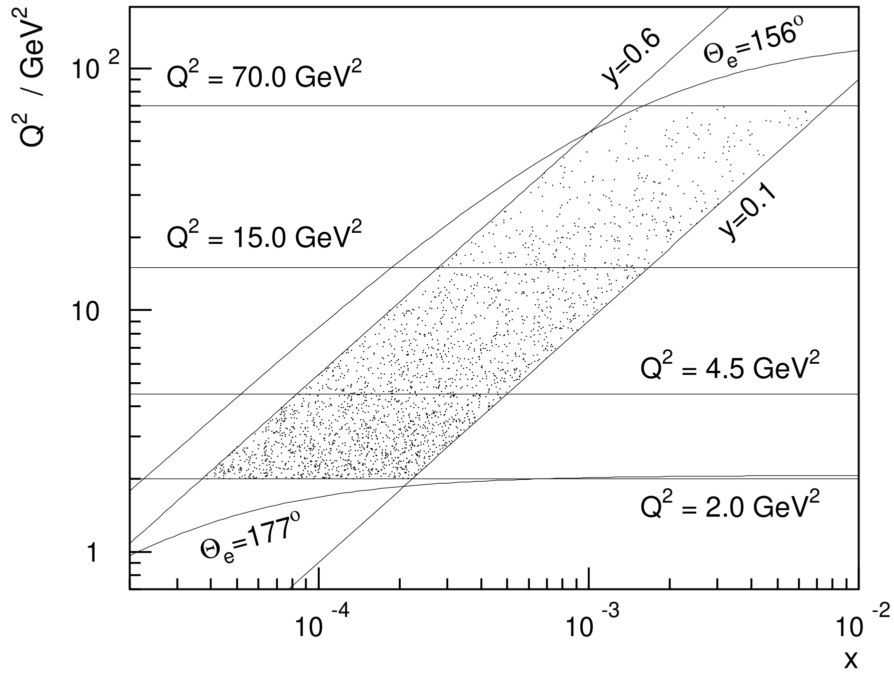

Figure 4.1: *The kinematic plane in terms of the Bjorken variables* Q^2 *and* x.

The kinematic region used for this analysis is the following:

$$5 < Q^2 < 70 \quad GeV$$

$$10^{-5} < x < 10^{-2}$$

$$0.1 < y < 0.6$$

which then defines the data selection in terms of these Lorentz invariant variables. The low Q^2 cut-off is chosen in order to minimise triggering correction effects (see section 4.2.2). The low y cut-off ensures a high-resolution measurement of the scattered positron that is also well modelled by Monte Carlo simulations.

4.2.1 Identification of the Scattered Positron

The most energetic reconstructed cluster of energy in the SPACAL, with a minimum energy requirement of 10 GeV, is taken to be the scattered positron.

The main source of background to DIS are hadrons which are mis-identified as the scattered positron. This leads to the wrong event kinematics being derived, or can cause events from photo-production processes to enter the event sample. To reduce this background contribution, the positron candidates are subject to a number of quality enhancing cuts:

- $R_{cl,e}$ has to be smaller than 3.5 cm (see figure 4.4). This is the transverse radius of the positron candidate cluster in the SPACAL. The cut rejects hadronic clusters, which are broader on average.
- $D_{tr,cl}$ is required to be smaller than 3.5 cm (see figure 4.4). This is the distance between the closest track in the BDC (used together with the event vertex for precise determination of the scattering angle- see 2.3.3) and the calorimeter cluster centre of gravity.
- $\sum_j(E_j - p_{z,j})$ is restricted to the range 35-70 GeV. This sum over all detected particles in an event will yield twice the incident positron beam energy if all the particles were correctly measured. In the case where the scattered positron escapes down the beampipe and a hadron is mis-identified as the scattered positron, the sum will in general yield smaller values. Photons radiated off the incoming positron and leaving the detector through the beam-hole also distort this quantity. (see figure 4.4).

In addition to these, a further important cut to place is that the reconstruction of the primary event vertex must yield a z-coordinate z_{vtx} closer than 35 cm to the nominal interaction point (see figure 4.4). This is important as z_{vtx} enters into the analysis in order to determine the polar angle of both the scattered positron and the final state particles.

Plots of the kinematic variables Q^2, x and y and of the detected polar angle, energy and transverse momentum of the scattered positron are shown in figure 4.3. Shown are the data points for 1996 data after corrections for triggering inefficiencies (see section 4.2.2). Also shown is the reconstructed Monte Carlo modelling of these quantities by the two models used to correct for detector effects in this analysis (see section 5.2). These plots show that the kinematics and simulation of the positron scattering are well modelled and understood. The biggest disagreement in these plots is from the peak region of the x distribution. Here, a re-weighting is applied to the Monte Carlo to study the systematic effects of this on the final corrected results in the analysis, which turn out to be small (see section 5.3).

In figure 4.4, plots of the other 4 event based cuts are shown (again with the Monte Carlo reconstruction shown). Here, two of the Monte Carlo distributions have had to be modified: the $R_{cl,e}$ distributions have been shifted right by $\approx 5\%$ by fitting gaussians to the data and Monte Carlo distributions; the z_{vtx} was also shifted by $\approx 5 - 10\%$, in this case by applying a weight to all Monte Carlo events (each Monte Carlo independently). The plot of the z_{vtx} before the application of the event re-weighting for data and Monte Carlo can be seen in figure 4.2, which also does not have the cut of $z_{vtx} < 35$ cm applied. In both of these cases, the effect of these changes is studied by examining the effects on the final corrected results and added to the systematic errors (see section 5.3). With the other two plots in figure 4.4, it can be seen that the Monte Carlo broadly models these distributions well, deviations of the Monte Carlo from the data are again studied in terms of final corrected results and included in the systematic errors.

4.2.2 Corrections Due to Triggering Inefficiencies

For the correct measurements of event rates, corrections must be made to the data sample for events rejected by the trigger which would have otherwise entered into

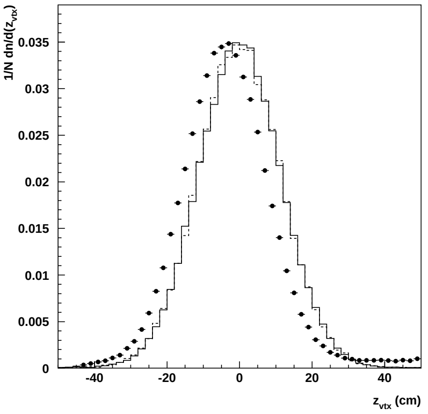

Figure 4.2: *Position on the z-axis of the reconstructed event vertex with no cut placed. The flat distribution on the right side of this plot is due to lepton beam-gas interactions.*

the final physics plots.

The Level 1 trigger (see section 2.8) used in this analysis is s001. This subtrigger is made up of a number of trigger elements which fire depending on different criteria, all of which must fire to fire the s001 trigger. This trigger has elements corresponding to:

- The need for energy deposits above 5 GeV in the SPACAL.
- The existence of a well defined primary event vertex determined by combining hits in the central and forward proportional chambers (see sections 2.3.1 and 2.3.2)
- Positive signals from the forward, backward and plug time-of-flight counters and time-of-flight information from the SPACAL. And also from the veto wall (see section 2.7).

It is important that the trigger remains stable over the running periods used in the analysis. This is checked by looking at the number of kaons, pions and protons measured in the analysis as a function of run number. As can be seen in

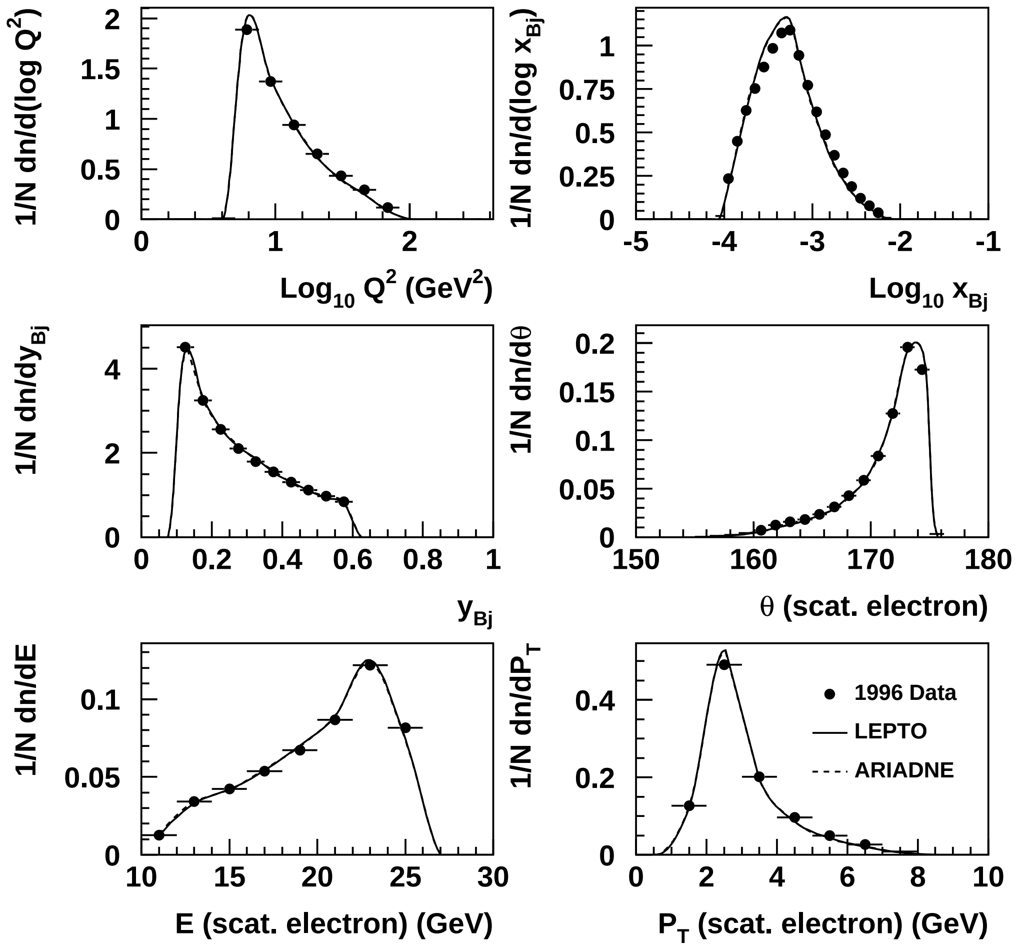

Figure 4.3: *Kinematic control plots: calculated from the scattered positron for 1996 data with triggering corrections and Django reconstructed Monte Carlo comparisons. Shown are the Bjorken variables* Q^2*,* x *and* y *as well as the energy, transverse momentum and scattering angle* θ *spectra for the scattered positron.*

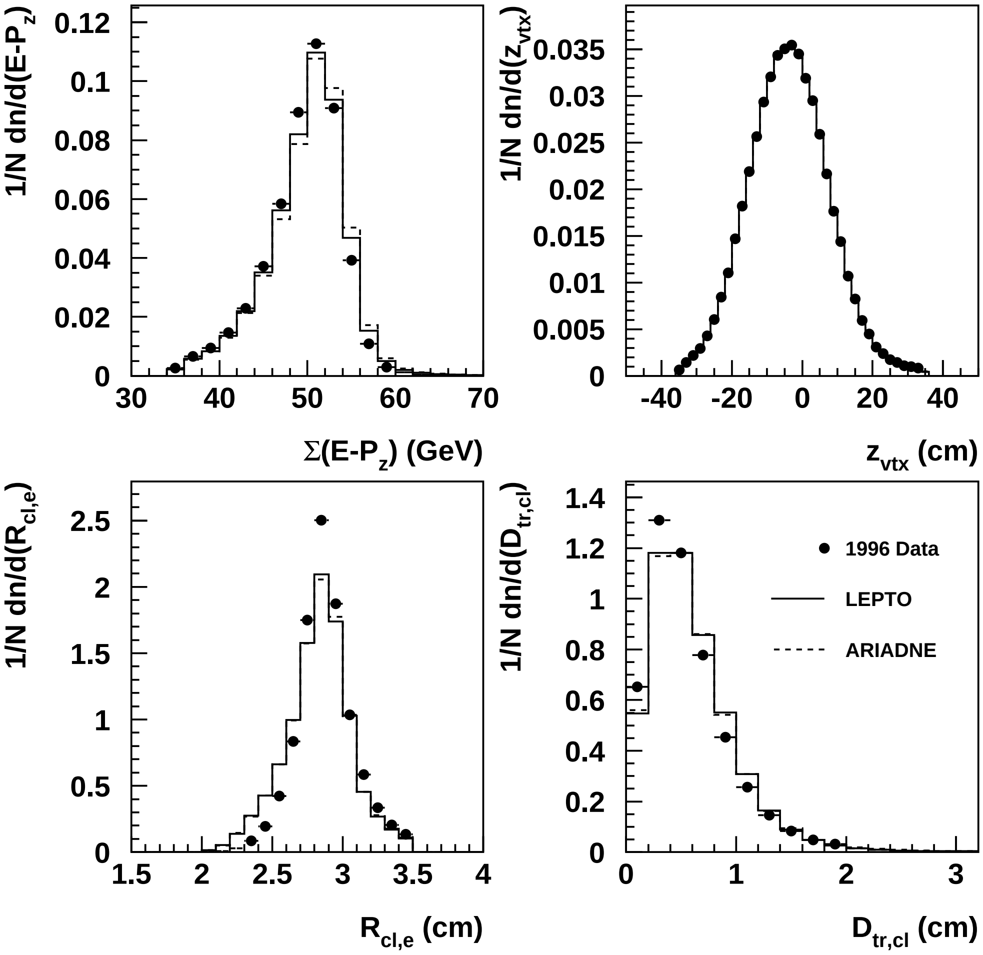

Figure 4.4: *Event selection control plots for 1996 data with triggering corrections and Django reconstructed Monte Carlo comparisons. See 4.2.1 for details of variables.*

these plots shown in figure 4.5, the average number of particle species produced over the running ranges stays approximately constant indicating the stability of this sub-trigger. Inefficiencies in the s001 sub-trigger are present in the vertex defining elements and the elements requiring backward energy deposition in the SPACAL. The s001 efficiency is thus measured in two parts.

To measure inefficiencies arising from the SPACAL trigger element, a monitor trigger *lar* is used which requires one of s060, s067, s075 or s077 firing. These sub-triggers are mainly based on energy depositions in the LAr calorimeter. The efficiency of this part of s001 is then determined by:

$$\epsilon_{s1,SPACAL} = \frac{lar \ \& \ s001}{lar} \tag{4.1}$$

i.e. the ratio of the number of events which were fired with the *lar* monitor trigger and the s001 sub-trigger, to the number triggered by just the *lar* monitor trigger.

To measure the inefficiencies of elements of s001 requiring a vertex, s000 is used as a monitor trigger which mainly uses the same backward energy deposition requirements as the s001 SPACAL elements, but has no vertex or central track energy requirements. The *vtx* efficiency is thus determined by:

$$\epsilon_{s1,vtx} = \frac{s000 \ \& \ s001}{s000} \tag{4.2}$$

Plotting $\epsilon_{s1,SPACAL}$ in terms of Q^2 (top plot in figure 4.6), it can be seen that at larger Q^2 values ($\gtrsim$ 10 GeV) the efficiencies are high ($> 90\%$), whereas, at lower Q^2 values the efficiency drops off towards the cut-off value for the analysis. This is due to the problem of the hot spot (mentioned in 4.1) which effects positron detection close to the beam pipe which equates to lower Q^2 values.

In the bottom plot of figure 4.6- looking at $\epsilon_{s1,vtx}$ as a function of visible charged track multiplicity, the efficiency is high over the majority of the sample. Inefficiencies here occur at low and, to a lesser extent at high multiplicities. This is where the track reconstruction performed by the proportional chambers become more difficult.

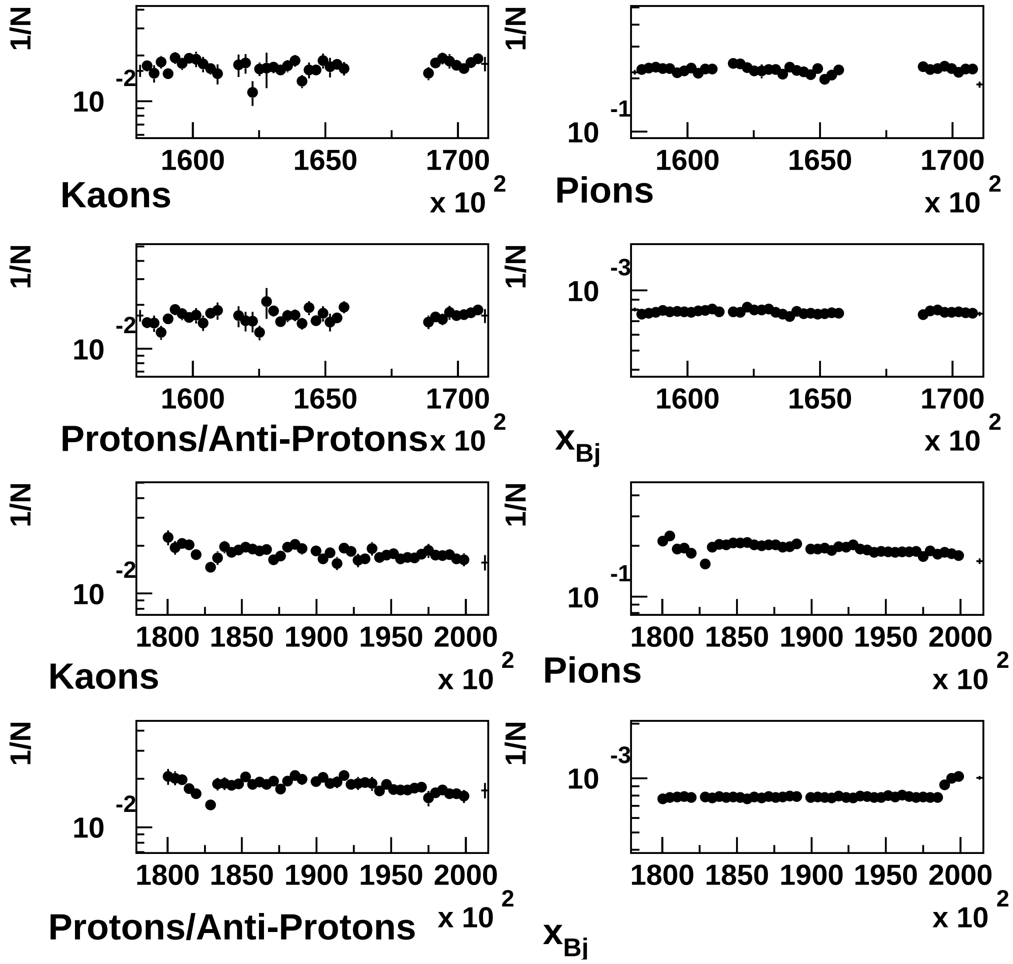

Figure 4.5: *Ave. Number of measured particle species and kinematic values of x plotted as a fn. of run number over the 1996 (top 4 plots) and 1997 (bottom 4 plots) running periods.*

These inefficiencies are corrected for in the data sample by using polynomial fits to the Q^2 and event multiplicity distributions shown in figure 4.6. An event weight is then calculated using the inverse of these fits read off for the values of Q^2 and multiplicity corresponding to the particular event. The event weight is then simply the product of these two values.

To perform a systematic check of this procedure, the above is performed using the s002 sub-trigger in place of s001. This has a similar format with respect to ToF triggering as s001, but has a slightly different SPACAL and vertex triggering arrangement. It has the additional requirement of needing at least 800 MeV in transverse track momentum in the event.

Systematic errors are calculated by looking at the difference this makes to the final corrected results (see section 5.3), and the effect is found to be small.

4.3 Track Selections and Identification of Charged Kaons, Pions and Protons

From the event sample defined by the selections described thus far, tracks measured in the central tracking system of H1 (see section 2.3.1) are used to identify the required particle species.

4.3.1 Track Quality Cuts

In order to use only good quality, well measured tracks, the following acceptance criteria are placed on track candidates entering the central tracker:

- The track must be reconstructed with information taken from at least 5 hits in the CJC (later made redundant by more stringent criteria imposed by dE/dx requirements)

- The measured p_T of the track must be at least 150 MeV.

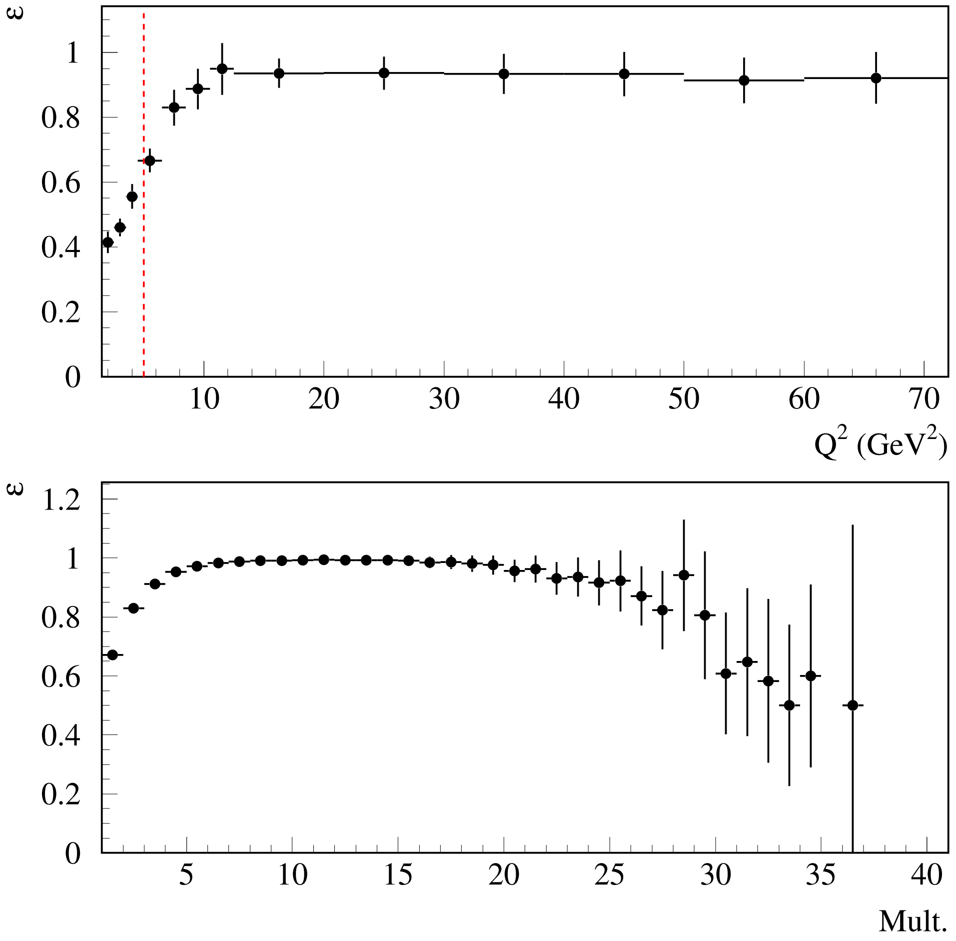

Figure 4.6: *Triggering efficiency for SPACAL and vertex elements of the s001 sub-trigger. The top plot is in terms of Q^2 with the cut-off at 5 GeV^2 as placed in this analysis shown. The bottom plot is in terms of event charged particle multiplicity.*

- The distance of closest approach (DCA) of the track to the measured vertex must be less than 2 cm. This reduces the number of tracks possibly originating from background processes such as beam-gas interactions.
- The radius in the CJC of the start point of the reconstructed track r_{start} must be under 50 cm, suppressing tracks originating from possible secondary processes.
- The length of the reconstructed track l_{tr} must be at least 10 cm. This ensures a good quality momentum and position reconstruction of the track.

Comparisons of the quantities DCA, r_{start} and track length with the Monte Carlo models used for detector corrections are shown in figure 4.7. It can be seen that the Monte Carlo gives a good description of the data samples. Again, the effects of any differences between the Monte Carlo modelling and the data are studied with regards to the final corrected results and included in the systematic errors. This is found to be a very small effect compared to other sources (see section 5.3).

4.3.2 Selecting Identified Particle Species

From this sample of charged tracks, further selections and enhancements are then made to select charged kaon, pion and proton candidates.

The identification of the particle species is done using the dE/dx technique as discussed in Chapter 3. From equation 3.5, it can be seen that the error on the measurement of dE/dx for a given track is governed by the number of CJC hits used to reconstruct the dE/dx value for that track ($N_{dE/dx}$). And, from equation 3.11 it is clear that the separation between between the dE/dx of two particle candidates depends on this error which is minimised by requiring larger values of $N_{dE/dx}$. Figure 3.13 shows how the error $\sigma_{dE/dx}$ varies as a function of $N_{dE/dx}$ (lower curve). For this analysis, a cut is placed of $N_{dE/dx} > 20$ hits. This is

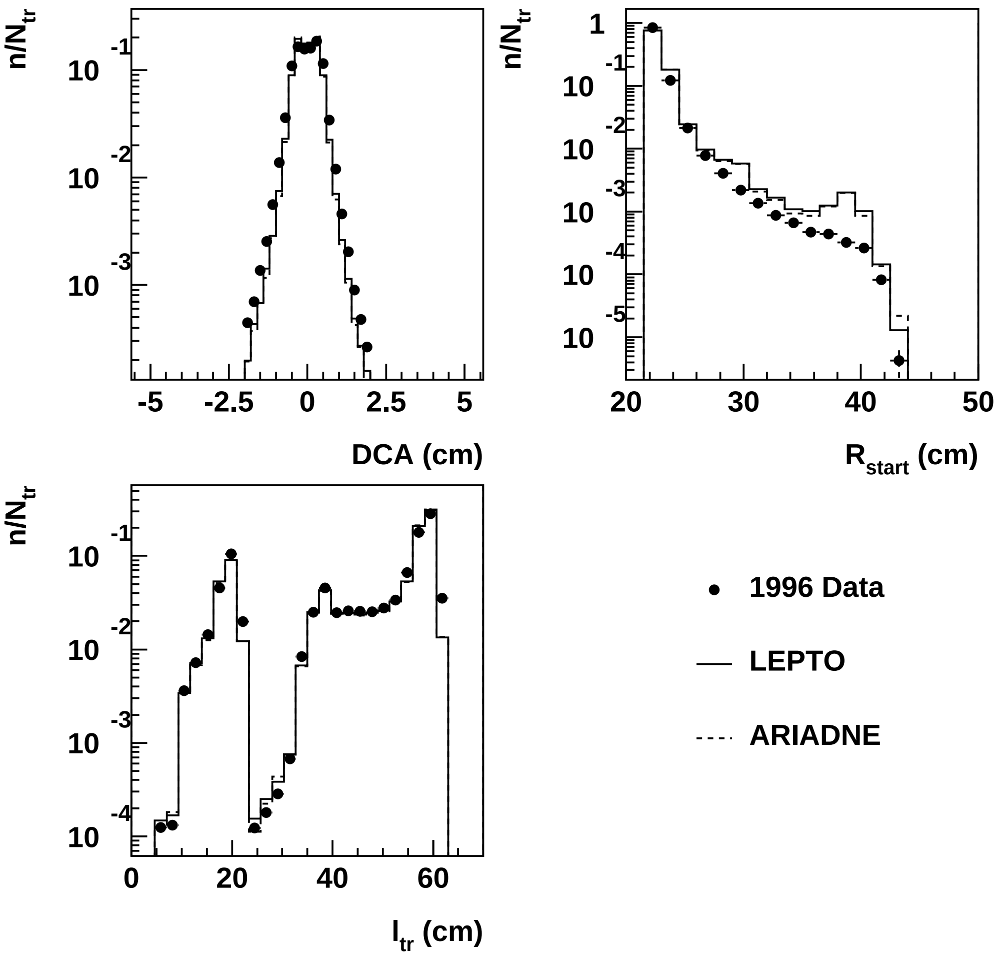

Figure 4.7: *Track quantities for 1996 data and reconstructed Django Monte Carlo. Shown are distance of closest approach, radius of track start point in the CJC and track length within the CJC.*

justified by the fact that it gives adequate separation between the particle species bands (see figure 4.9). While going to higher cut-off values slightly increases the separation power, this is also accompanied by a loss of a large portion of the data sample. Hence, the decision of $N_{dE/dx} > 20$ was thought to be an optimal value to use.

A comparison of data and Monte Carlo $N_{dE/dx}$ distributions shown in figure 4.8 indicates that the modeling of this variable is not performed precisely. Hence, a weight is applied to the Monte Carlo tracks calculated from a bin-by-bin re-weighting to data independently for different identified particle species and charges. The effect of this re-weighting procedure is studied as before by examining the effect on final corrected plots. The systematic effects discussed in section 5.3 for this are small compared to the dominant sources of systematic error. Figure 4.9 shows a scatter plot of all charged particles passing the selection cuts as a function of momentum and ionisation loss dE/dx. Overlayed onto the plots in figure 4.9 are the theoretical curves calculated from the reference function (equation 3.9) described in section 3.2.3. It can be seen that at lower momenta, the required particle species of kaons, pions and protons show a distinctive separation.

Before proceeding to explain the selection, it is necessary to examine the quality of the Monte Carlo modelling. Firstly, looking at figure 4.10, it can be seen that for the 3 particle species under consideration, the Monte Carlo models describe the dE/dx information well.

The errors on the dE/dx measurement for data and Monte Carlo calculated using equation 3.5 are shown in figure 4.11. As can be seen, the errors of Monte Carlo and data are broadly consistent with each other, although the Monte Carlo shows a slightly poorer dE/dx resolution.

Using equation 3.14, a cut is placed on LN_i of 0.1 to define the selection of a particle type. The LN_i distribution for data and Monte Carlo models is shown

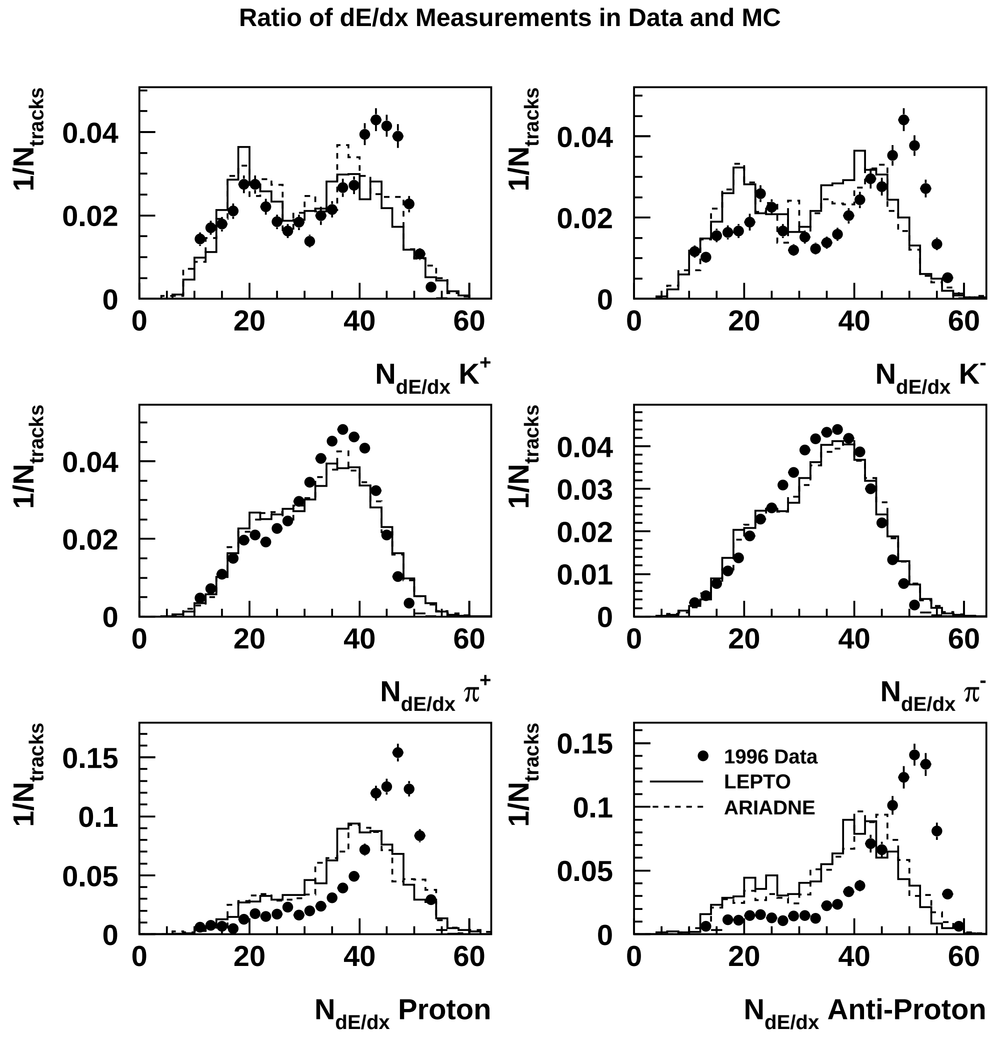

Figure 4.8: *Comparison of* $N_{dE/dx}$ *in data and Monte Carlo for kaons, pions and protons.*

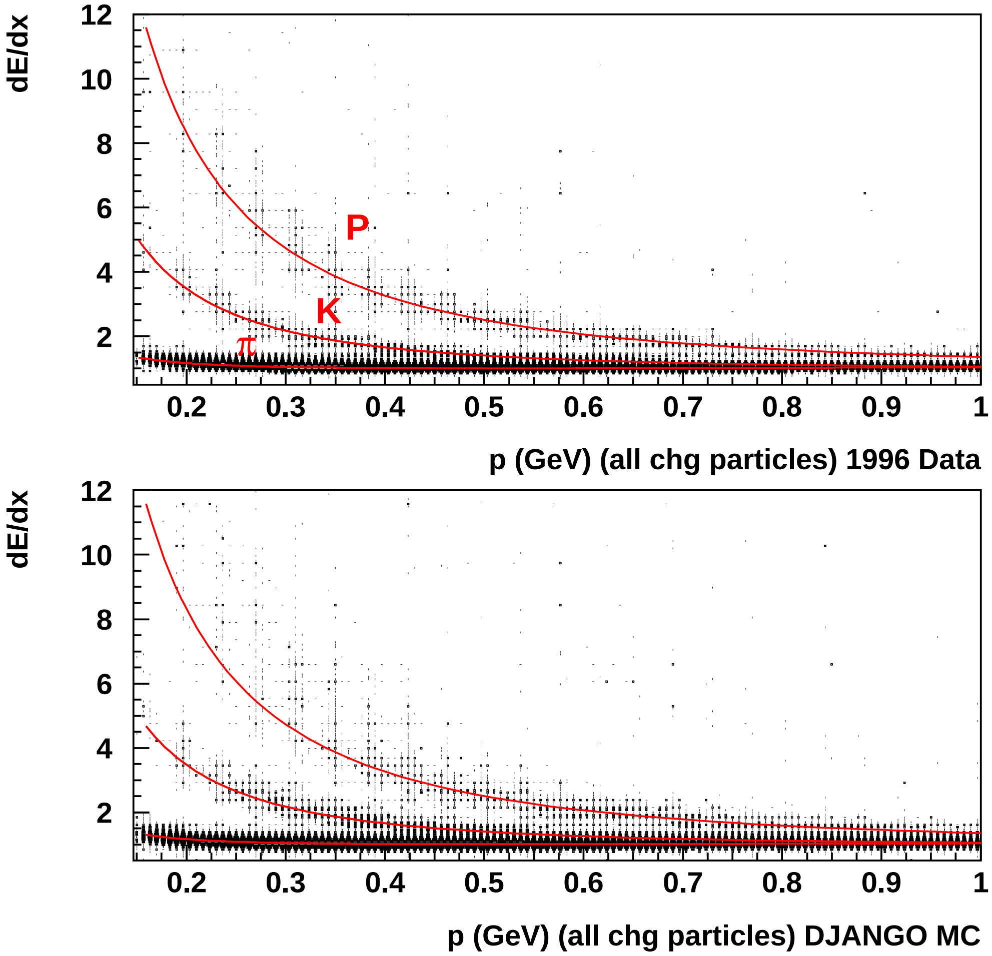

Figure 4.9: *Ionisation loss dE/dx vs. track momentum for 1996 data and Django Monte Carlo.*

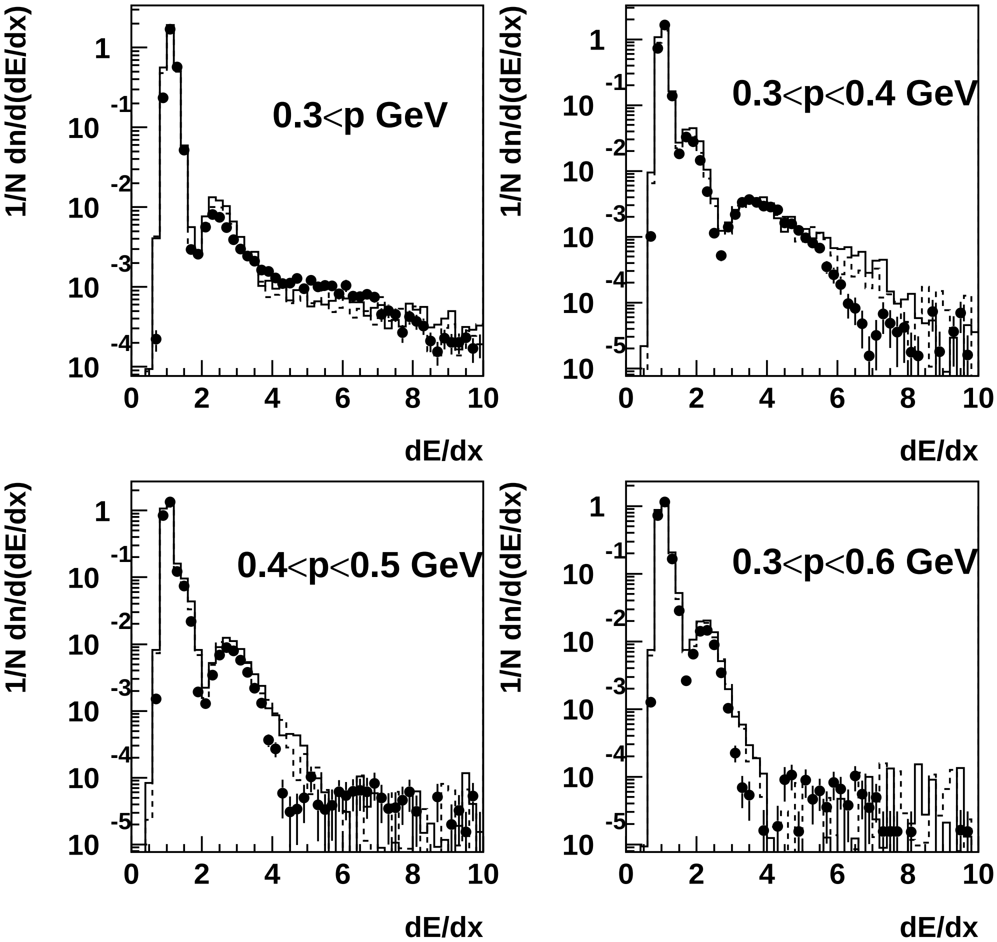

Figure 4.10: *dE/dx distributions for data and Monte Carlo.*

in figure 4.12. As can be seen, the shape of this distribution is well modelled. The differences in the peak height at $LN_i \sim 1$ for protons and to a lesser extent for kaons is due to the overestimations of these yields in the reconstructed Monte Carlo.

The purity of the tracks selected is calculated from Monte Carlo by counting the percentage of tracks identified as a particular particle species that were actually generated as such. This purity is plotted in figure 4.13 as a function of momentum for the individual particle types under consideration here. As can be seen, the purity remains very high at lower momenta. The cut-off for protons at

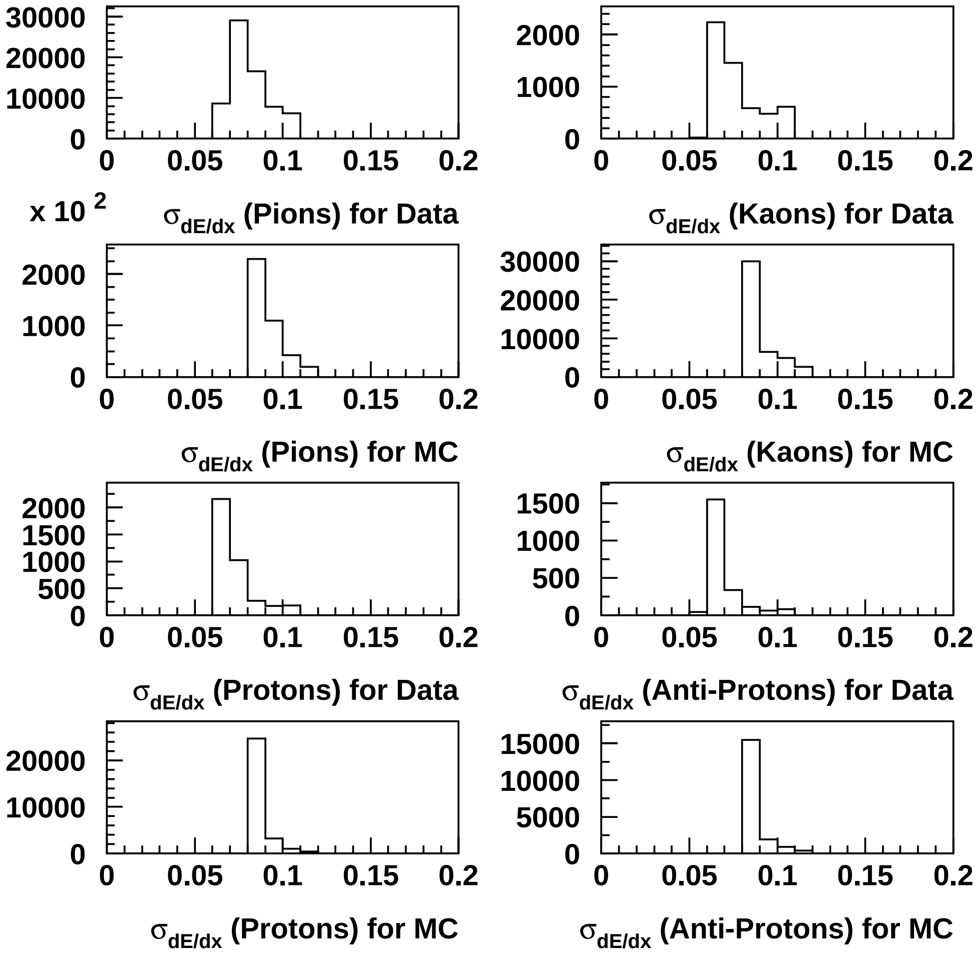

Figure 4.11: *Error on dE/dx measurements for data and Monte Carlo from equation 3.5.*

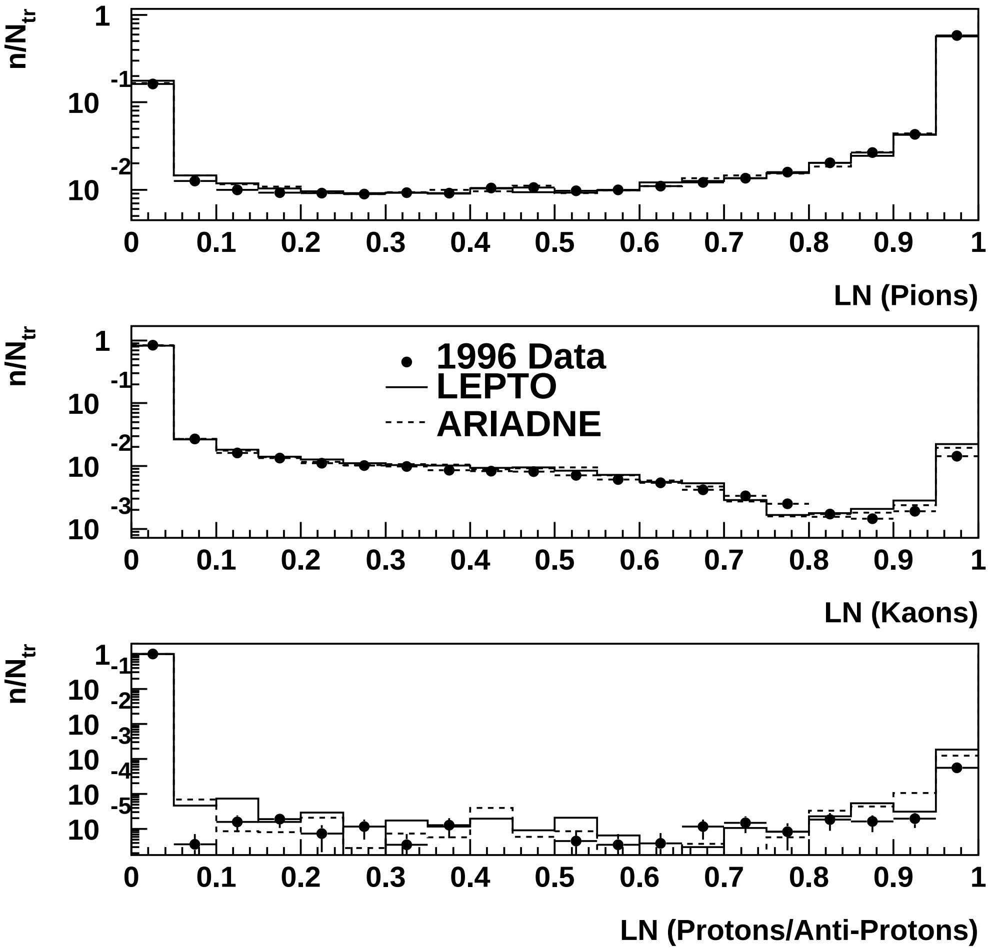

Figure 4.12: *LN_i distributions for data and Monte Carlo.*

0.3 GeV used in this analysis was chosen due to severe divergences between the different Monte Carlo models in this region. There is also a drop-off in purity towards higher momenta in kaons and protons due to contamination between particle species as the overlap region seen in figure 4.9 is entered. The lower purity for protons than antiprotons seen in figure 4.13 is not seen in other particle species, these ‘impure’ tracks correspond to proton background simulated in the reconstruction step. This can be demonstrated to be the case by looking at figure 4.14 which shows the distribution of the quantity $z - z_{vtx}$, which shows the distance in cm along the z-axis of the track intercept with the z-axis to the reconstructed event vertex position. The points with statistical error bars represent these ‘impure’ tracks from the proton purity plot, whilst the histogram represents all the identified proton tracks. It can be seen that the points describe purely the background of this distribution, which is the proton background discussed in 4.3.3.

It is principally from purity calculations that the following cuts are placed on the momentum phase space used for this analysis:

$$\begin{aligned} p < 0.5: &\quad K^{+/-}, \pi^{+/-} \\ 0.3 < p < 0.6: &\quad p, \bar{p} \end{aligned}$$

As a systematic check of this selection procedure, an alternate method is employed where, in the considered momentum regions, the particle species are selected by manually placing 2D cuts on figure 4.9 by eye. This method produces similar purities to those shown, apart from giving slightly poorer purities at the higher momenta values. Again, a systematic error is assigned to this effect based on the measured effect on the final corrected results. And, once more this was found to be minor with respect to the dominant sources.

For clarity, a summary of the event and track cuts and selections is displayed in table 4.2.

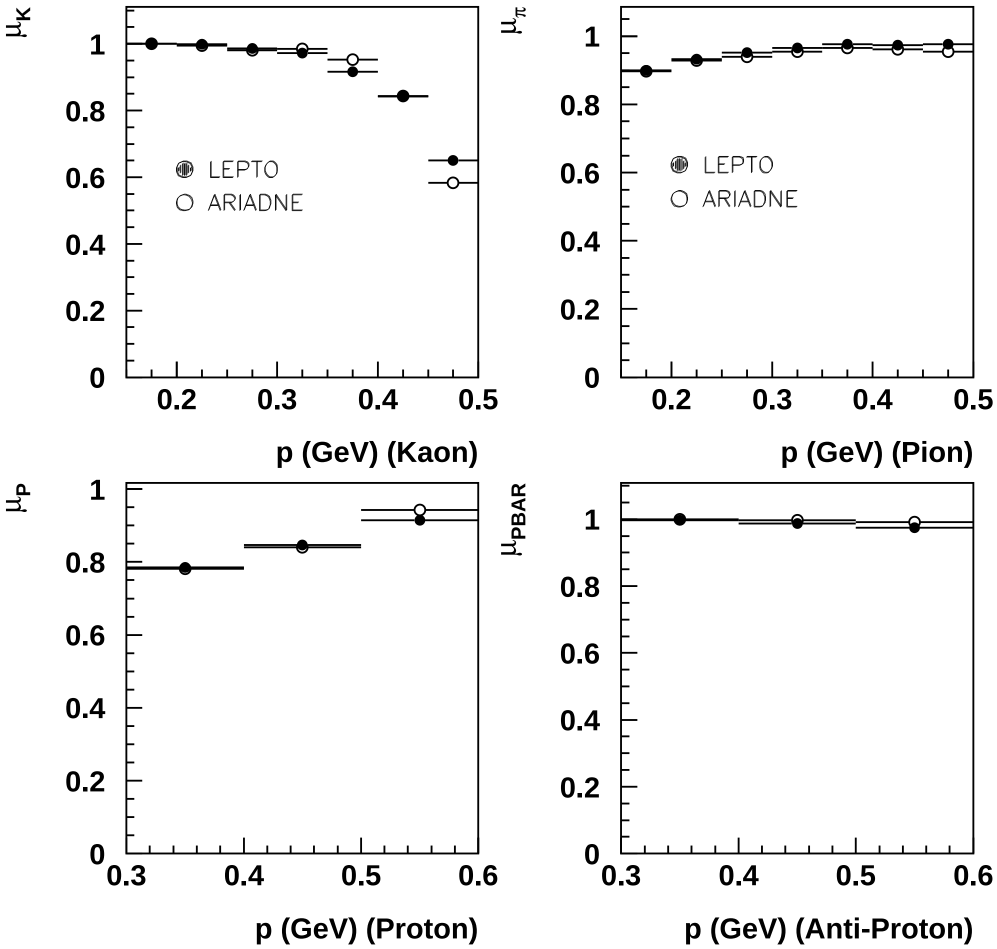

Figure 4.13: *Purity of kaon,pion and proton samples as a function of momentum.*

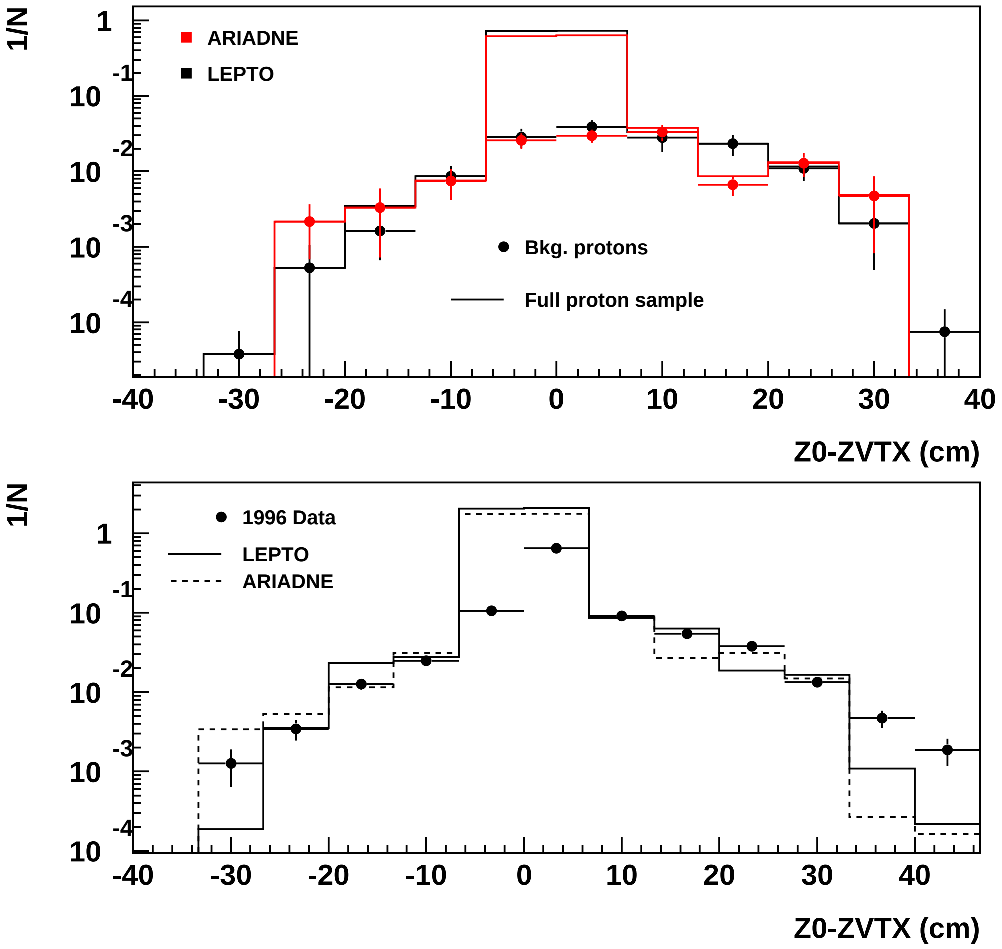

Figure 4.14: *The distance along the z-axis of the track intercept on this axis from the event vertex position. Plotted are reconstructed identified proton tracks from Monte Carlo (histogram) and background (points) in the top plot. The bottom plot shows the shape normalised distributions for data and Monte Carlo superimposed upon each other.*

4.3.3 Treatment of Proton Background

Special consideration needs to be applied to the proton selections due to a background source which exists when hadrons from the *ep* collision interact strongly with the material of the beam pipe or CJC walls. A way of reducing contamination of spallation protons from this material is, firstly, to accept hadronic events which contain only exactly one proton or one antiproton. In the photo-production studies of [28], this was found to reduce the background from secondary protons by more than 60%.

Whilst the Monte Carlo models do incorporate this background (as can be seen from figure 4.14), due to the incorrect GEANT modelling of these low momenta protons (as reported in [28]) they incorrectly estimate the level. To correct for this, a fitting procedure to the $z0 - z_{vtx}$ distributions in data in different momenta ranges is carried out. From these (see figure 4.15), the ratio $\frac{sig.}{sig.+bkg.}$ is calculated by fitting two gaussian distributions to model the signal and background. An event weight is then used in the Monte Carlo based on the ratio:

$$\frac{\left(\frac{sig.}{sig.+bkg.}\right)_{MonteCarlo}}{\left(\frac{sig.}{sig.+bkg.}\right)_{Data}}. \tag{4.3}$$

in the different momenta regions shown. Table 4.1 shows these figures along with the derived errors from the fits that enter the analysis as a systematic error (see 5.3).

A final effect needing consideration is that of the modelling of the absorption cross-sections of protons and antiprotons passing through the beam-pipe. In [28], it was announced that GEANT incorrectly models these cross-sections and a weighting of 2% was applied to the antiproton samples. Here, the same procedure is followed.

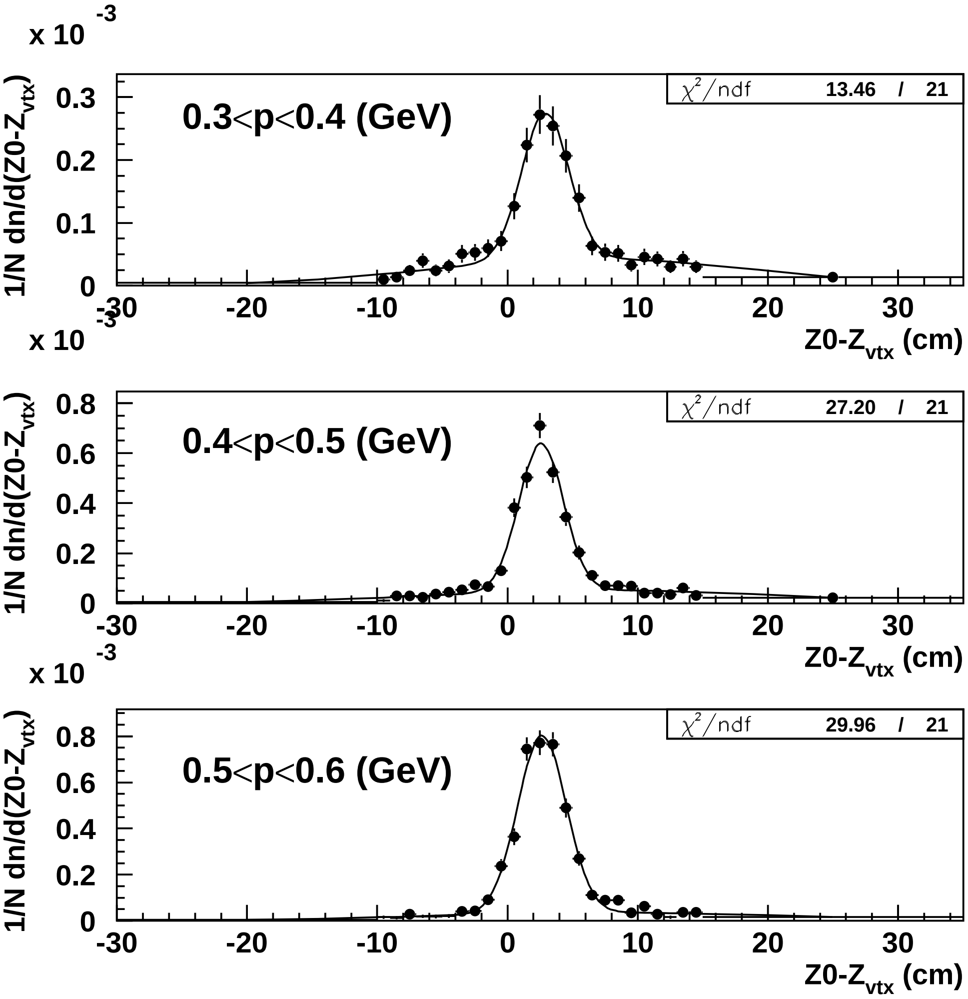

Figure 4.15: *Z-vertex track intercept position from reconstructed interaction vertex for 1996 Data. Shown are two gaussian fits for signal and background in three momentum bins.*

Momentum Range (GeV)	Monte Carlo Event Weight
0.3-0.4	1.639 ± 0.206
0.4-0.5	1.379 ± 0.191
0.5-0.6	1.205 ± 0.106

Table 4.1: *Monte Carlo event weights to correct for proton background from equation 4.3.*

4.3.4 Beam-Gas Background

The H1 ToF and veto counters (see 2.7) are designed to choose events originating near the nominal interaction point, and thus eliminate a great deal of events occurring through the collision of a beam particle with residual particle gas in the beam-pipe. The cut introduced in 4.1 of $\sum E - p_z$ also further reduces any proton beam particle initiated beam-gas interactions. To estimate the level of lepton beam initiated interactions of this type which may effect the physics results of this analysis, the z-vertex position cut introduced in 4.1 is relaxed. As these interactions are equally likely along the z-axis, a flat distribution is expected in z. This can indeed be observed to be the case (figure 4.2) beyond the cut region in the z-vertex position. A simple extrapolation of this distribution under the cut region reveals that only a small proportion of events are likely to originate from such interactions in this analysis $\mathcal{O}(few\ \%)$.

As an additional check, the proton results were examined under the influence of cuts requiring the presence of considerable forward energy. These events cannot originate from electon initiated beam gas interactions, and no change in the results indicating a bias from such beam gas events was detected.

Event-level selections
1996+1997 low Q^2 DIS ep data and Django Monte Carlo
$E_{e'} > 10$ GeV
$156^o < \theta_{e'} < 177^o$
$R_{cl,e'} < 3.5$ cm
$35 < \sum_j E_j - p_{zj} < 70$ GeV
$D_{tr,cl} < 3.5$ cm
use s001 sub-trigger
exclude runs:
$<$ 157877 & 166000-168820 (1996)
Use kinematic range:
$5 < Q^2 < 70\ GeV^2$
$10^{-5} < x < 10^{-2}$
$0.1 < y < 0.6$
Track-level selections
use tracks from central tracking chambers
$p_T > 0.15$ GeV
$\lvert DCA\rvert < 2$ cm
$r_{tr,start} < 50$ cm
$l_{tr} > 10$ cm
$N_{dE/dx} > 20$
$p < 0.5$ GeV $(k^{+/-}, \pi^{+/-})$
$0.3 < p < 0.6$ GeV $(p, \bar{p})$

Table 4.2: *Event and track selections used for kaon, pion and proton analyses.*

Chapter 5

Corrected Kaon, Pion and Proton Spectra

Spectra of the samples of identified charged kaons, pions[1] and protons selected by the methods described previously are presented here. These spectra are corrected for detector acceptance and resolution effects as well as effects due to possible initial-state QED radiation in the event.

5.1 Observables and Kinematic Regions Used

The corrected spectra are differentially plotted rates of the particle species in terms of their transverse momenta squared p_T^{*2} and pseudo-rapidity η^* in the CMS frame for the kaon and pion samples. The proton and antiproton samples are presented as functions of transverse momenta p_T and pseudo-rapidity η in the LAB reference frame. The rates plotted are defined below, normalised by the number of DIS events N passing the selection cuts defined in section 4.2 and the bin width.

$$K^{+/-}, \pi^{+/-} \quad : \quad \frac{1}{N}\frac{dn}{dp_T^{*2}, \eta^*} p, \bar{p} \quad : \quad \frac{1}{N}\frac{dn}{dp_T, \eta} \tag{5.1}$$

---

[1] The kaon and pion spectra are the sums of kaon+antikaon and pion+antipion respectively

The kaon and pion samples are plotted in the preferred way for theoretical comparison by being in the proton-photon rest frame. For the protons and antiprotons, it was necessary to plot spectra in the LAB frame due to excessive kinematic phase space acceptance corrections when working in the CMS frame. This is essentially a mass effect, where the higher proton mass effectively smears its tracks out in the kinematic phase spaces where these cuts are made.

Also presented are spectra of the $K^{+/-}/\pi^{+/-}$ ratio, which gives a better handle on the production of strange quarks compared to lighter u and d quarks.

The quantity A_B defined below in terms of observed numbers of protons (N_p) and antiprotons ($N_{\bar{p}}$), used in [31], as a measure of baryon asymmetry is also presented differentially in p_T, p_{tot} and η, and also as a function of the number of charged particles visible in the event.

$$A_B = \frac{2.(N_p - N_{\bar{p}})}{(N_p + N_{\bar{p}})} \tag{5.2}$$

To keep detector acceptance corrections within acceptable limits, samples of kaons and pions are restricted to and corrected back to the following regions of phase space[2]:

$$2.5 < p^* < 4.0 \text{ GeV}$$
$$p_T^* < 0.5 \text{ GeV}$$

The proton samples are plotted and corrected to the rapidity and momentum interval:

$$-1 < \eta < 1$$
$$0.3 < p < 0.6$$

To study the effect of kinematics on the plotted spectra, all quantities are presented in 7 bins of x and Q^2. These are shown below in table 5.1 with the mean values of x, Q^2, W in these bins and the η^* regions for the kaon and pion samples plotted.

---

[2] The $*$ denotes the CMS frame

Bin	$Q^2 (GeV^2)$	$x \times 10^{-3}$	η^*	$< Q^2 >$	$< x >$	$< W >$
0	5-70	0.01-10	2.5-3.5	14.8	0.76	158
1	5-9.5	0.093-0.22	2.25-3.25	6.4	0.16	200
2	5-9.5	0.22-1.5	2.5-3.5	6.9	0.43	134
3	9.5-20	0.1-0.6	2.5-3.5	12.8	0.40	185
4	9.5-20	0.6-3	2.75-3.75	14.3	0.99	124
5	20-70	0.2-1.5	2.75-3.75	30.3	0.97	182
6	20-70	1.5-10	3.25-4.25	40.9	2.6	130

Table 5.1: *Kinematic bins used in analysis.*

5.2 Unfolding Procedure

The data, having been corrected for triggering effects as described in 4.2.2 are now subject to an unfolding procedure to correct for the effects of finite detector resolution and acceptance. The influence of initial-state QED radiation is also taken into account here. A bin-by-bin method is used where a correction factor is computed for each bin used in the spectra under consideration.

The following method is used to correct the spectra measured from the data:

1. Two samples of events are generated using the LEPTO and ARIADNE Monte Carlo model programs. These generated events include the effects of QED radiation. To emulate the hadronic final state seen in the detector; final state photons are merged with the scattered positron if closer than five degrees and events with an initial state photon of more than 3 GeV energy and $\theta > 178^o$ are rejected. The quantities described in 5.1 are formed at this level, collectively referred to as $R_{gen,rad}$.

2. The event samples from (1) are now subject to full H1 detector simulation and reconstruction. The reconstructed Monte Carlo models are now treated in the same fashion as the data sample and the quantities described in section 5.1 are formed, $R_{rec,rad}$.

3. Two more sets of Monte Carlo events are generated: one including QED

radiation effects, the other set without. These have the level of hadronic events described in (1). The derived quantities from these samples are referred to as $R_{gen2,rad}$ and $R_{gen2,norad}$.

The correction factors $C_{a,i}$ and $C_{b,i}$ are now calculated for the bins i of all the measured distributions. The factor $C_{a,i}$ corrects for the effects of limited resolution and acceptance of the H1 detector and is calculated by dividing the distributions obtained in (1) to those in (2), which gives:

$$C_{a,i} = \frac{R_{gen,rad,i}}{R_{rec,rad,i}} \tag{5.3}$$

The QED radiative effects are corrected using $C_{b,i}$, again bin-by-bin for all measured distributions. This factor is calculated by taking the ratio of the distributions in (3):

$$C_{b,i} = \frac{R_{gen2,norad,i}}{R_{gen2,rad,i}} \tag{5.4}$$

Using the product of these bin correction factors, all the measured distributions are corrected:

$$R_{corr,i} = C_{a,i}.C_{b,i}.R_{uncorr,i} \tag{5.5}$$

To determine the accuracy of the Monte Carlo to perform this correction, two different models are utilised. The correction factor used in equation 5.5 is the average value from the two models (LEPTO and ARIADNE). The difference between the correction factors calculated from these models is propagated through to the final distributions and is the model dependence systematic error. This is the dominant source of systematic error in this analysis.

Figures 5.1 and 5.2 show the calculated correction factors for the measured kaon, pion and proton spectra. As can be seen, due to the phase space restrictions described in section 5.1, all correction factors are kept within acceptable limits ($\approx 0.5 - 2.0$). This means that no large reliance on the Monte Carlo to correct for detector effects is present. As can be seen, the correction for QED effects are small ($\lesssim 10\%$). Note here that statistical errors for the calculation of $C_{b,i}$ (small due to the use of a large number of generated Monte Carlo events) are included amongst the systematic errors.

Also shown in figure 5.3 are the correction factors for proton and antiproton total momentum and rates as a function of charged particle multiplicity; used for the comparison of A_B with other results (see section 5.4.2).

The bin-by-bin correction method as used here is adequate so long as the bin-to-bin migrations are not too big. To study the size of bin migrations, the following bin purity is defined for each bin in the measured distributions:

$$\mu_i = \left(\frac{N_{gen+rec,i}}{N_{rec,i}} \right) \tag{5.6}$$

where, $N_{rec,i}$ is the number of entries in bin i found in the reconstructed Monte Carlo models after all selections. $N_{gen+rec,i}$ is the number of these entries in bin i which stem from the same bin as the level of generated hadrons.

The bin purities for all distributions are shown in figures 5.4 and 5.5 for both the Monte Carlo models used in the correction procedure (LEPTO & ARIADNE). All bins fulfill the minimum criterion of having greater than 40% purity.

5.3 Systematic Uncertainties

The sources of systematic uncertainties considered in this analysis are the following:

- Model dependence of correction procedure (see 5.2).
- Statistical errors from correction factors for QED effects (see 5.2).
- Varying event and track cut parameters.
- Choice of dE/dx particle identification method (see 4.3.2).
- Effect of re-weighting $N_{dE/dx}$ distributions.

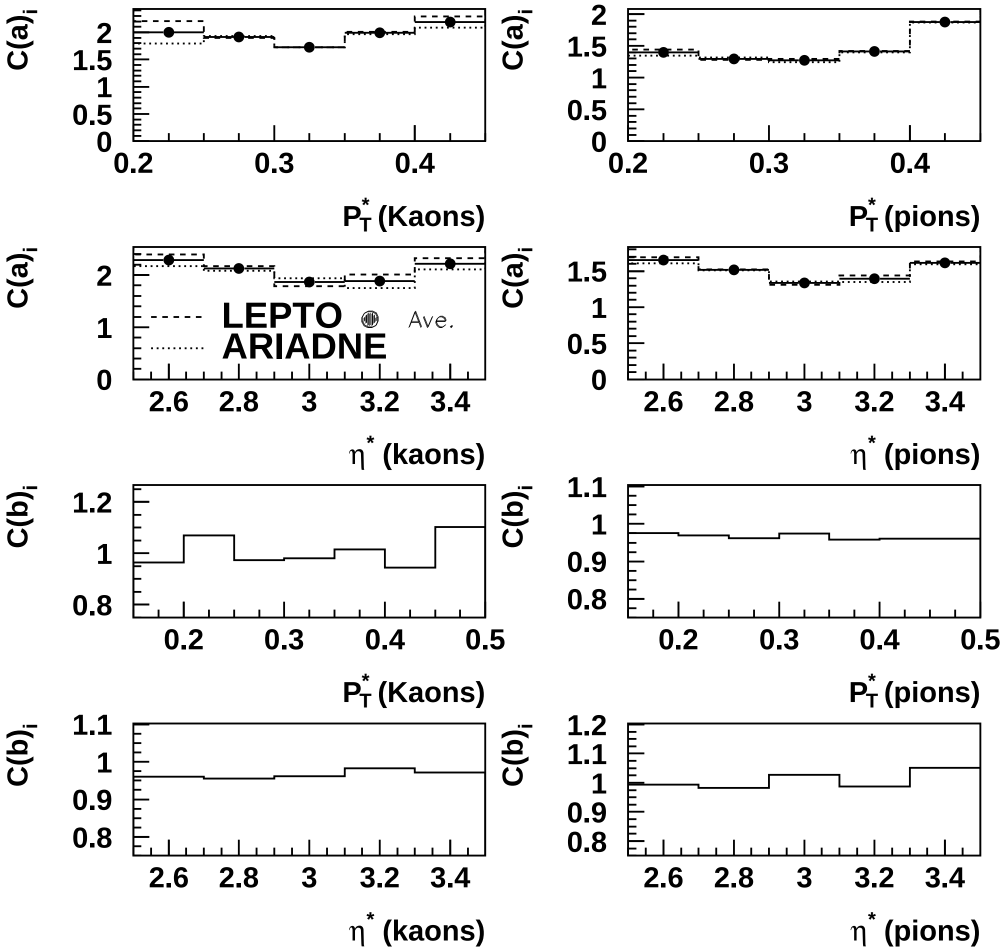

Figure 5.1: *Detector and QED correction factors for kaon and pion measured pseudo-rapidity and transverse momentum spectra (CMS frame). The factors C(a) are the detector correction factors; C(b) are the QED radiation corrections.*

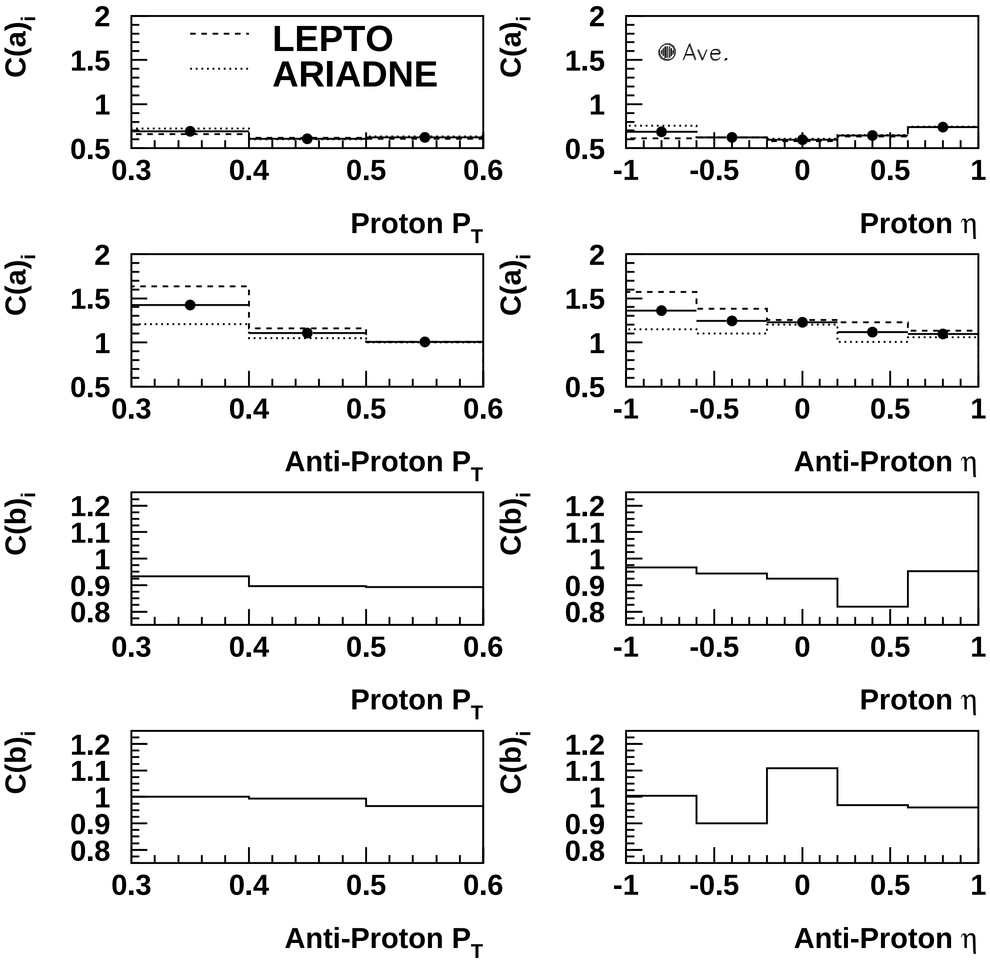

Figure 5.2: *Detector and QED correction factors for proton and antiproton measured rapidity and transverse momenta spectra (LAB frame). The factors C(a) are the detector correction factors; C(b) are the QED radiation corrections.*

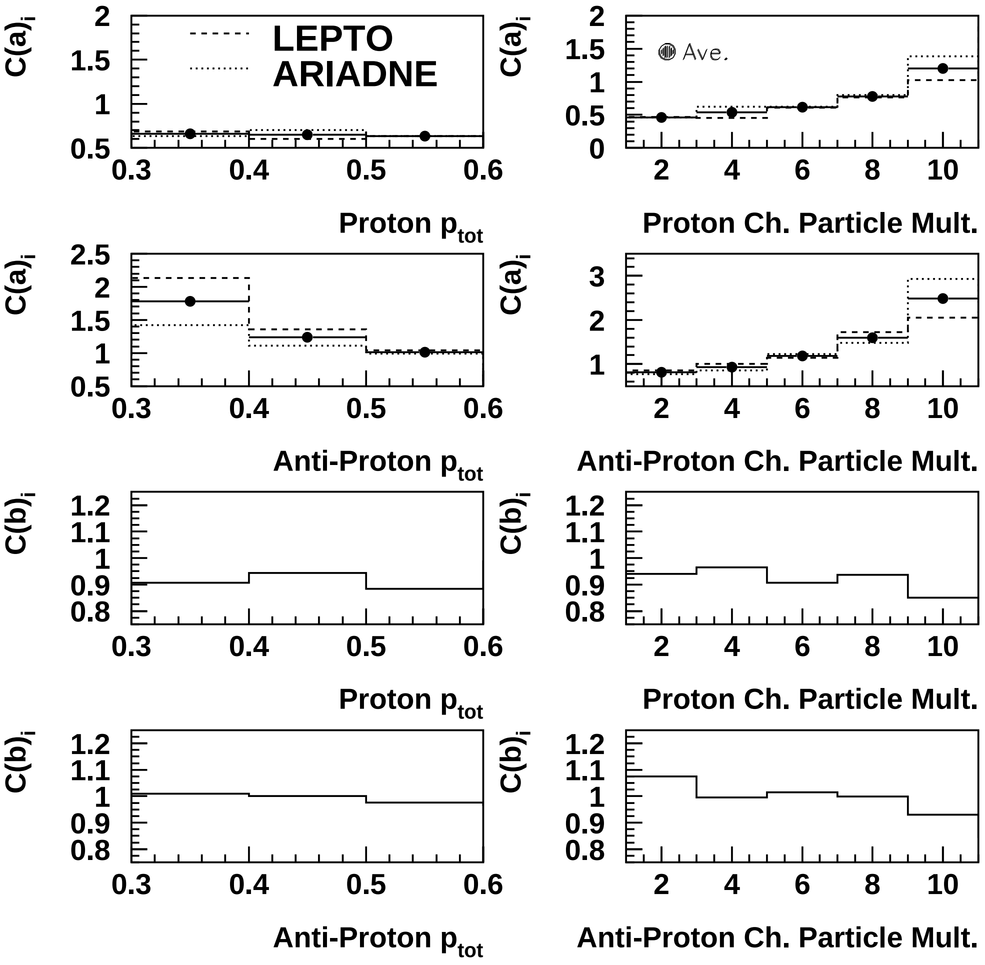

Figure 5.3: *Detector and QED correction factors for proton and antiproton measured total momenta spectra and rates as a function of charged track multiplicity (LAB frame). The factors C(a) are the detector correction factors; C(b) are the QED radiation corrections.*

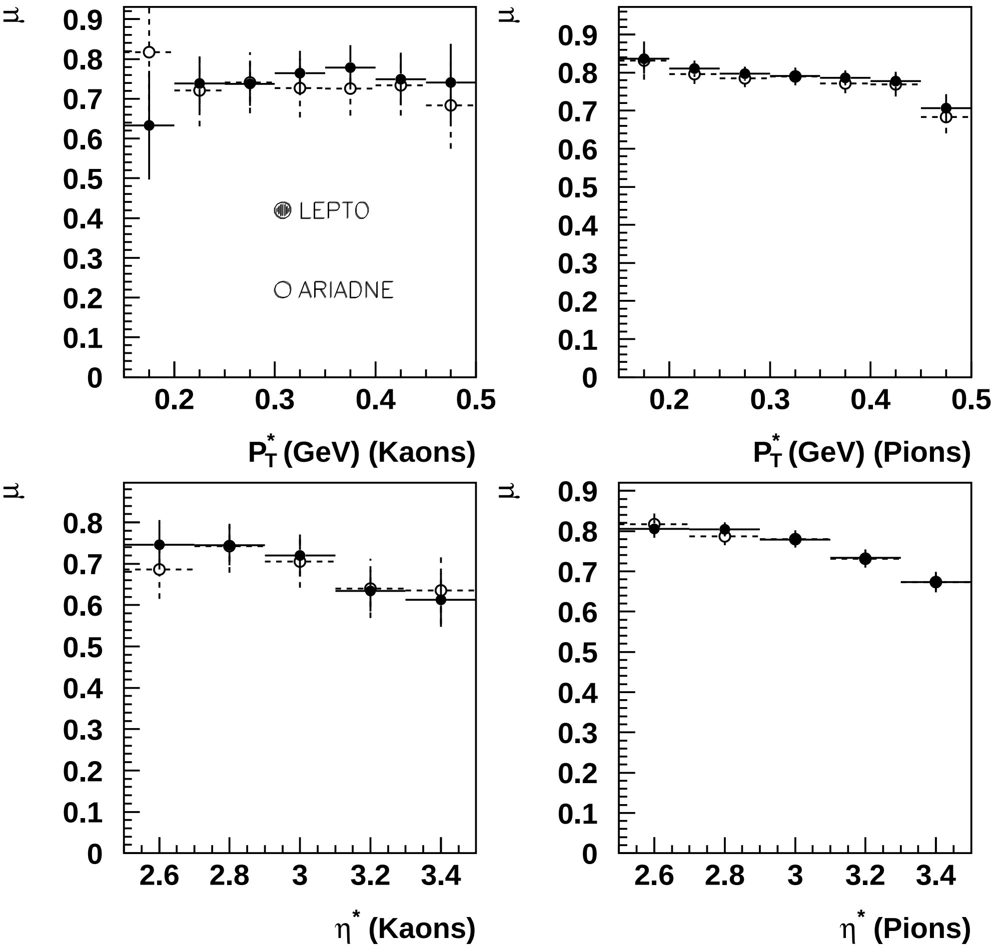

Figure 5.4: *Bin purities for the kaon and pion distributions as defined from LEPTO and ARIADNE Monte Carlo models. The bin purity measures the number of events identified in bin i that were generated there.*

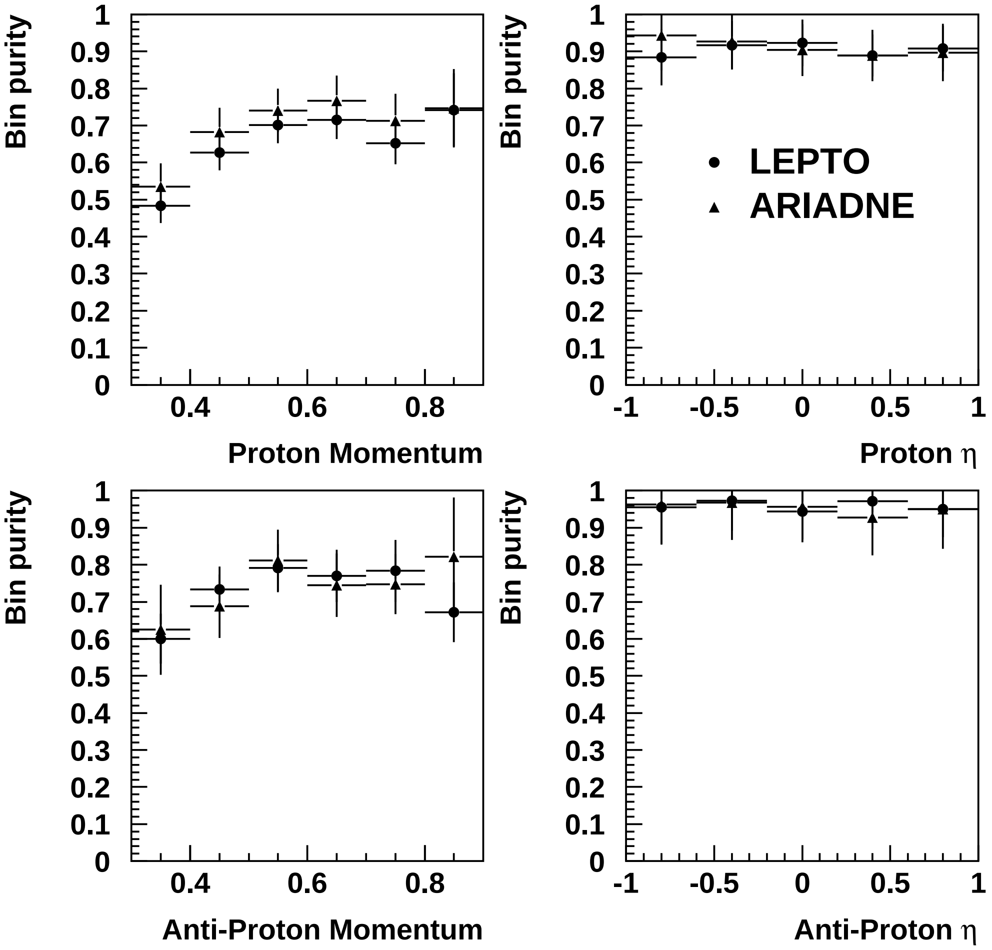

Figure 5.5: *Bin purities for the proton distributions as defined from LEPTO and ARIADNE Monte Carlo models. The bin purity measures the number of events identified in bin i that were generated there.*

- Choice of s001 or s002 sub-trigger (see 4.2.2).
- Effect of re-weighting some track and event selection distributions (see 4.2).
- Effect of possible asymmetric ϕ distribution of tracks in CJC.
- Uncertainty of SPACAL electromagnetic energy scale.
- Background from photo-production events (see 4.2).
- Effects of re-weighting of proton yields (see 4.3.3).

The following paragraphs describe how the influence of those systematic uncertainties are calculated that are not described elsewhere as indicated in the above list. Table 5.2 then summarises the typical effect the systematic effects have on the results. The list of systematic uncertainties are then added in quadrature for each bin to obtain the total systematic error for all the distributions measured.

Variance of track/event cut parameters

All the cuts described together with their distributions in chapter 4 are varied by a few percent around the cut value, corresponding to the typical measurement resolution for that variable. By measuring the corresponding systematic error on the final corrected results, this shows how sensitive the results are on these applied cuts.

Asymmetric ϕ distributions

Due to inefficiencies in the CJC, the observables examined in the analysis may not be perfectly symmetric in ϕ. This was found to be the case, with an asymmetry present between tracks measured in the upper and lower sections of the CJC. This effect was found not to be perfectly well modelled by the reconstructed Monte Carlo. A systematic error is thus obtained by measuring the difference in final physics results performing the analysis separately in the different CJC segments.

Uncertainty of the SPACAL electromagnetic energy scale

The energy of the scattered positron is exclusively measured in the SPACAL

Source of Systematic Uncertainty	Typical Effect on Measured Dists.(%)		
	Kaons/Pions	Protons	A_B
Model dependence of corrections	1-10	1-15	5-20
Varying track & event cuts	2-6	1-5	10-60
Choice of dE/dx particle ID	1-6	< 1	0-1
dE/dx re-weighting	1-3	1-10	15-80
Event/track distribution re-weighting	0-3	1-4	10-80
Choice of trigger correction method	3-8	2-8	10-80
Phi asymmetry effect	2-8	3-8	15-40
SPACAL EM scale uncertainty	1-4	0-1	2-8
Photo-production background	< 1	< 1	< 1
Proton correction uncertainties	-	8-12	40-100
Total Effect	7-14	8-20	60-100+

Table 5.2: *Sources of systematic errors and typical effects based on kaon, pion and proton/A_B spectra.*

which has a scale uncertainty of less than 1%. This energy measurement is included in the event selections and also used to calculate the boost vector to plot measurements in the CMS frame. Therefore, to study what effect the uncertainty in this measurement will have, the scattered positron energy is artificially shifted by ±1% in the data. The effect this has on the final corrected results is included in the list of systematic uncertainties and is small.

Photo-production background

Events entering this analysis from photo-production processes (as described in section 4.2) constitute a background source and is studied using a sample of photo-production Monte Carlo events (generated with PHOJET [50]). After the DIS selection procedure described in section 4.2, this contribution to the systematic errors is negligible.

5.4 Corrected Distributions and Interpretation

With the complete selection, identification and correction procedures carried out as described, we can now examine the identified particle spectra for the variables introduced earlier. In this section, the spectra for $K^{+/-}$, $\pi^{+/-}$ and the $K^{+/-}/\pi^{+/-}$ ratio are shown in the CMS frame for each kinematic bin listed in table 5.1. Also presented are the spectra for p, $\bar{p}$ in the LAB frame for the bins in table 5.1. The asymmetry measurement A_B is presented in p_T, p_{tot}, η and charged track multiplicity.

These corrected results are then compared with a number of Monte Carlo models, briefly described below.

5.4.1 Phenomenological QCD Models

The following Monte Carlo models are used in this analysis to compare with the data, giving a handle on the fundamental physics processes involved.

DGLAP inspired models

The LEPTO [51] and HERWIG [52] Monte Carlo programs implement $\mathcal{O}(\alpha_s)$ matrix elements with QCD partonic showering based on DGLAP splitting functions (see section 1.1.7). In LEPTO, the Lund string model as implemented in JETSET [13] is used to convert the partonic final state from LEPTO into the observable hadronic final state. HERWIG differs from LEPTO in that it also considers interference effects due to colour coherence and uses the cluster fragmentation model (see section 1.2.5).

The Colour Dipole Model

As described in section 1.2.3, an alternative description to the parton cascade picture used in LEPTO and HERWIG is the colour dipole model (CDM). In the CDM, a colour dipole formed originally between the struck quark and proton remnant emits partons. Colour dipoles spanned between the newly created colour charges and the original ones emit subsequent gluon radiation. Gluon emissions

Parameter	Description	Default Value	DELPHI Value
PARJ(2)	λ_s (strangeness suppression)	0.3	0.23
PARJ(11)	Prob. meson has spin 1 (u,d)	0.5	0.365
PARJ(12)	Prob. meson has spin 1 (s)	0.6	0.410

Table 5.3: *Values of some JETSET hadronisation parameters associated with u,d and s quark production.*

from this cascade are not ordered in k_T, causing the CDM to resemble a BFKL-like parton emission chain (see section 1.1.8). The ARIADNE [53] Monte Carlo program implements the CDM.

Tuning of JETSET parameters

Using the findings of the DELPHI collaboration studies of K^0s and other light resonances; the JETSET parameters shown in table 5.3 are used which described their data [55]. Hence, the Monte Carlo models utilising JETSET used for data comparison are labelled LEPTO-D and ARIADNE-D to signify this tuning is incorporated.

5.4.2 Corrected Spectra and Physics Results

Charged Kaons and Pions

Measurements are presented here of the differential transverse momentum squared $\left(\frac{1}{N}\frac{dn}{dp_T^{*2}}\right)$ and pseudo-rapidity $\left(\frac{1}{N}\frac{dn}{d\eta^*}\right)$ spectra in the hadronic centre of mass system (see section 2.10), for which the incoming photon direction defines the $+z^*$ direction[3]. The kaon and pion measurements are made in the high experimental acceptance range: $p_T^* < 0.5$ GeV, $2.5 < p^* < 4.0$ GeV and one unit of η^* in the range $2.25 < \eta^* < 4.25$ depending on the kinematical bin, as shown in table 5.1.

In order to investigate the evolution of u,d and s production with the kinematics of the ep scattering, the distributions are presented in one bin which covers the full kinematic range under study here (bin 0) and a further 6 independent

---

[3] Where quantities in this frame are denoted by *

bins in x and Q^2 (shown in table 5.1). The ratio $K^{+/-}/\pi^{+/-}$ is also shown in all of these bins to give a more direct view on the production of s over lighter u and d quarks.

The transverse momentum squared spectra for kaons and pions in bin 0 only is shown in figure 5.6. The pseudo-rapidity spectra for kaons and pions in this bin are shown in figure 5.7. Figure 5.8 shows the transverse momentum squared and pseudo-rapidity spectra of the kaon/pion ratio. Figures 5.10 to 5.15 show the kaon, pion and kaon/pion transverse momenta and pseudo-rapidity distributions in all the kinematic bins. In all of these figures, the corrected data are shown along with the predictions of ARIADNE-D, LEPTO-D and HERWIG. The data are compared to ARIADNE with the DELPHI tuning and with the default tuning of the JETSET parameters of table 5.3 in figure 5.9.

In all plots, the inner error bars represent the 1σ statistical errors, and the outer error bars are the statistical and systematic errors added in quadrature.

The transverse momentum distribution for kaons in figure 5.6 peaks in the 0.25-0.3 GeV p_T bin and falls off towards higher p_T. ARIADNE-D agrees well with the data here, LEPTO-D over-estimates the strangeness yield in all bins, HERWIG greatly over-estimates the strangeness yield and also incorrectly models the shape of the distribution. The pion distribution peaks in the lowest p_T bin and again falls off at higher p_T. Here, LEPTO-D seems to best describe the data in the lowest two p_T bins, whilst ARIADNE-D describes the data best in the other three bins. HERWIG, here too greatly over-estimates the yield and incorrectly models the shape of the distribution.

The same message is repeated in the pseudo-rapidity distributions shown in figure 5.7, with the best descriptions again coming from the ARIADNE-D and LEPTO-D Monte Carlo models.

Figure 5.8, showing the kaon/pion ratio distributions, reveals once again a better description from the ARIADNE-D and LEPTO-D Monte Carlo models than from HERWIG. Here though, ARIADNE-D and LEPTO-D seem to slightly under-estimate the slopes of the distributions, whilst ARIADNE-D seems to give the better description of the two in terms of yield. This would seem to indicate that the rate of strangeness production increases quicker with p_T and decreases more quickly with pseudo-rapidity than predicted with the QCD models.

It is interesting to note in these distributions, the sensitivity shown by the data to the two models, LEPTO-D and ARIADNE-D. Using the same hadronisation process, these models essentially differ in the way they handle the partonic evolution of the ep scattering interaction (see section 5.4.1). It would appear from the data, that the colour dipole model of ARIADNE is preferred over the leading-log parton showering process of LEPTO; with the DELPHI tuned JETSET parameters in place.

The effect of using the DELPHI tuned JETSET parameters over the LUND default ones is demonstrated in figure 5.9. As shown, the effect of this tuning is to lower these distributions by $\approx 20\%$ which subsequently gives a considerably better description of the data. This shows a preference in this data to a lower strangeness suppression value than the LUND default of 0.3 that is roughly consistent with the DELPHI tuned value for $\lambda_s = 0.23$.

Looking at the kaon and pion transverse momenta spectra in all the kinematic bins shown in figures 5.10 and 5.11: the peak of the distributions are seen to shift right slightly with increasing x (moving from left to right in the plots) and to shift left slightly with increasing Q^2 (moving from bottom to top in the plots). The picture of agreement with Monte Carlo doesn't change with changing kinematics, although in the high-x, high-Q^2 bin (bin 6), the LEPTO-D and ARIADNE-D seem to under-estimate the yield seen in data. The kaon/pion ratio transverse momentum spectra is seen to steadily rise in all the plots in figure 5.12, with approximately the same average ratio seen in all of the bins. The pseudo rapidity spectra for kaons and pions displayed in figures 5.13-5.15 appear to be invariant throughout all the kinematic bins shown, and similar agreement with Monte

Carlos is seen in all plots.

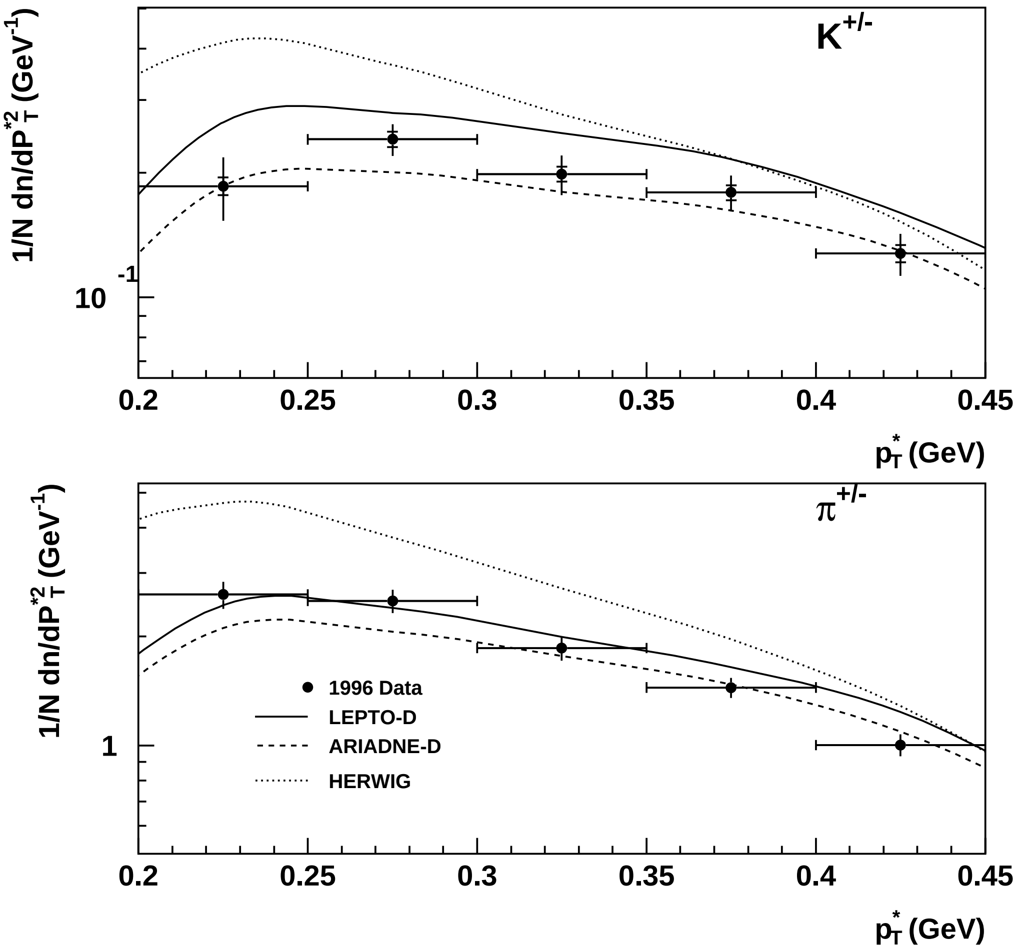

Figure 5.6: *Transverse momentum spectra for charged kaons and pions in kinematic bin 0 (from table 5.1). Shown are 1996 corrected data points together with Monte Carlo predictions of ARIADNE-D, LEPTO-D and HERWIG. All quantities are measured in the* γp *CMS frame.*

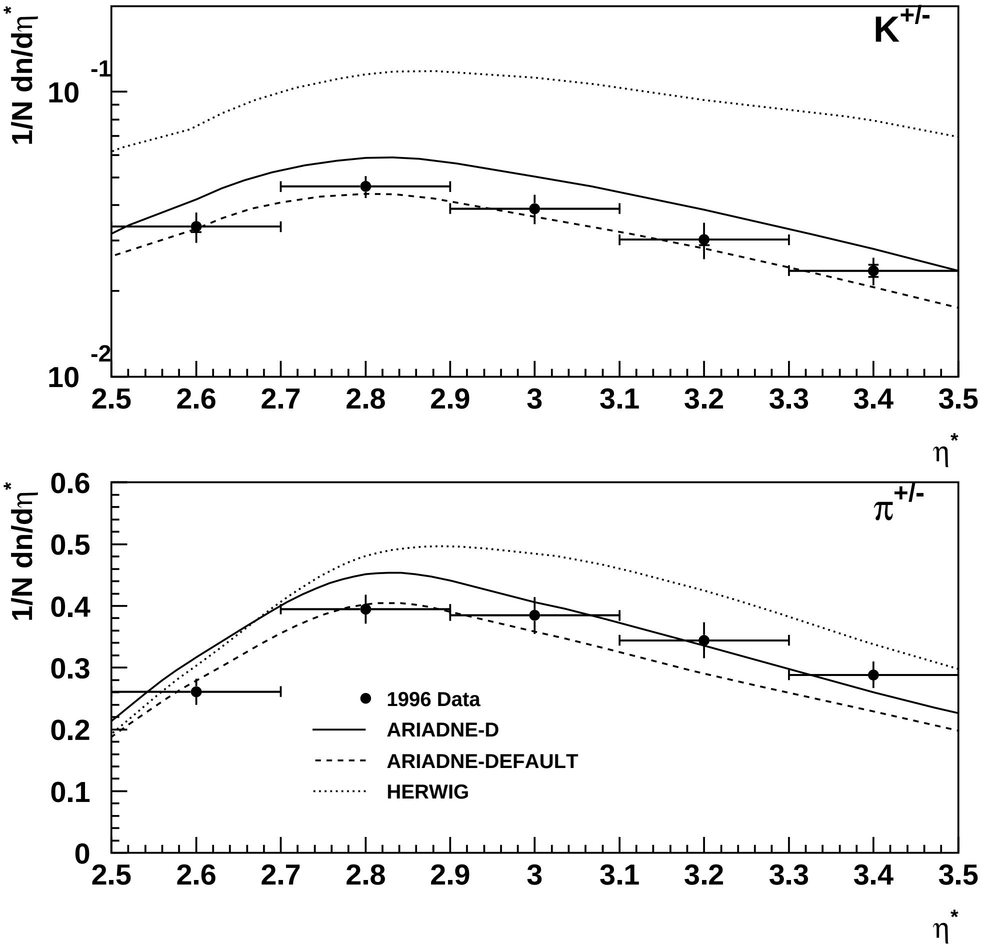

Figure 5.7: *Pseudo-rapidity spectra for charged kaons and pions in kinematic bin 0 (from table 5.1). Shown are 1996 corrected data points together with Monte Carlo predictions of ARIADNE-D, LEPTO-D and HERWIG. All quantities are measured in the γp CMS frame.*

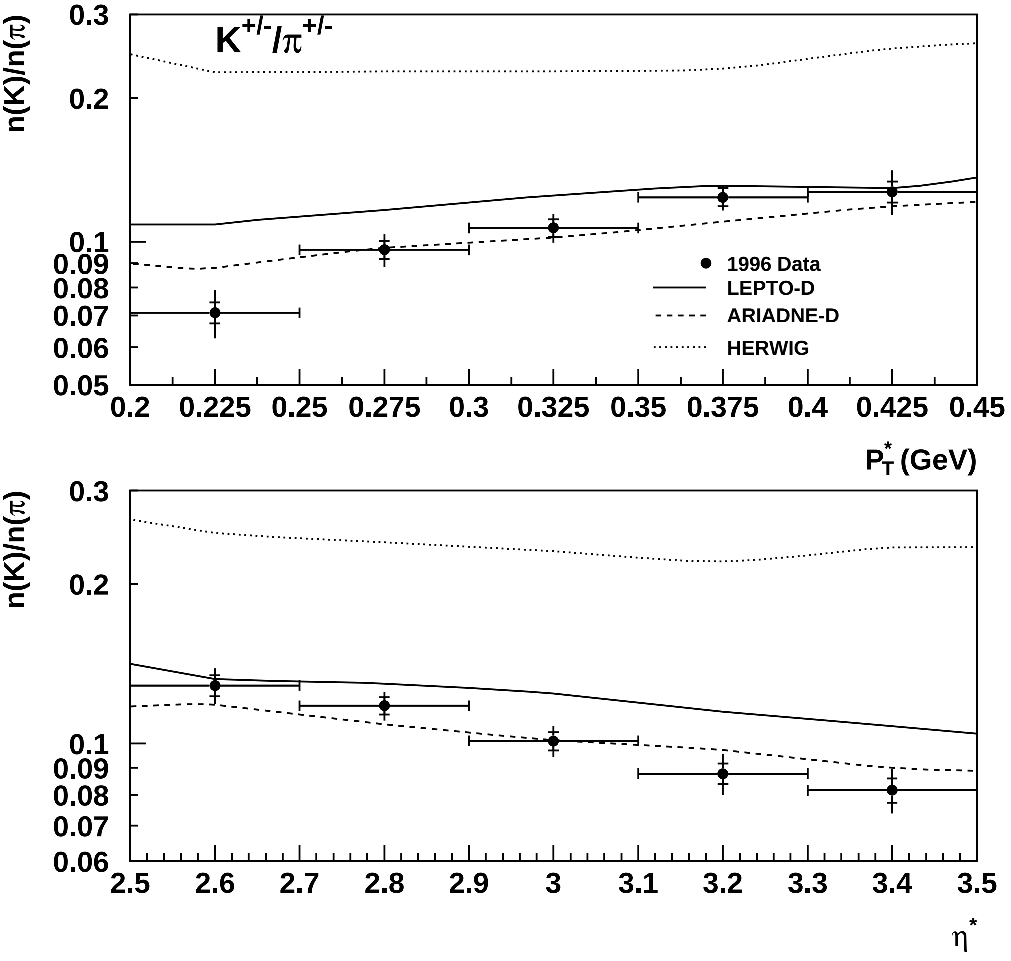

Figure 5.8: *Transverse momentum and Pseudo-rapidity spectra for the charged kaon/pion ratio in kinematic bin 0 (from table 5.1). Shown are 1996 corrected data points together with Monte Carlo predictions of ARIADNE-D, LEPTO-D and HERWIG. All quantities are measured in the* γp *CMS frame.*

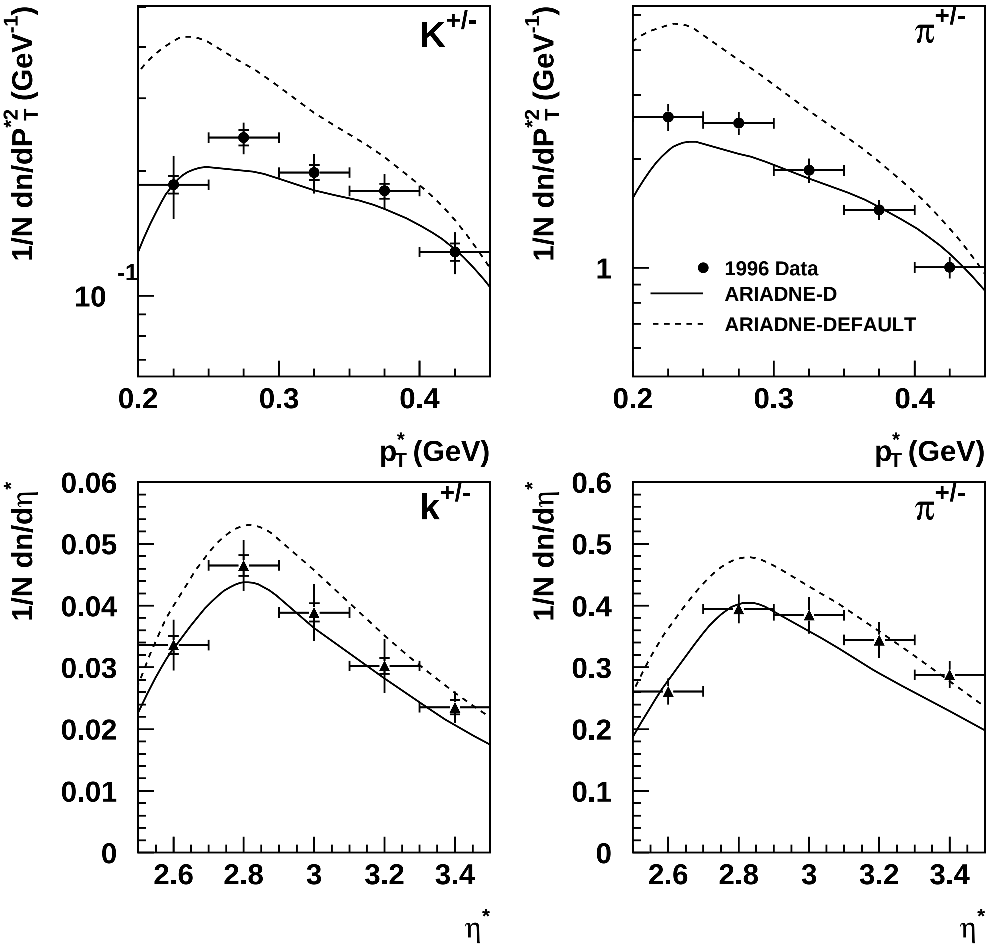

Figure 5.9: *Transverse momentum and Pseudo-rapidity spectra for the charged kaons and pions in kinematic bin 0 (from table 5.1). Shown are 1996 corrected data points together with Monte Carlo predictions of ARIADNE-D, and ARIADNE with the default tuning parameters of JETSET shown in table 5.3. All quantities are measured in the* γp *CMS frame.*

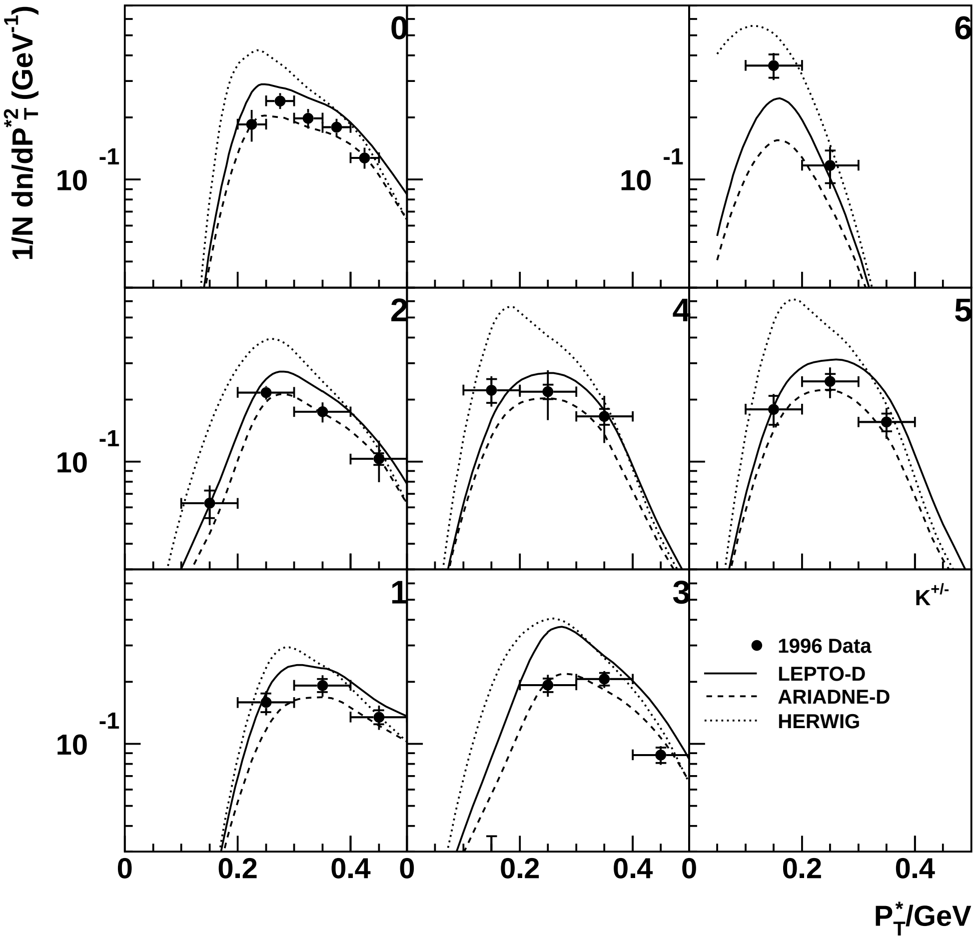

Figure 5.10: *Transverse momentum spectra for charged kaons for all kinematic bins in table 5.1. Shown are 1996 corrected data points together with Monte Carlo predictions of ARIADNE-D, LEPTO-D and HERWIG. Plotted in the H1 CMS frame. The numbering of the plots corresponds to the bin numbers of table 5.1, apart from bin 0, the plots are arranged with increasing* x_{Bj} *along the x-axis and increasing* Q^2 *up the y-axis.*

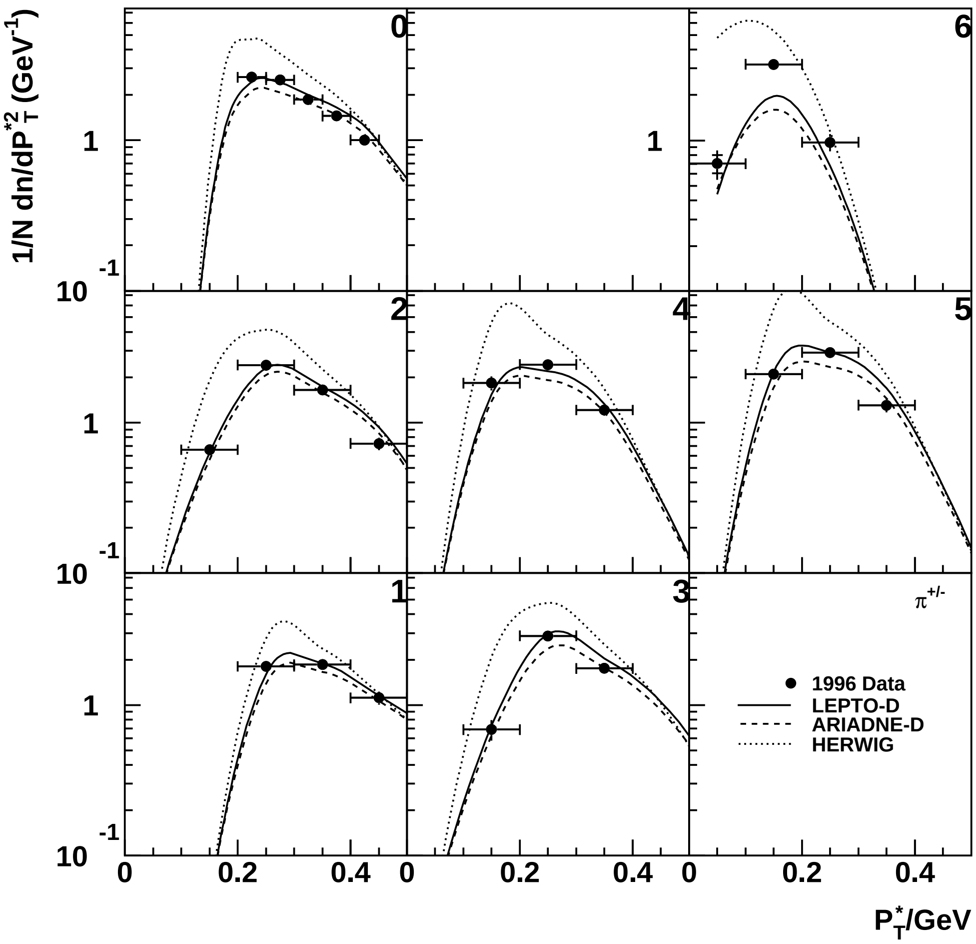

Figure 5.11: *Transverse momentum spectra for charged pions for all kinematic bins in table 5.1. Shown are 1996 corrected data points together with Monte Carlo predictions of ARIADNE-D, LEPTO-D and HERWIG. Plotted in the H1 CMS frame. The numbering of the plots corresponds to the bin numbers of table 5.1, apart from bin 0, the plots are arranged with increasing* x_{Bj} *along the x-axis and increasing* Q^2 *up the y-axis.*

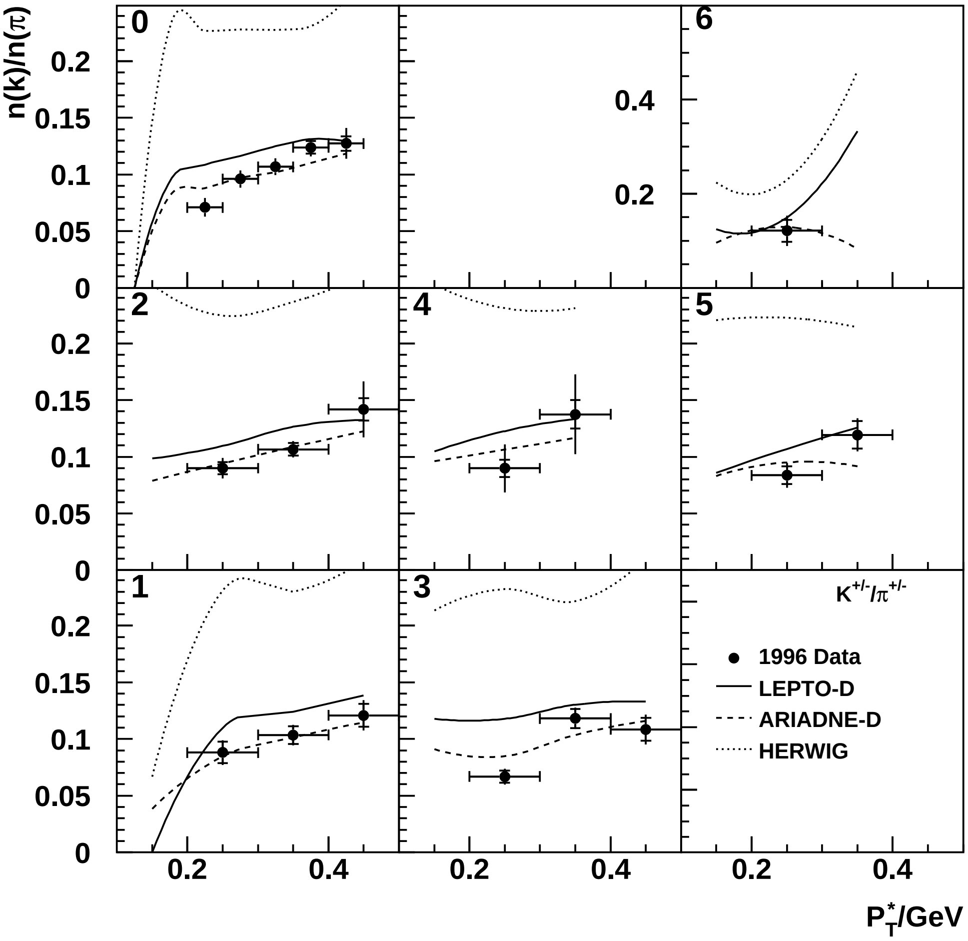

Figure 5.12: *Transverse momentum spectra for the charged kaon/pion ratio for all kinematic bins in table 5.1. Shown are 1996 corrected data points together with Monte Carlo predictions of ARIADNE-D, LEPTO-D and HERWIG. All quantities are measured in the γp CMS frame. The numbering of the plots corresponds to the bin numbers of table 5.1, apart from bin 0, the plots are arranged with increasing x_{Bj} along the x-axis and increasing Q^2 up the y-axis.*

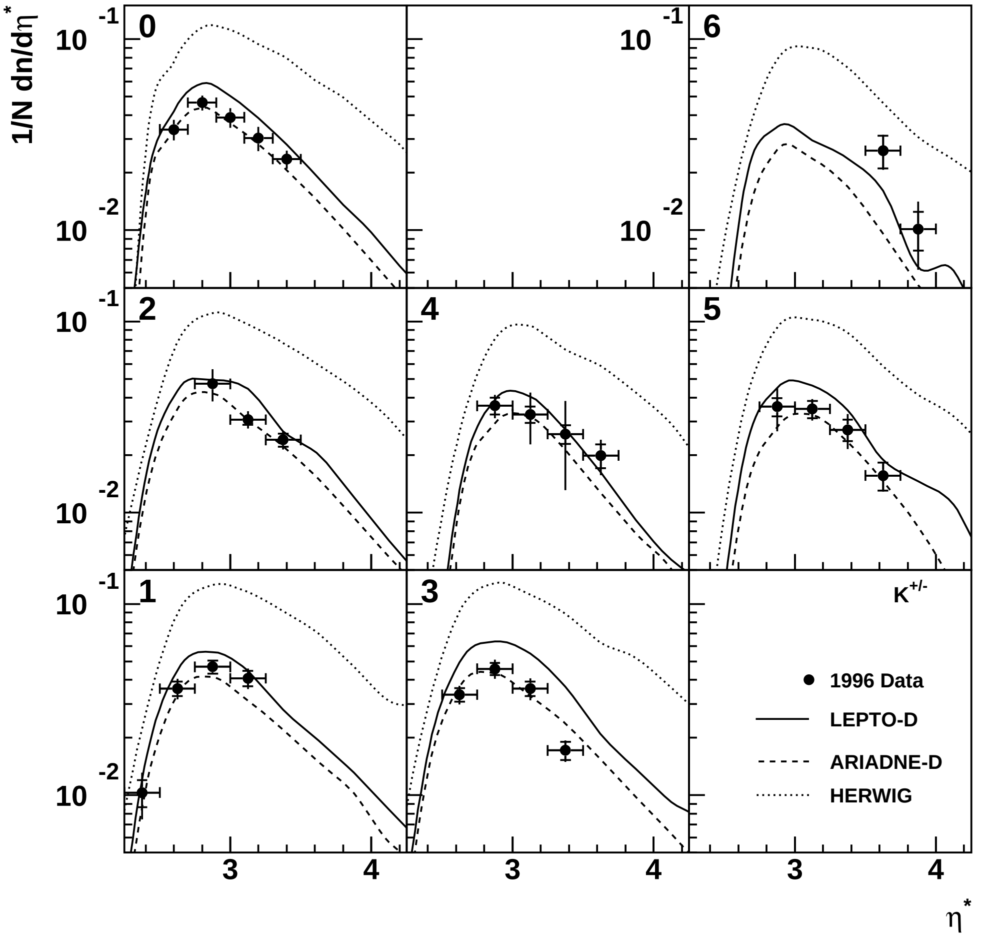

Figure 5.13: *Pseudo-rapidity spectra for charged kaons for all kinematic bins in table 5.1. Shown are 1996 corrected data points together with Monte Carlo predictions of ARIADNE-D, LEPTO-D and HERWIG. Plotted in the H1 CMS frame The numbering of the plots corresponds to the bin numbers of table 5.1, apart from bin 0, the plots are arranged with increasing* x_{Bj} *along the x-axis and increasing* Q^2 *up the y-axis.*

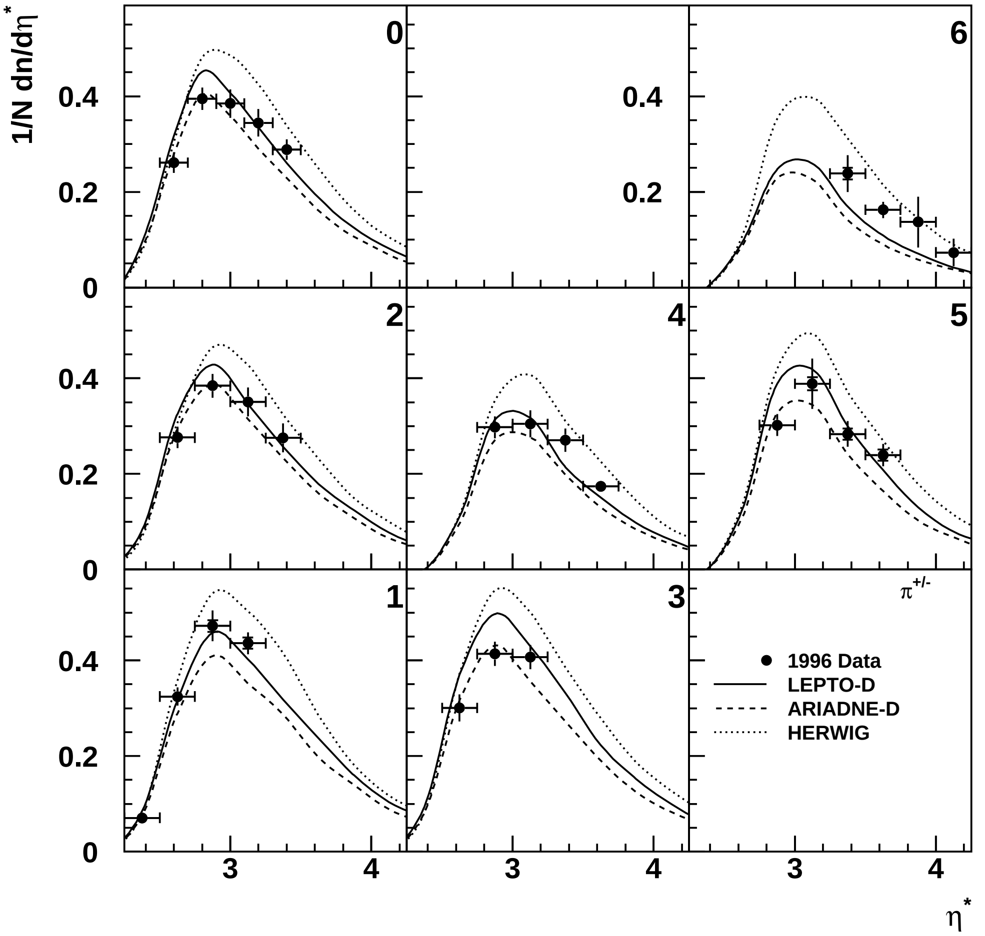

Figure 5.14: *Pseudo-rapidity spectra for charged pions for all kinematic bins in table 5.1. Shown are 1996 corrected data points together with Monte Carlo predictions of ARIADNE-D, LEPTO-D and HERWIG. Plotted in the H1 CMS frame. The numbering of the plots corresponds to the bin numbers of table 5.1, apart from bin 0, the plots are arranged with increasing* x_{Bj} *along the x-axis and increasing* Q^2 *up the y-axis.*

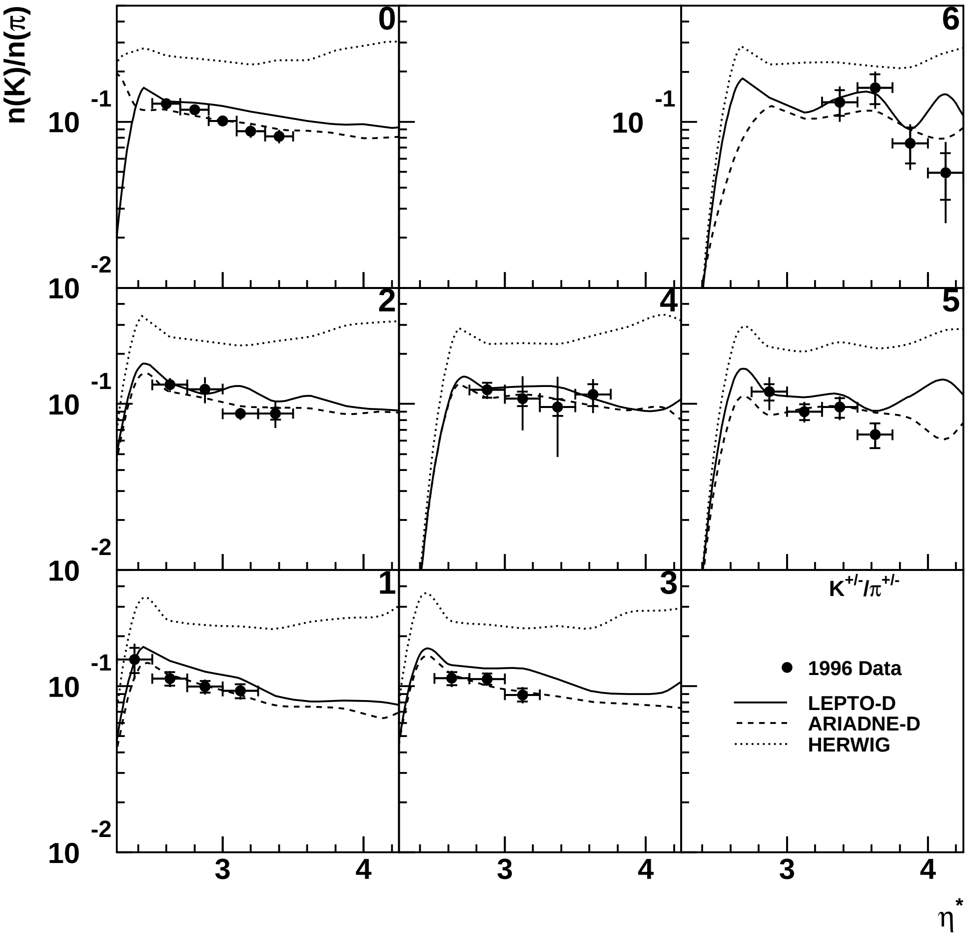

Figure 5.15: *Pseudo-rapidity spectra for the charged kaon/pion ratio for all kinematic bins in table 5.1. Shown are 1996 corrected data points together with Monte Carlo predictions of ARIADNE-D, LEPTO-D and HERWIG. All quantities are measured in the γp CMS frame. The numbering of the plots corresponds to the bin numbers of table 5.1, apart from bin 0, the plots are arranged with increasing x_{Bj} along the x-axis and increasing Q^2 up the y-axis.*

Protons and Antiprotons

Measurements here are presented of the differential transverse momentum $\left(\frac{1}{N}\frac{dn}{dp_T}\right)$ and pseudo-rapidity $\left(\frac{1}{N}\frac{dn}{d\eta}\right)$ spectra of p and $\bar{p}$ in the H1 laboratory frame (see section 2.10), in which the beam proton determines the positive z direction. The measurements are made in the high experimental acceptance range: $-1 < \eta < 1$ and $0.3 < p < 0.6$ GeV. This range in rapidity is several units away from the proton remnant system.

The p and $\bar{p}$ transverse momentum and pseudo-rapidity spectra are shown in figure 5.16, with the same shown for all kinematic bins in figures 5.17 and 5.18. The corrected data points are shown, together with the predictions from ARIADNE-D, LEPTO-D and HERWIG. The model predictions shown are the average of the proton and antiproton points, as the only difference between these is statistical (no $p\bar{p}$ asymmetry is predicted by the models).

Also shown, is an asymmetry variable composed of the $p(\bar{p})$ rate per event $N_p(N_{\bar{p}})$: $A_B = \frac{2.(N_p - N_{\bar{p}})}{N_p + N_{\bar{p}}}$ which is shown in figure 5.19 as a function of transverse momentum, pseudo-rapidity, total momentum and charged track multiplicity. Also shown for comparison are the results obtained from the photo-production studies of [28] in the total momentum and charged track multiplicity distributions.

In all plots, the inner error bars represent the 1σ statistical errors, and the outer error bars are the statistical and systematic errors added in quadrature.

The proton and antiproton p_T distributions shown in figure 5.16 peak in the lowest p_T bin and fall off towards higher p_T. The shape of these distributions is described by all the QCD-based models, however, they all significantly over-estimate the yields. ARIADNE-D is the nearest to the correct yield, HERWIG is furthest away. The same is true of the modelling of the pseudo rapidity distributions shown in the same figure. This over-estimation by the Monte Carlo models based on string fragmentation could be due to the suppression of baryon production in the fragmentation process at these low-x values as discussed in section 1.4.

A similar picture is seen in all the kinematic bins studies, as shown in figures 5.17 and 5.18. In all plots, the QCD models over-estimated the proton and antiproton yields, with no significant change in shape of the spectra.

The differences between proton and antiproton yields are shown more demonstratively in the A_B spectra shown in figure 5.19. The asymmetry is seen to decrease with both transverse and total momenta, with no clear dependence seen in either pseudo-rapidity or charged track multiplicity. The trend in total momentum is in agreement with the results shown in photo-production measurements [28]. The increase with charged track multiplicity observed in [28] is not seen here however. As discussed in section 1.4, both the measurements shown from [28] are in agreement with the theoretical predictions of [31] which uses a gluonic mechanism for the propagation of baryon number.

The integrated proton-antiproton asymmetry was measured to be:
$A_B(DIS) = 0.071 \pm 0.018(\textit{stat.}) \pm 0.091(\textit{stat.+sys.})$
which compares to the photo-production result [28] of:
$A_B(\gamma P) = 0.08 \pm 0.01(\textit{stat.}) \pm 0.025(\textit{stat.+sys.})$
and the theoretical prediction from [31] of $A_B = 0.07$.

Unfortunately, due to the large experimental uncertainties in the measurement of A_B in this analysis, it is not possible to claim a significant proton-antiproton asymmetry here. These systematic effects seem to be larger then might be expected due to the fact that, in many of the systematic sources investigated, the proton and antiproton systematic effects appear to be uncorrelated.

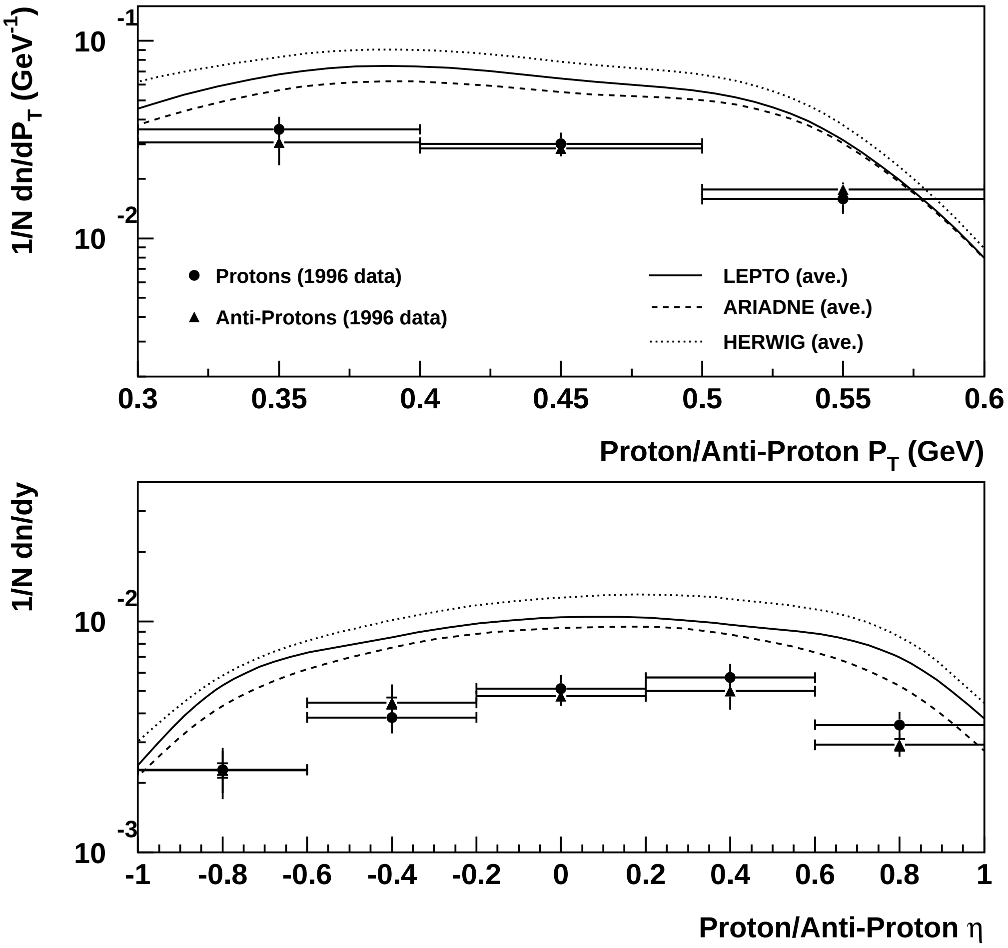

Figure 5.16: *Transverse momentum and pseudo-rapidity spectra for protons and antiprotons in kinematic bin 0 (from table 5.1). Shown are 1996 corrected data points together with Monte Carlo predictions of ARIADNE-D, LEPTO-D and HERWIG. Plotted in the H1 LAB frame.*

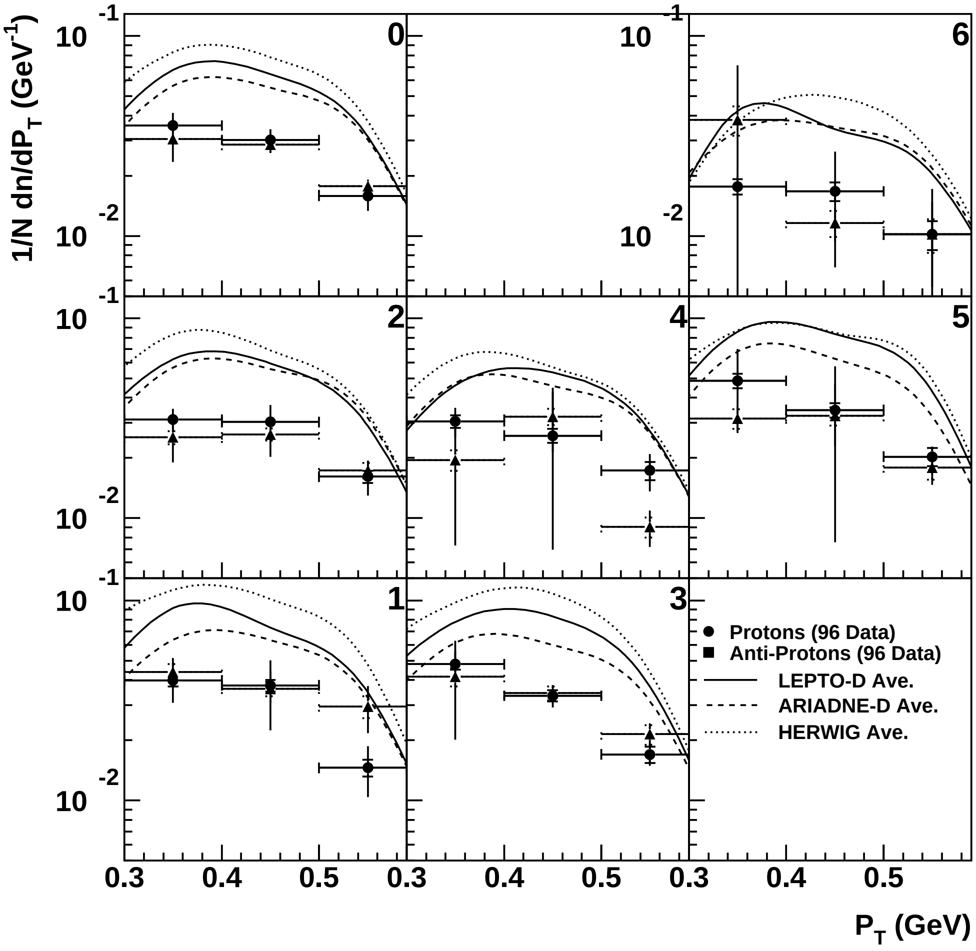

Figure 5.17: *Transverse momentum spectra for protons and antiprotons for all kinematic bins in table 5.1. Shown are 1996 corrected data points together with Monte Carlo predictions of ARIADNE-D, LEPTO-D and HERWIG. Plotted in the H1 LAB frame The numbering of the plots corresponds to the bin numbers of table 5.1, apart from bin 0, the plots are arranged with increasing x_{Bj} along the x-axis and increasing Q^2 up the y-axis..*

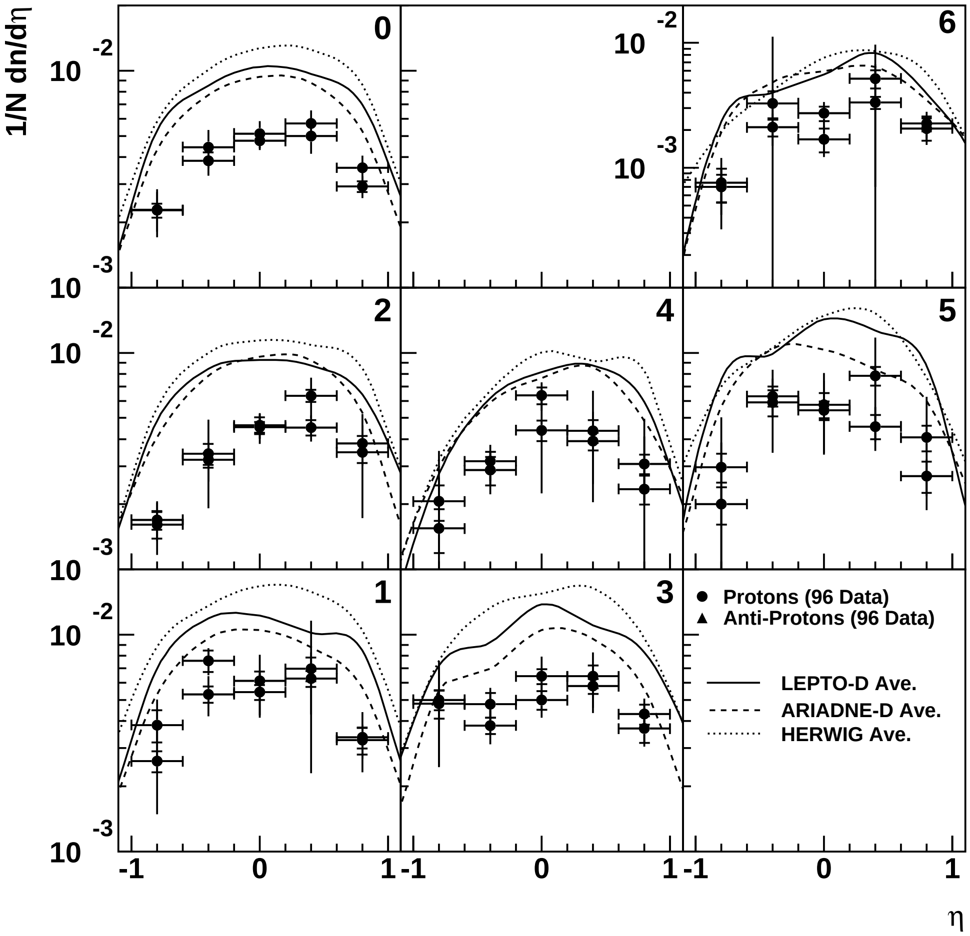

Figure 5.18: *Pseudo-rapidity spectra for protons and antiprotons for all kinematic bins in table 5.1. Shown are 1996 corrected data points together with Monte Carlo predictions of ARIADNE-D, LEPTO-D and HERWIG. Plotted in the H1 lab frame The numbering of the plots corresponds to the bin numbers of table 5.1, apart from bin 0, the plots are arranged with increasing* x_{Bj} *along the x-axis and increasing* Q^2 *up the y-axis..*

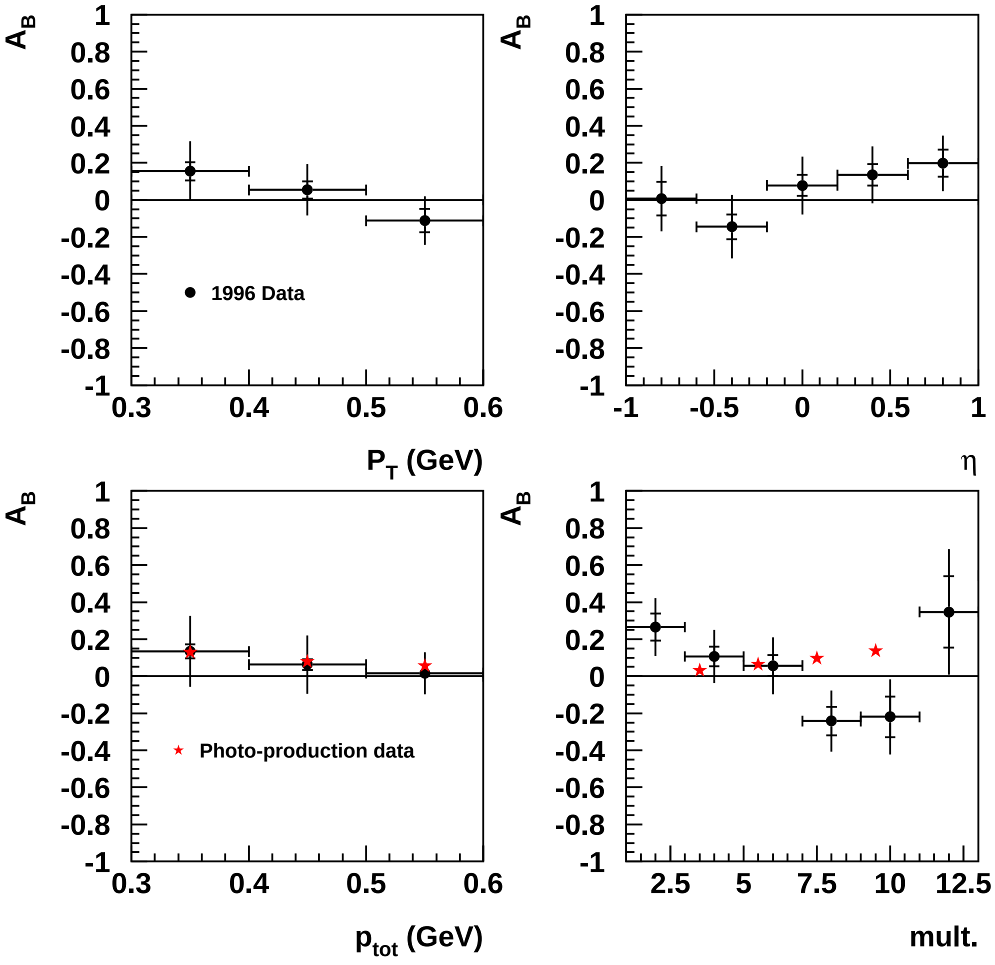

Figure 5.19: *Proton-antiproton asymmetry* $A_B = \frac{2.(N_p - N_{\bar{p}})}{N_p + N_{\bar{p}}}$ *as a function of transverse momentum, pseudo-rapidity, total momentum and charged track multiplicity. Plotted in the H1 LAB frame. Also shown are the results from the photo-production analysis of [28].*

Chapter 6

Search For QCD Instanton Induced Processes

QCD instanton processes can occur in the DIS scattering picture as shown in figure 1.14 and described in section 1.5.2. Here, a search strategy utilising the expected large strange particle yields in the instanton sub-process is used. The basis of the search is a set of events in the 1997 data pre-selected for their instanton-like characteristics. This pre-selection is due to the extensive Monte Carlo work performed [57] on event shape variables and other variables based on the expected hadronic final states of interactions involving the instanton sub-process.

6.1 Experimental Signatures and Event Pre-Selection

The investigation of possible instanton induced events is carried out based on the predicted topology of these events, and the predicted high multiplicity and flavour democracy of the partonic final state in such a sub-process.

In the $q'g$ (see figure 1.14) instanton CMS, there is an isotropic distribution of the partonic final state from the instanton sub-process. This leads to a hadronic final state restricted to a certain range in pseudo-rapidity η referred to as the 'instanton-band'. In the instanton CMS, this band is localised around $\eta = 0$. In the hadronic CMS, the centre of the band is shifted to higher values of η depending on the kinematics of the event. The size of this band is typically $\approx \pm 1.1$ units in η. In addition to this band, the hadronic final state will also exhibit a jet of particles originating from the outgoing current quark (q'' in figure 1.14).

In every instanton induced event, one quark and anti-quark of every kinematically accessible flavour is produced; as well as, on average, approximately 3 gluons. The multiplicity of the hadronic final state depends mainly on the accessible centre of mass energy W_i (see figure 1.14) and is typically $\mathcal{O}(20)$.

Figure 6.1 shows what a typical instanton event may look like. Clearly shown is the narrow band of particles in η, the high average transverse energy present and the isolated current jet.

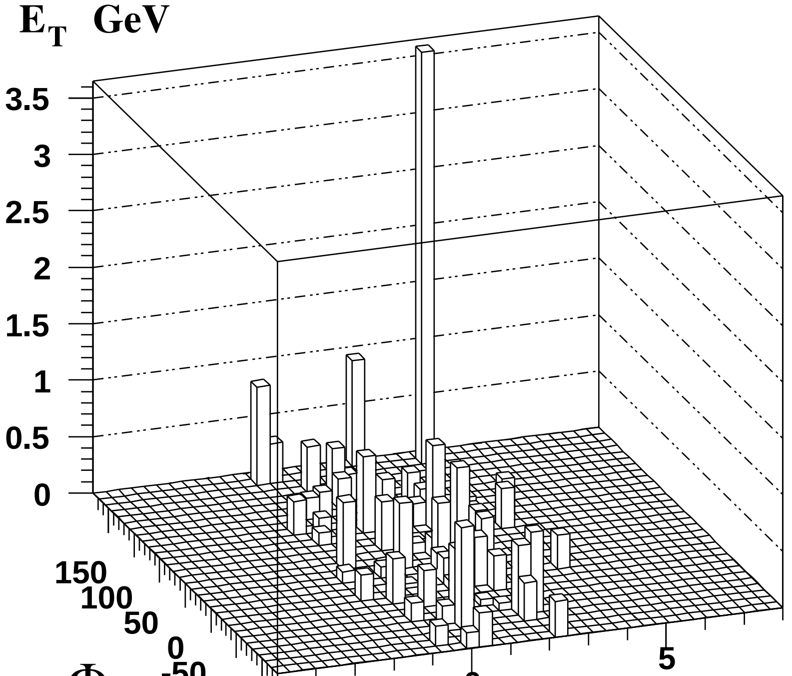

Figure 6.1: *A 'typical' instanton-induced DIS event in the $\eta - \phi$ plane, weighted for transverse energy. Taken from [58].*

Searches thus far for these events have used Monte Carlo models to isolate variables and cuts in these variables where the expected signal over standard DIS events is maximised [57]. No exploitation of the expected heavy flavour excess has been used as yet; apart from a study of K^o events based on the smaller 1994 event sample [56].

In this analysis, the kaon and pion selection process already established is used on the 1997 data sample with pre-selected events described below.

6.2 QCD Instanton Monte Carlo Model

To investigate the expected event shapes and distributions from the QCD instanton induced process in DIS, the QCDINS [59] Monte Carlo package was used. This acts as a hard process generator in the QCD Monte Carlo generator HERWIG (see section 5.4.1). The hard process is treated according to the physics assumptions outlined in 1.5.1. Default settings were used in the latest available QCDINS20 model, these include; $x' > 0.35$ and $n_f = 3$.

After the construction of the hard instanton sub-process, further gluons are simulated in the LLA. The coherent branching algorithm implemented in HERWIG is used. The hadronic final state is formed using the cluster fragmentation model (see section 1.2.5) also implemented in HERWIG.

6.3 Selection of an 'Instanton Enriched' Event Sample

Based on investigations using the QCDINS and standard DIS Monte Carlo programs, many variables were investigated [57]. The three variables deemed to give the best instanton-DIS background separation were those of; n_b (the hadronic multiplicity in the instanton band), sphericity (Sph) and Q'^2_{rec} (the reconstructed

value for Q'^2 as described in section 1.5.2) [58]. These variables are measured as follows:
Jets are defined using a cone algorithm, the jet with the highest transverse energy E_t is then used to estimate the four-momentum q'' of the current quark of figure 1.14. Q'^2_{rec} is then reconstructed from the particles associated with the current jet and the photon reconstructed from the scattered positron. Whilst this variable gives a good discrimination from DIS 'background', it is not sufficient to accurately model the true Q'^2 of the instanton sub-process.

The objects belonging to the current jet are removed from further consideration. The centre of the instanton band is defined by the E_t weighted pseudo-rapidity mean:

$$\bar{\eta} = \frac{\sum_n E_{t,h}\eta_h}{\sum_h E_{t,h}} \tag{6.1}$$

the instanton band is then defined by $\bar{\eta} \pm 1.1$ and the number of charged particles (n_b) in this band is counted.

The vectorial sum of all measured final state objects not associated with the current jet is used to perform a boost to their rest system defined by: $\sum_h \vec{p}_h = 0$. This is then an approximation to the instanton centre-of-mass system. It is in this frame that the sphericity is calculated.

The event normalised distributions of these three variables n_b, Sph and Q'^2_{rec} are shown in figure 6.2. Shown are the predictions based on QCDINS and two 'background' DIS models (ARIADNE and RAPGAP [54]). Based on these plots, a vast number of cuts were applied and combined [58]. Three cut scenarios were then chosen corresponding to cases with; a) highest instanton efficiency; b) high instanton efficiency at a reasonable separation power $\left(\frac{\epsilon_{ins}}{\epsilon_{DIS}}\right)$; c) highest separation power at greater than 10% instanton efficiency. These are presented in table 6.1.

Events selected using these three cut scenarios on 1997 data form the basis for the instanton search performed here. This pre-selection is analysed to find

Scenario	Cuts			ϵ_{ins}	$\frac{\epsilon_{ins}}{\epsilon_{DIS}}$	
	Q'^2 (GeV^2)	Sph	n_b		CDM	MEPS
A	95.0-200.0	0.40	5	32 %	35	34
B	105.0-200.0	0.40	7	21 %	56	52
C	105.0-200.0	0.50	8	11 %	86	71

Table 6.1: *Cut values, instanton efficiency and separation power in the three cut scenarios. Taken from [58].*

identified kaons and pions as described in chapters 4 and 5 for the 1996 data sample. The K/π ratio's are then compared for the 1997 sample before and after the 3 'instanton enhancing' scenarios described above, looking for a characteristic increase in the strangeness yield.

6.4 Instanton Search

6.4.1 Comparison of 1996 and 1997 data

The 1996 analysis for kaons and pions as described in chapters 4 and 5 was repeated for the 1997 data sample and corresponding Monte Carlo. From this analysis, the same physics plots shown in section 5.4.2 are produced. To provide a cross-check that the 1997 data is understood before applying the instanton enhancing cuts, these 1997 physics results are compared with the 1996 results displayed earlier. The p_T spectra for kaons, pions and the kaon/pion ratio for the two years are shown in figure 6.3. This is representative of all the plots investigated and shows agreement within calculated errors.

It is worth noting that the systematic errors calculated for the 1997 data set are overall, considerably worse than those from 1996. This is the reason for performing the primary analysis using the 1996 data set. The reasons for the differences arose due to greater CJC inefficiencies during the 1997 running period and worsening resolution. This lead to higher systematic errors in almost all the

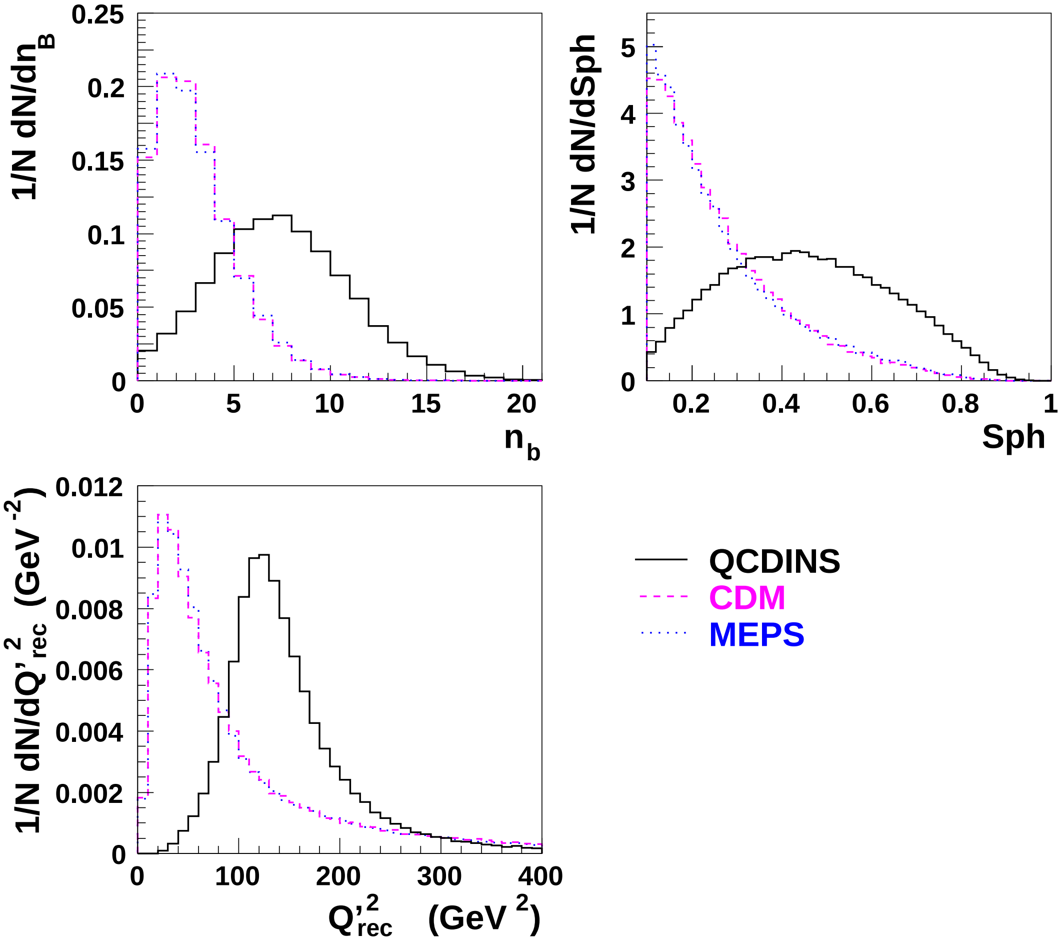

Figure 6.2: *Normalised distributions of the number of charged particles in the instanton band, the sphericity in the instanton rest system and the reconstructed* Q'^2*. Standard DIS and QCDINS Monte Carlo models are shown. Taken from [58].*

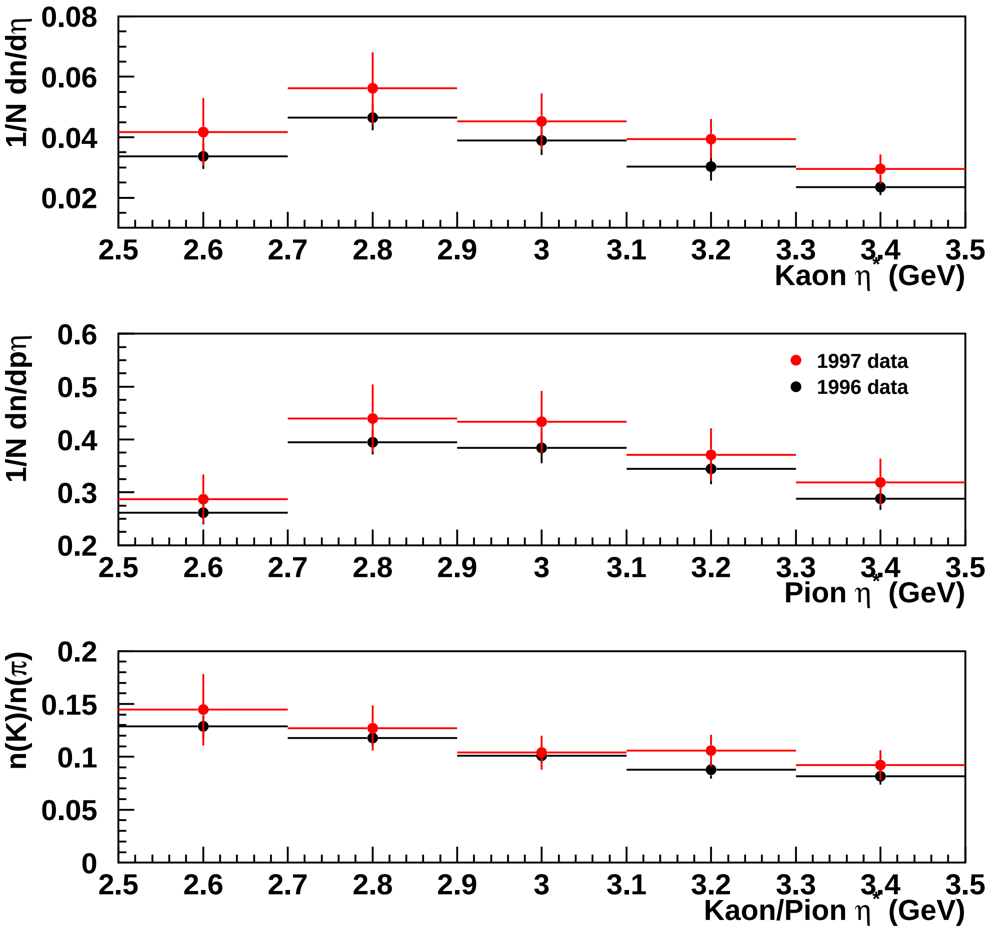

Figure 6.3: *Corrected pseudo-rapidity spectra for 1996 and 1997 DIS data.*

sources listed in table 5.2. Especially of note is the fact that the dE/dx resolution appears to be worse in 1997, with the dE/dx calibration apparently suffering as a result. As the more dominant sources of systematic error are at least partially correlated and not point-to-point, this has led to the systematic shifting of the kaon and pion spectra to higher values as seen in figure 6.3. The kaon/pion ratio seems to largely cancel out this effect. It is using this kaon/pion ratio that the search for these events is made.

6.4.2 Kaon/Pion Ratios with Instanton Enhanced Selections

The kaon and pion samples are taken as per the method described earlier, apart from the acceptance enhancing cuts in p_T^*, η^*, p^*. The kaon and pion yields are compared with reconstructed Monte Carlo models; of ARIADNE with the DELPHI tuned JETSET parameters shown in table 5.3. This is the Monte Carlo that best agreed with the prior data analysis. Also compared is the QCDINS Monte Carlo model discussed in section 6.2.

Shown at the end of this section in figures 6.4-6.6 are the event and track control plots of section 4.1 corresponding to the 1997 data and instanton selection A. These are representative of all instanton selections and compare 1997 data with the ARIADNE-D and QCDINS models. As can be seen, the data are once again modelled well in these plots with the ARIADNE-D DIS QCD Monte Carlo model, and less well with QCDINS. It is, however, from comparisons with the ARIADNE-D model that conclusions are largely drawn. Also shown in figures 6.7-6.11 are the dE/dx control plots as demonstrated with the 1996 sample earlier. Here, the plots are shown before cuts for reasons of statistics, although no bias is expected to be introduced in these through the cutting procedure. It is worth noting from figure 6.8 that although, as important here, the kaon and pion data seem well calibrated, the proton band appears to be poorly described in the 1997 data sample.

Results showing the ratio of observed kaons to pions before and after the addition of the cuts of scenarios A, B and C described in section 6.3 are presented in figures 6.12-6.26, together with the observed kaon and pion multiplicities after these cuts. The plots are not corrected for detector effects as before, instead comparisons are made between the data, corrected only for triggering inefficiencies (see section 4.2.2), and reconstructed Monte Carlo model (i.e. Monte Carlo that has been passed through the full H1 detector simulation).

In all plots, the inner error bars represent the 1σ statistical errors, and the outer error bars are the statistical and systematic errors added in quadrature. The sources of systematic error studied here are the same as those outlined in section 5.3, with the exception of those related to the detector correction procedure as this is not performed here owing to poor statistical precision following the cuts. The systematic uncertainties are calculated on the pre-instanton enhancing cut scenarios and assumed to be the same after the cuts have been applied.

Cut scenario A corresponds to a sample of 2932 1997 data events, 23220 QCDINS Monte Carlo events and 1976 ARIADNE-D Monte Carlo events. The plots in figure 6.12 show the average kaon/pion ratio for the data and ARIADNE-D Monte Carlo before the introduction of the cut A scenario; also shown is the data, ARIADNE-D and QCDINS Monte Carlo models after this selection has been made. Shown next to these two plots are the differences between the data and the standard DIS-based Monte Carlo ARIADNE-D. As can be seen, there is an increase of the strangeness production rate with respect to the standard DIS model after selecting events passing the scenario A cuts. This is not, however, predicted by the QCDINS model. Figures 6.13 and 6.14 show the above broken down into bins of p_T^* and η^* together with the differences in these plots between data and ARIADNE-D. It is hard given the large errors, due to the low statistics, to deduce any trend, although the differences seem larger towards higher p_T^* and higher η^*. Figure 6.15 shows the effect of the introduction of the cut A selection by giving the change in the differences between the data and DIS Monte Carlo model. As can be seen, there is an increase in strangeness yield by using these cuts, but not a significant one. Whilst figure 6.16 shows that there are no events with much larger than expected kaon yields as might be expected with an instanton induced event.

Cut scenario B corresponds to a sample of 1296 1997 data events, 15120 QCDINS Monte Carlo events and 764 ARIADNE-D Monte Carlo events. The plots in figures 6.17-6.21 correspond to the B cut selection and are of the same format as the plots described above for the A selection. Here, a larger and more significant excess of strangeness is observed than that seen with selection A, with the same approximate trends seen in p_T^* and η^*. The QCDINS Monte Carlo model predicts a higher strangeness rate than that of ARIADNE-D, but not as high as seen in the data. The overall increase in the strangeness seen in data over DIS Monte Carlo here is significant to the 1σ level but not to the 2σ level. Once again, figure 6.21 shows no anomalous multi-kaon events present.

Cut scenario C corresponds to a sample of 532 1997 data events, 8277 QCDINS Monte Carlo events and 257 ARIADNE-D Monte Carlo events. The above plots for this cut scenario are presented in figures 6.22-6.26. Here, there is a slighter greater increase in strangeness production again over scenario B with about the same significance and the same p_T^* and η^* trends. QCDINS also predicts this increased strangeness rate, but is less than that observed in the 1997 data. Again, figure 6.26 shows no anomalous multi-kaon events present here.

To summarize the results displayed here, table 6.2 shows the measured kaon/pion ratios after the three cut scenarios together with the effect these have on increasing the differences between the kaon/pion ratio in data and ARIADNE-D, the DIS Monte Carlo.

Cuts	Ave. K/π $\times 10^{-2}$			(Data-ARIADNE) diff.
	1997 Data	ARIADNE-D	QCDINS17	$\times 10^{-2}$
A	$4.87 \pm 0.42 \pm 0.60$	3.73 ± 0.45	3.58 ± 0.09	$0.64 \pm 0.62 \pm 0.87$
B	$4.60 \pm 0.57 \pm 0.72$	2.75 ± 0.58	3.54 ± 0.11	$1.6 \pm 0.82 \pm 1.0$
C	$3.84 \pm 0.77 \pm 0.88$	1.75 ± 0.73	3.31 ± 0.14	$1.9 \pm 1.1 \pm 1.2$

Table 6.2: *Measured kaon/pion ratios after the 3 cut scenarios listed in table 6.1. Shown are the average kaon/pion rates and the increase in difference of this value between 1997 data and ARIADNE-D after the cuts have been implemented. The errors for data shown are statistical only (first error) and the sum in quadrature of the statistical and systematic errors (second error).*

These results show that there is an observed increase in strangeness production rate, and that this is highest in scenario C where the instanton enhancement is

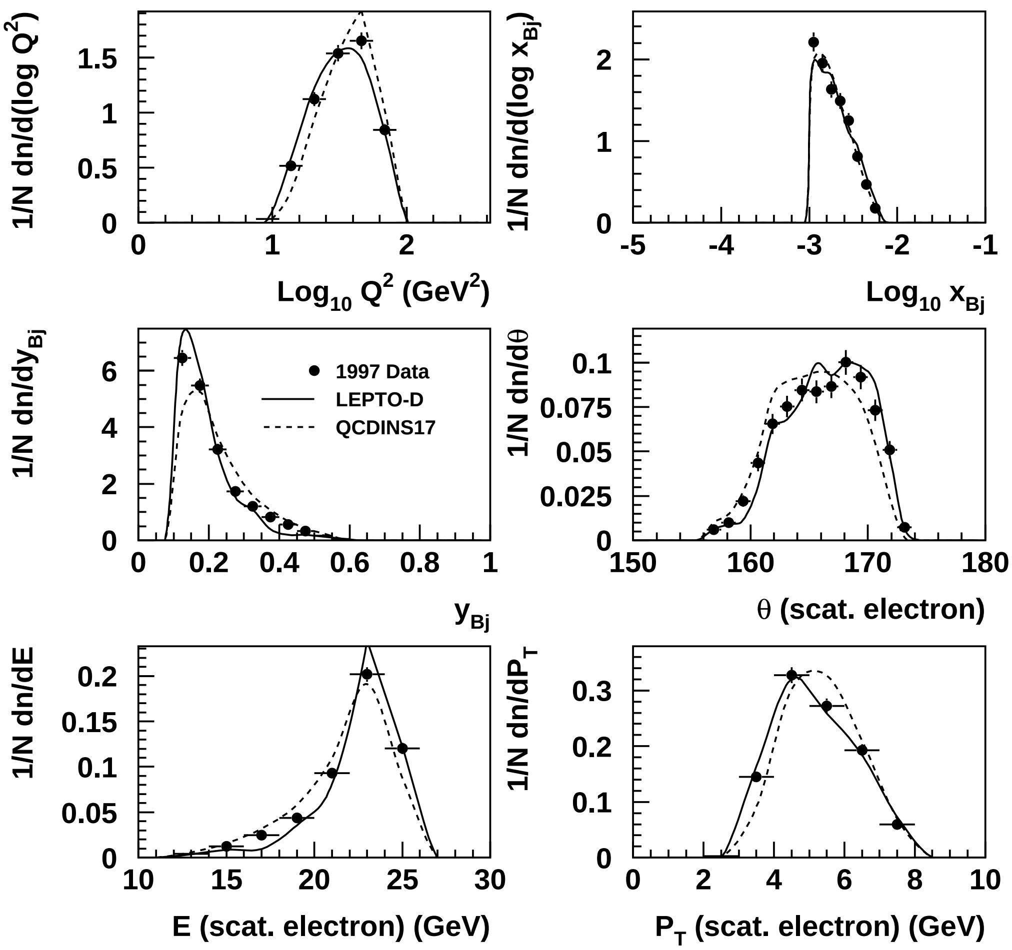

Figure 6.4: *Kinematic variables of the scattered positron for the 1997 data sample and ARIADNE-D and QCDINS17 Monte Carlo Models.*

expected to be largest. Although, as none of these increases is significant at the 2σ level, no strong message can be put forward here. Also, unfortunately, in the phase space region considered here, it can be seen that the QCDINS model does not predict a kaon/pion ratio any higher than that observed, and not much above the ARIADNE-D prediction. This means that it is futile to place an upper limit on the instanton cross-section from these results as it will be vastly above predicted values and lower estimates placed by other experiments (see for example [56], [58]).

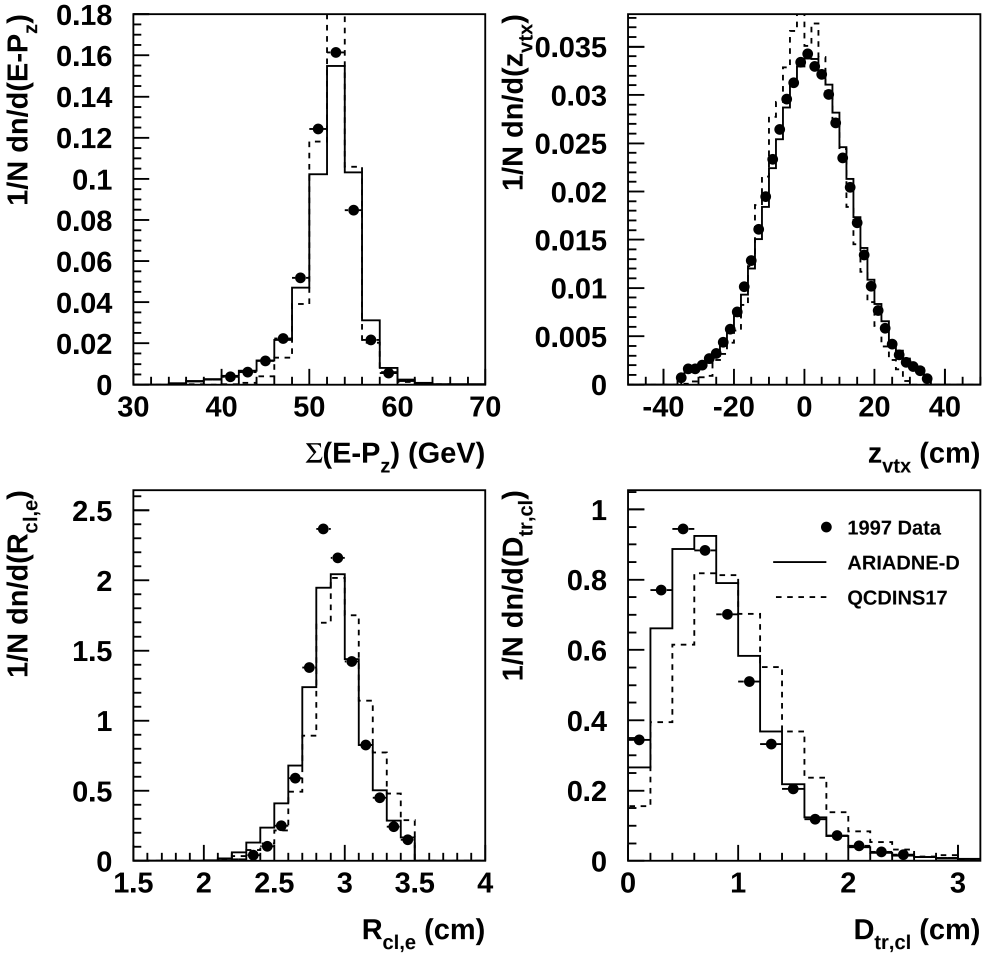

Figure 6.5: *Event selection control plots for 1997 data, ARIADNE-D and QCDINS17 Monte Carlo. See section 4.2.1 for details of variables.*

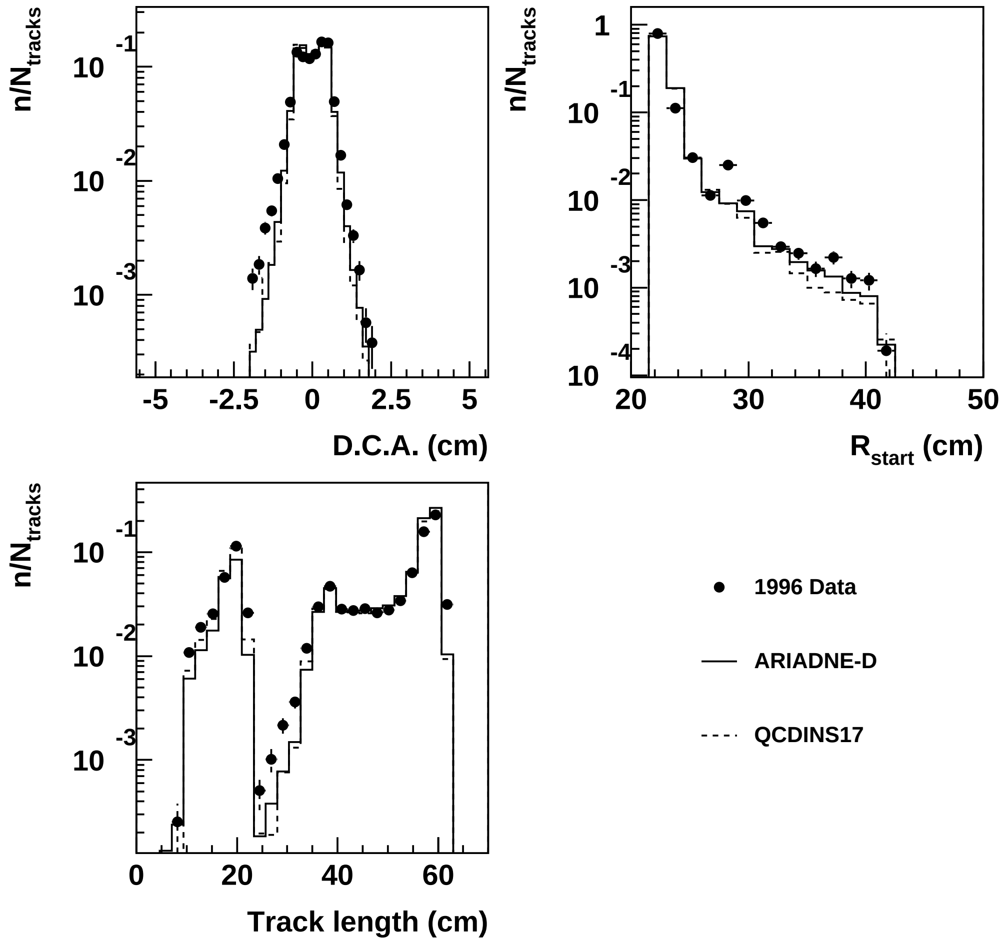

Figure 6.6: *Tracking control plots for 1997 data, ARIADNE-D and QCDINS17 Monte Carlo. Shown are distance of closest approach, radius of track start point and track length within the CJC.*

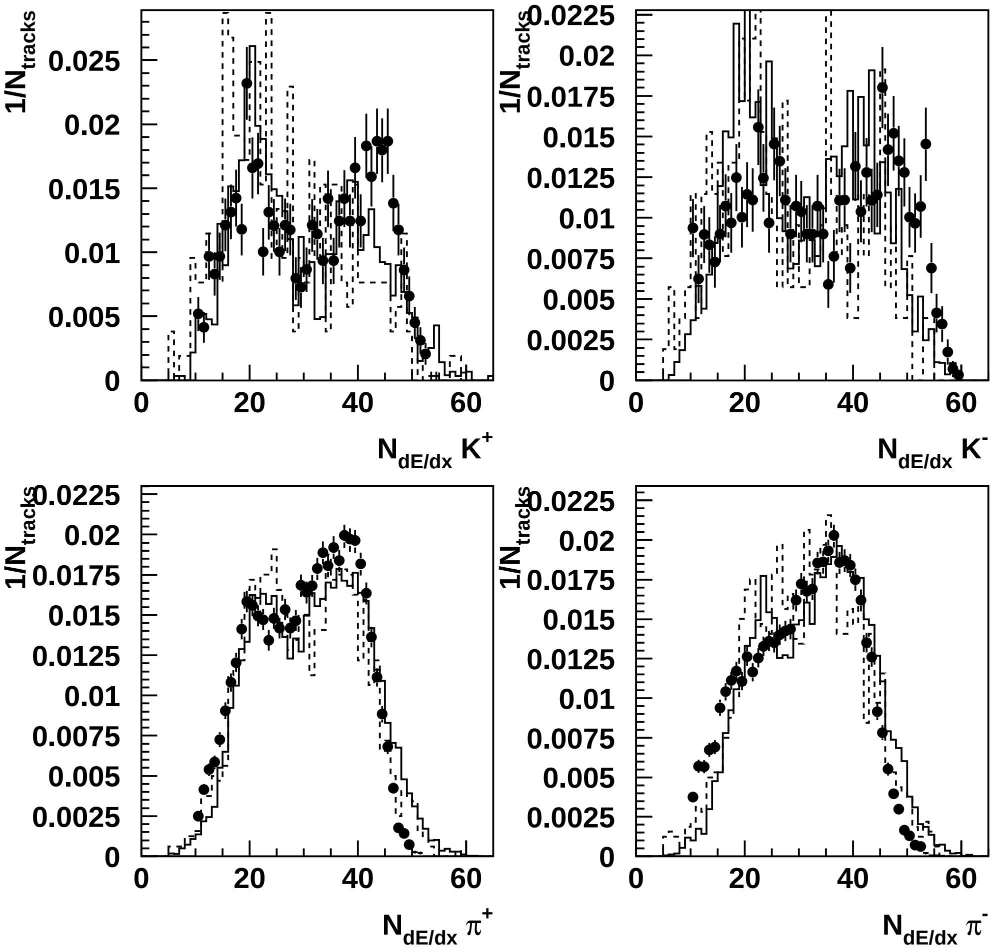

Figure 6.7: *Number of hits in CJC used for track reconstruction. Shown are 1997 data points together with reconstructed ARIADNE and QCDINS Monte Carlo models.*

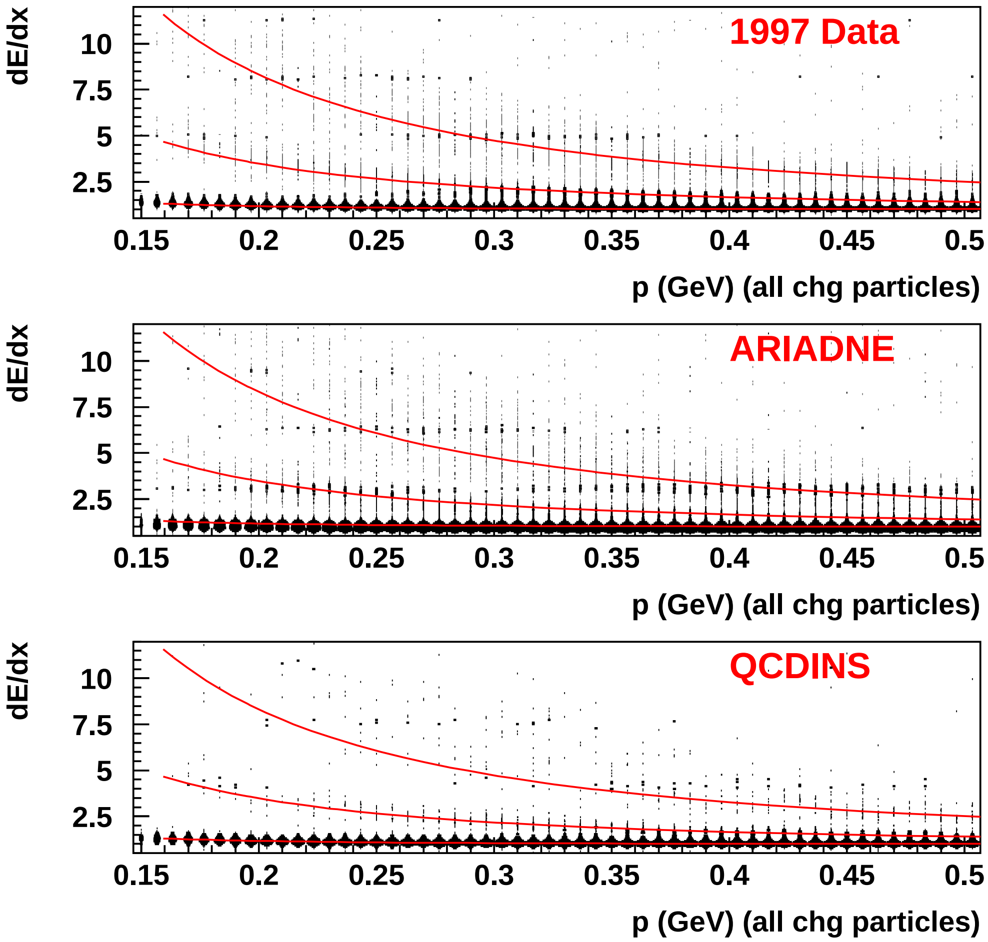

Figure 6.8: *Momentum vs. dE/dx together with superimposed Bethe-Bloch-like 'norm' functions (see 3.3). Shown are 1997 data points, reconstructed ARIADNE and QCDINS Monte Carlo models.*

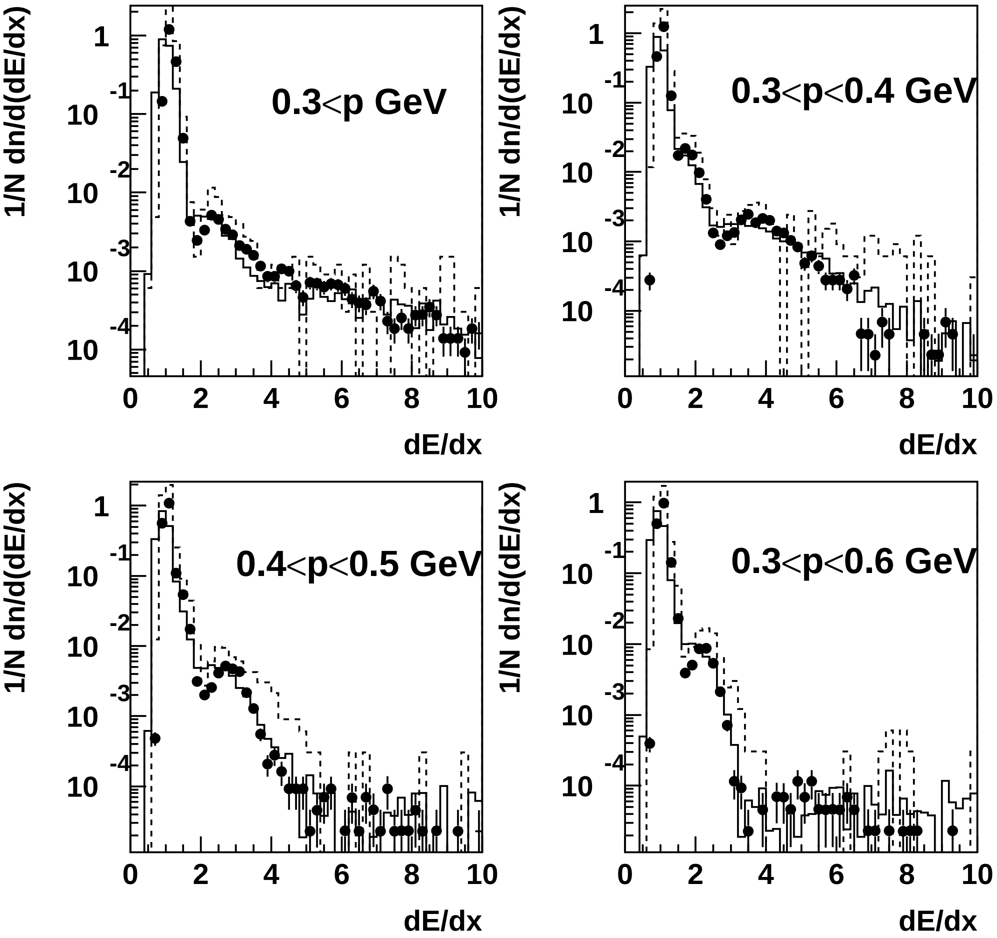

Figure 6.9: *dE/dx distributions for 1997 data, ARIADNE and QCDINS Monte Carlo Models, shown in four bins of momentum.*

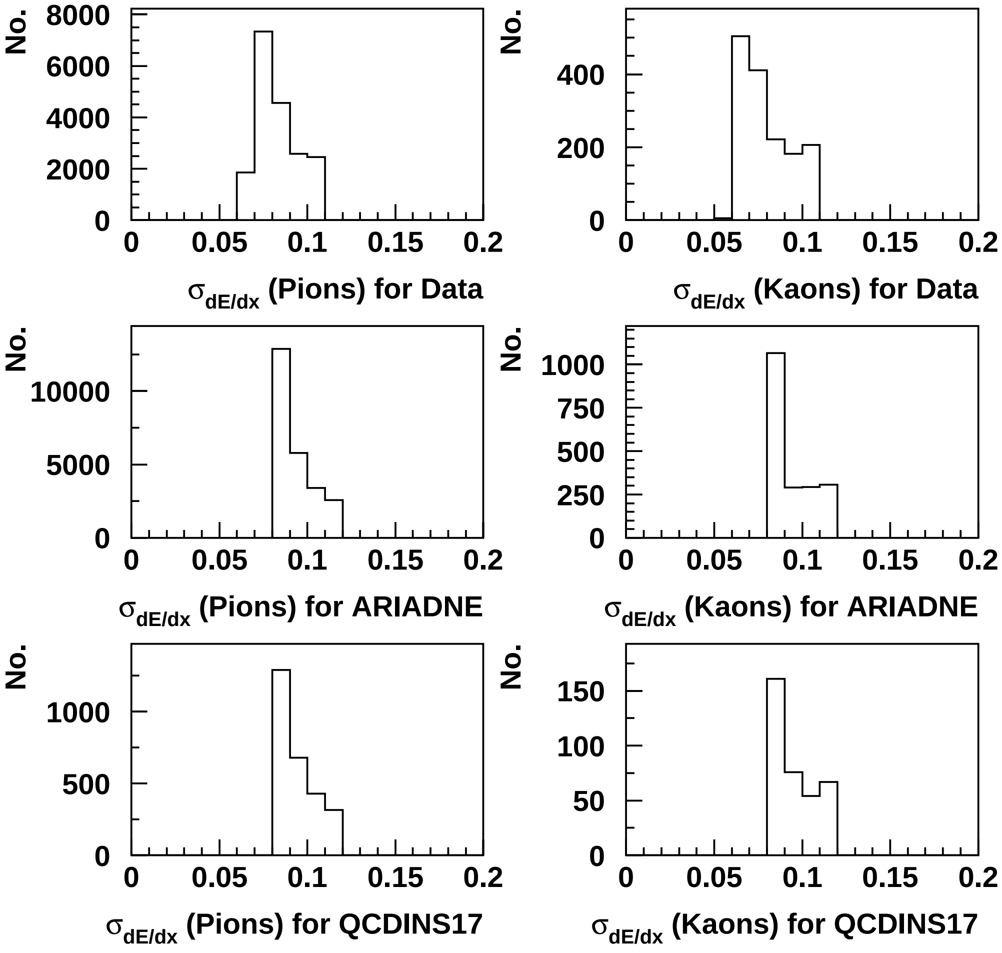

Figure 6.10: *Resolution of dE/dx measurements in 1997 data, ARIADNE and QCDINS Monte Carlo models.*

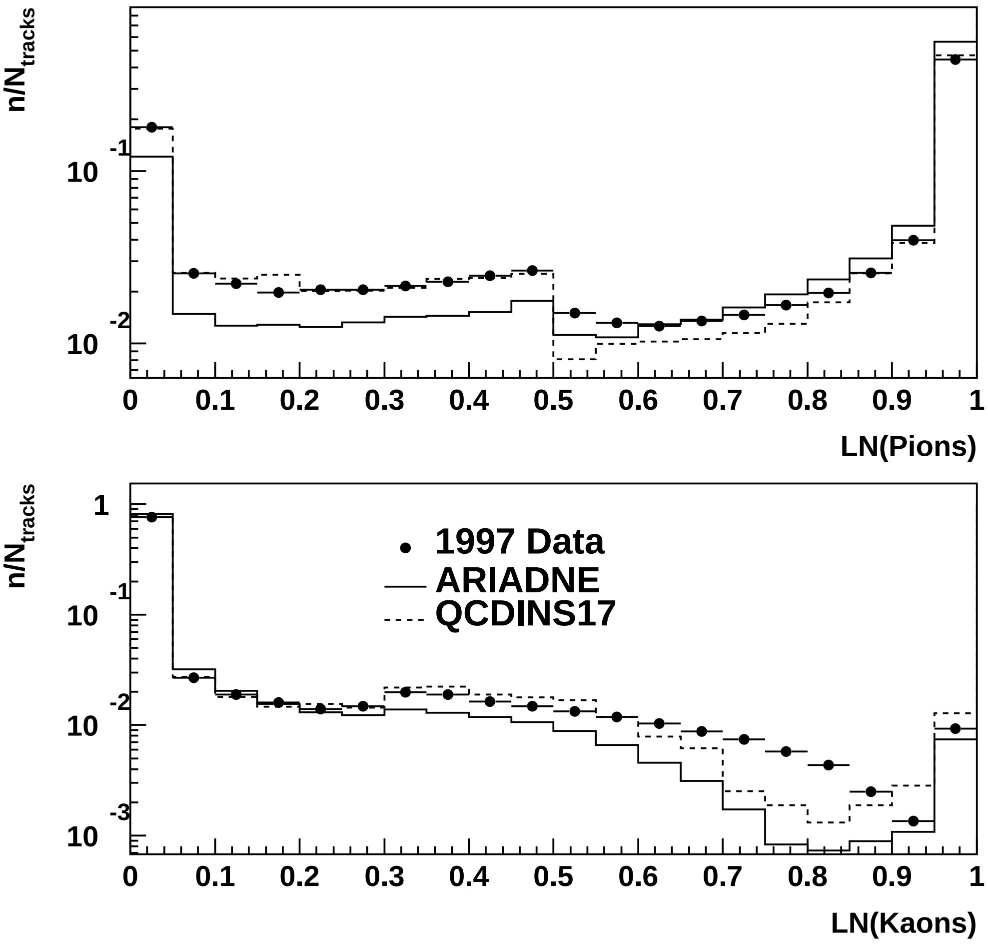

Figure 6.11: *Distributions of measured normalised log-likelihoods in 1997 data, ARIADNE and QCDINS Monte Carlo models (see Chapter 2).*

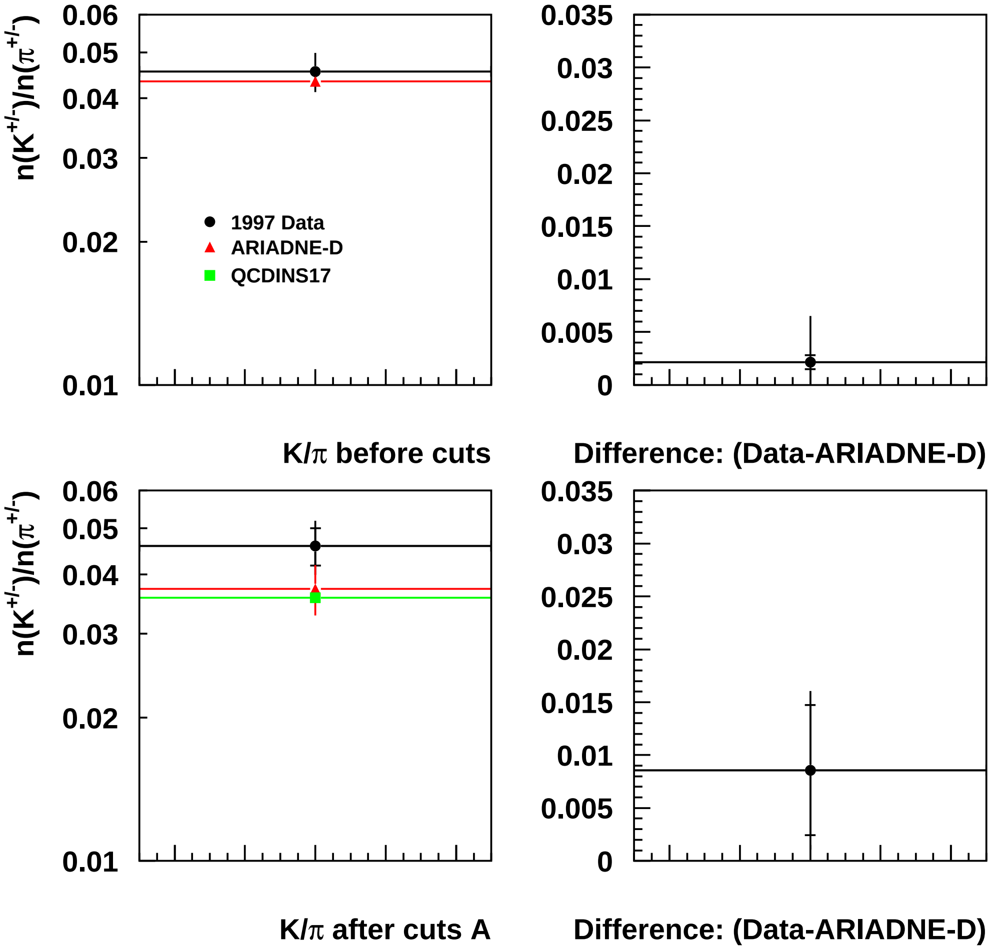

Figure 6.12: *Average Kaon/Pion rate before and after instanton enhancing cuts set A. Shown are the average rates for 1996 data and reconstructed ARIADNE-D Monte Carlo before and after the cuts and QCDINS17 Monte Carlo for the cut scenario A. Also shown are the differences between the data and ARIADNE-D Monte Carlo plots. The data have been corrected only for triggering inefficiencies.*

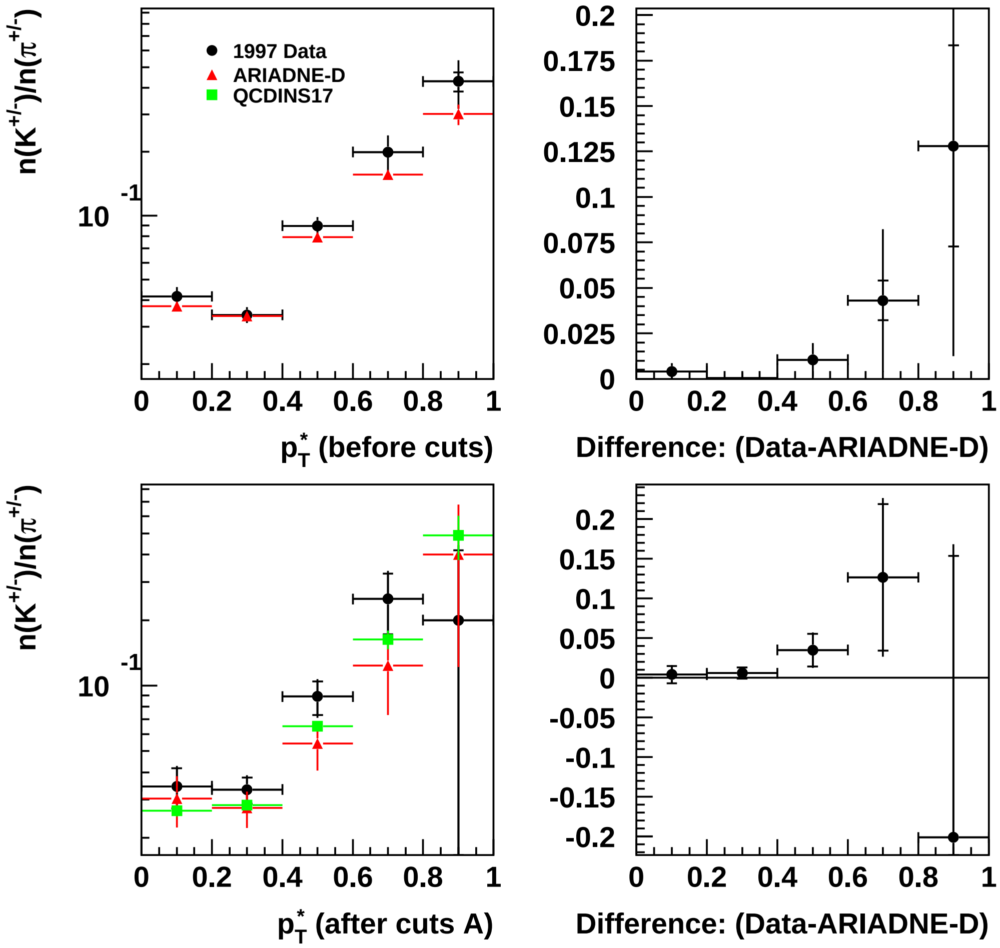

Figure 6.13: *Kaon/Pion ratio as a function of transverse momentum before and after instanton enhancing cuts set A. Shown are the average rates for 1996 data and reconstructed ARIADNE-D Monte Carlo before and after the cuts and QCDINS17 Monte Carlo for the cut scenario A. Also shown are the differences between the data and ARIADNE-D Monte Carlo plots. Plots are presented in the H1 CMS frame, the data have been corrected only for triggering inefficiencies.*

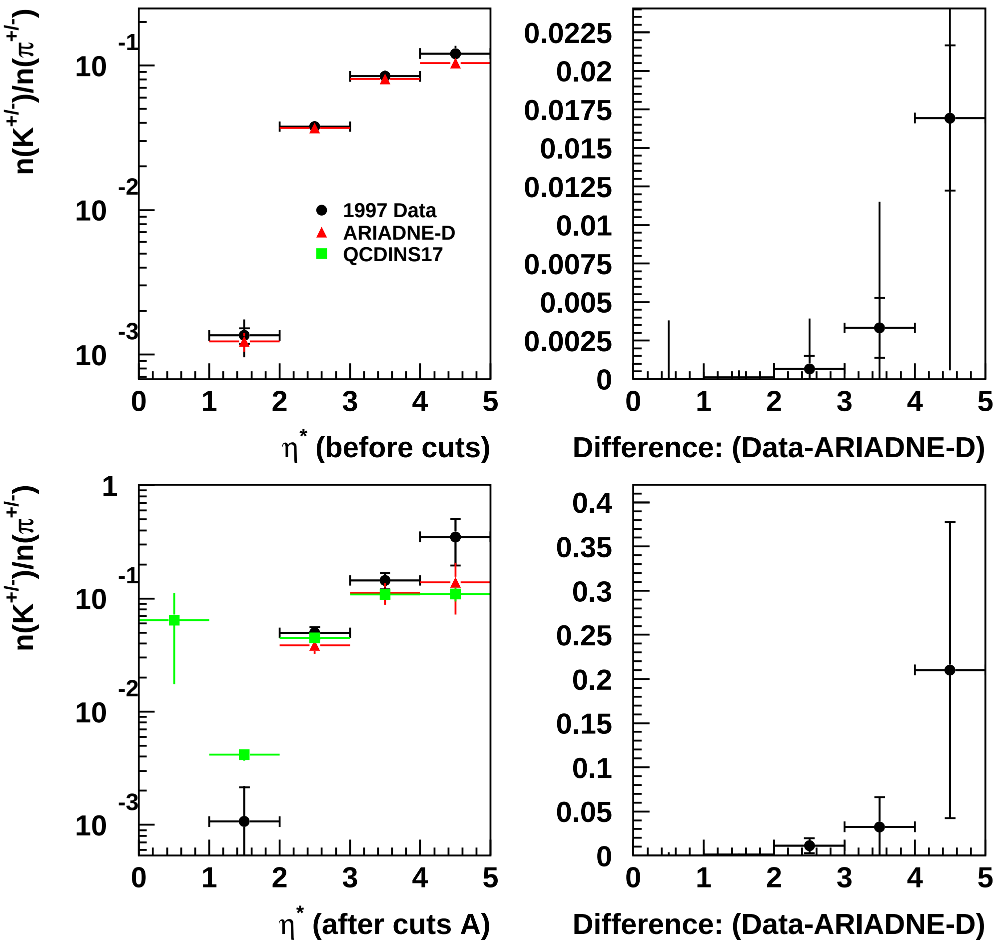

Figure 6.14: *Kaon/Pion ratio as a function of pseudo-rapidity before and after instanton enhancing cuts set A. Shown are the average rates for 1996 data and reconstructed ARIADNE-D Monte Carlo before and after the cuts and QCDINS17 Monte Carlo for the cut scenario A. Also shown are the differences between the data and ARIADNE-D Monte Carlo plots. Plots are presented in the H1 CMS frame, the data have been corrected only for triggering inefficiencies.*

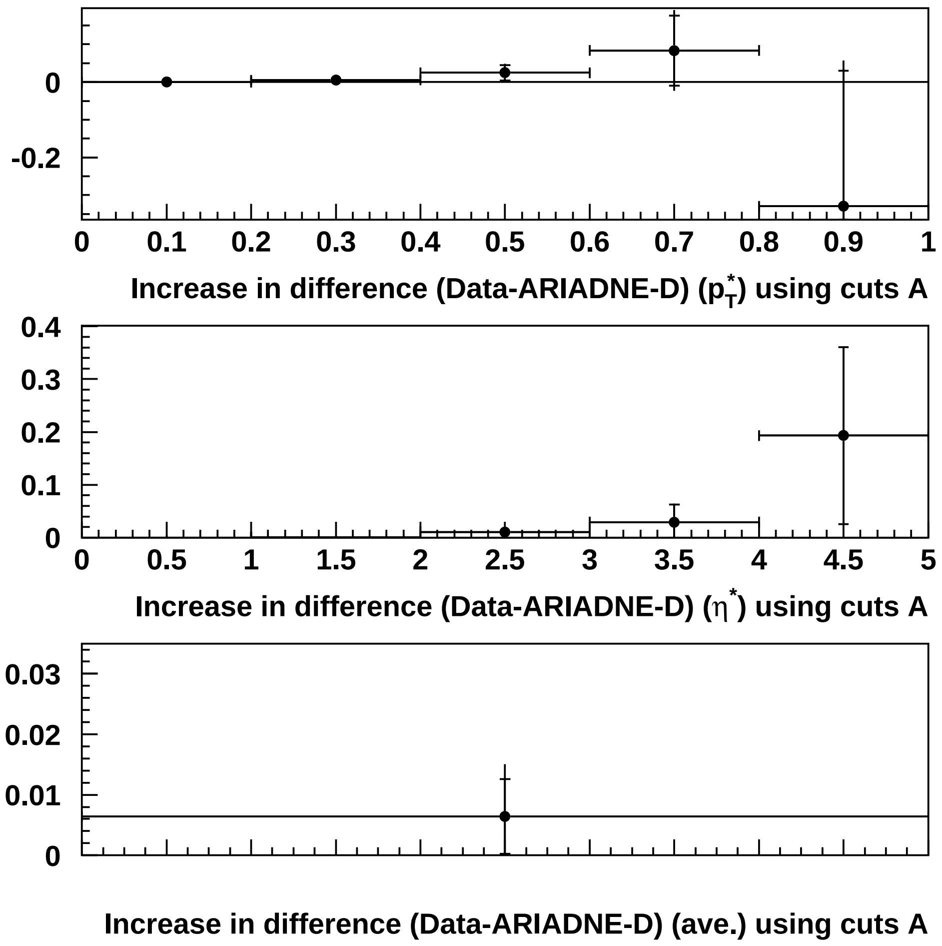

Figure 6.15: *The change in differences between data and ARIADNE-D with the addition of cut scenario A shown for all the quantities in the previous 3 figures.*

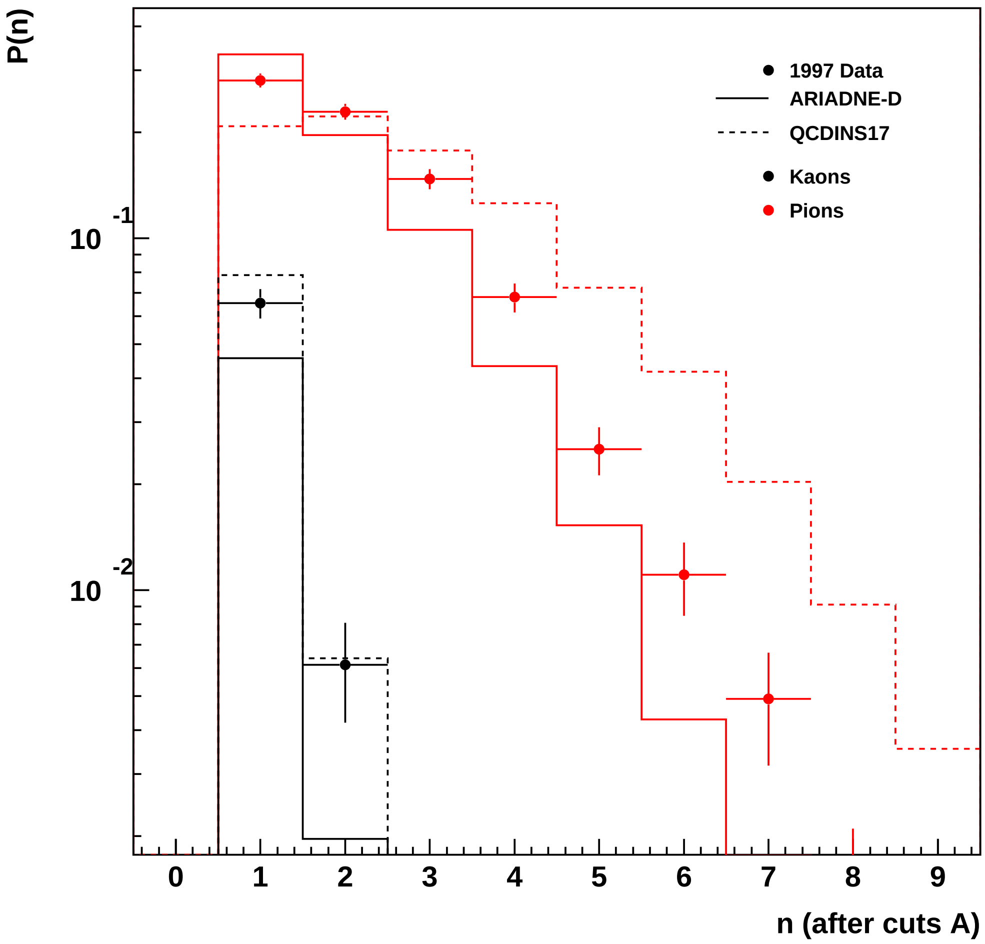

Figure 6.16: *Kaon and pion multiplicity after cut scenario A. 1996 data, ARIADNE-D and QCDINS17 Monte Carlo models shown.*

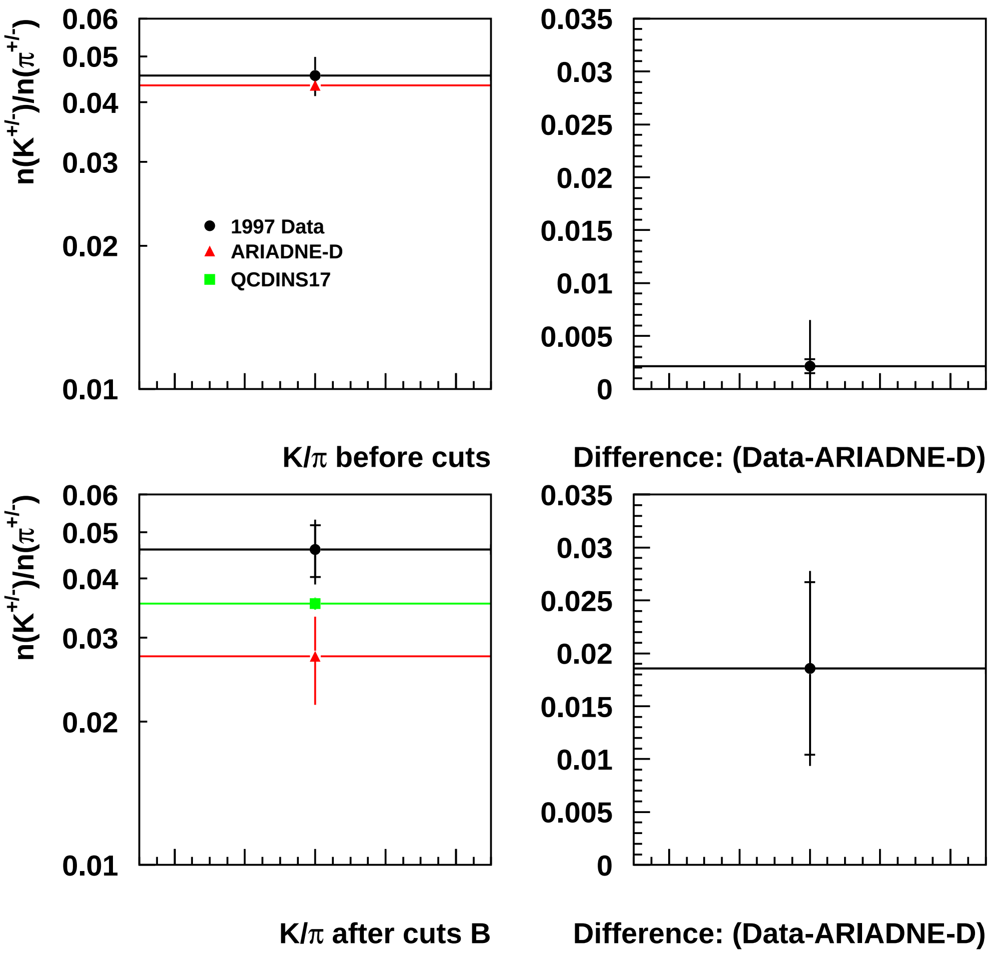

Figure 6.17: *Average Kaon/Pion rate before and after instanton enhancing cuts set B. Shown are the average rates for 1996 data and reconstructed ARIADNE-D Monte Carlo before and after the cuts and QCDINS17 Monte Carlo for the cut scenario B. Also shown are the differences between the data and ARIADNE-D Monte Carlo plots. The data have been corrected only for triggering inefficiencies.*

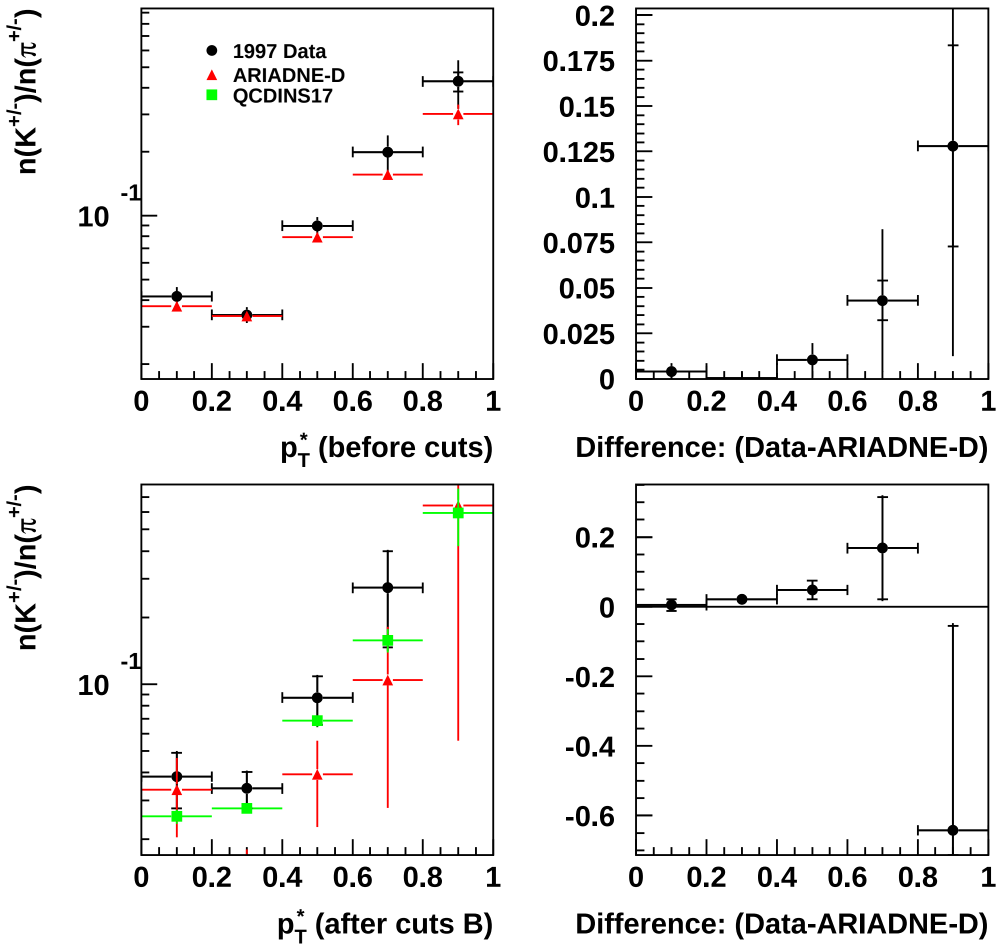

Figure 6.18: *Kaon/Pion ratio as a function of transverse momentum before and after instanton enhancing cuts set B. Shown are the average rates for 1996 data and reconstructed ARIADNE-D Monte Carlo before and after the cuts and QCDINS17 Monte Carlo for the cut scenario B. Also shown are the differences between the data and ARIADNE-D Monte Carlo plots. Plots are presented in the H1 CMS frame, the data have been corrected only for triggering inefficiencies.*

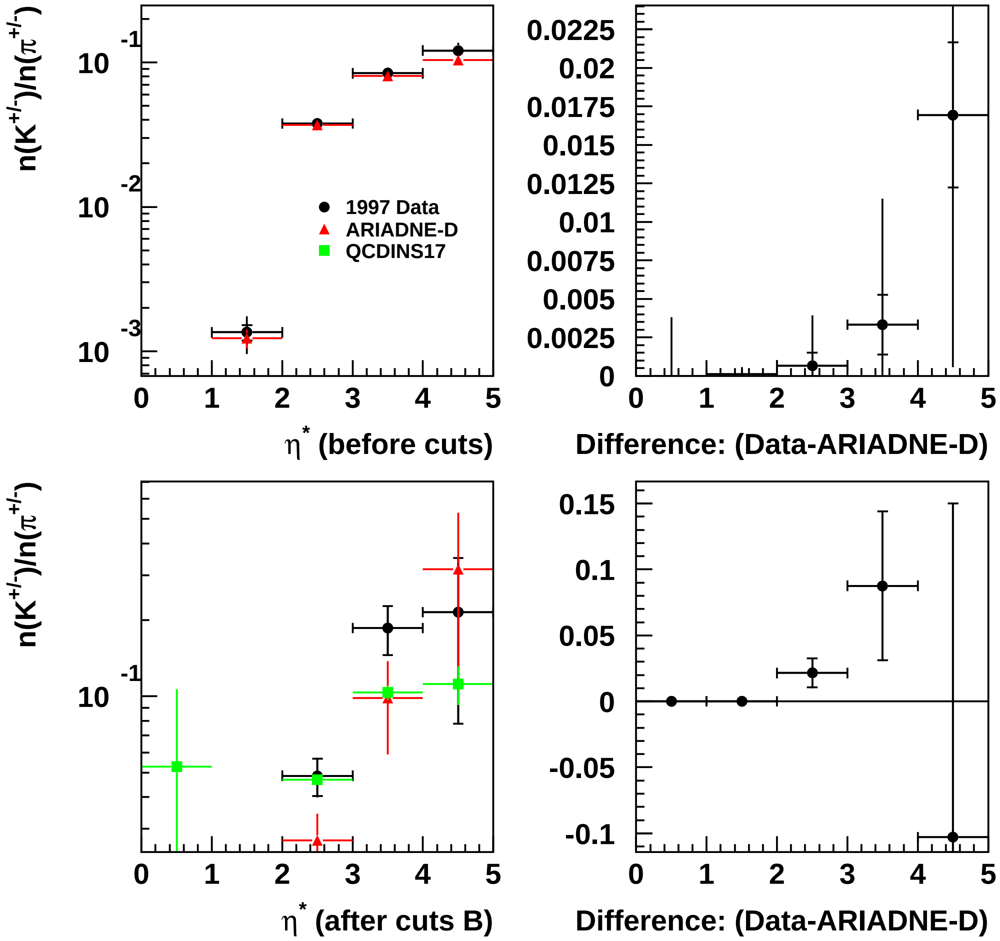

Figure 6.19: *Kaon/Pion ratio as a function of pseudo-rapidity before and after instanton enhancing cuts set B. Shown are the average rates for 1996 data and reconstructed ARIADNE-D Monte Carlo before and after the cuts and QCDINS17 Monte Carlo for the cut scenario B. Also shown are the differences between the data and ARIADNE-D Monte Carlo plots. Plots are presented in the H1 CMS frame, the data have been corrected only for triggering inefficiencies.*

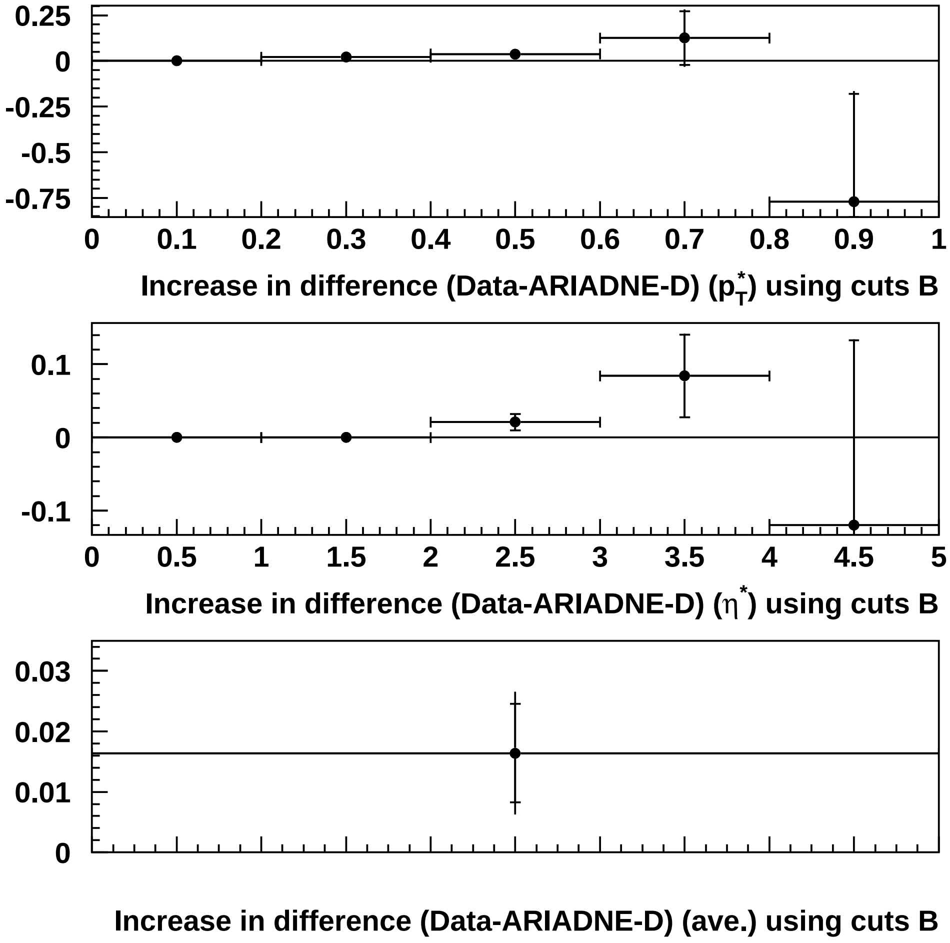

Figure 6.20: *The change in differences between data and ARIADNE-D with the addition of cut scenario B shown for all the quantities in the previous 3 figures.*

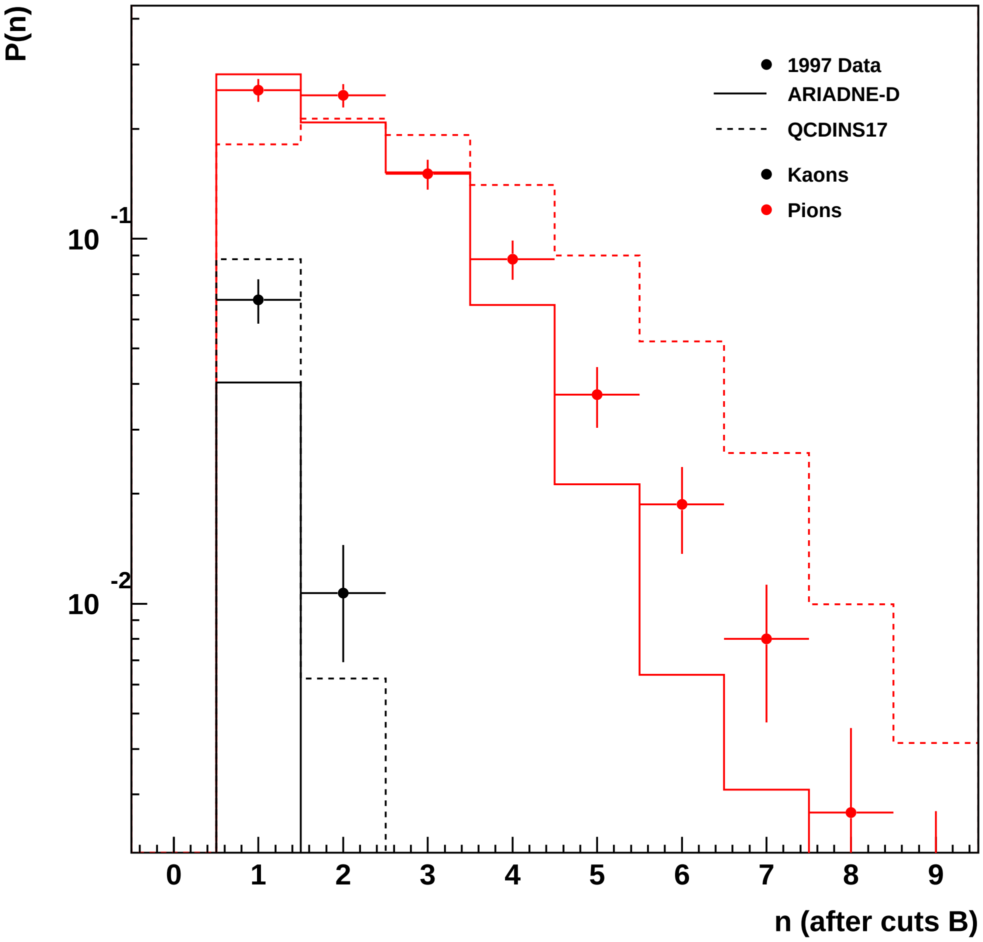

Figure 6.21: *Kaon and pion multiplicity after cut scenario B. 1996 data, ARIADNE-D and QCDINS17 Monte Carlo models shown.*

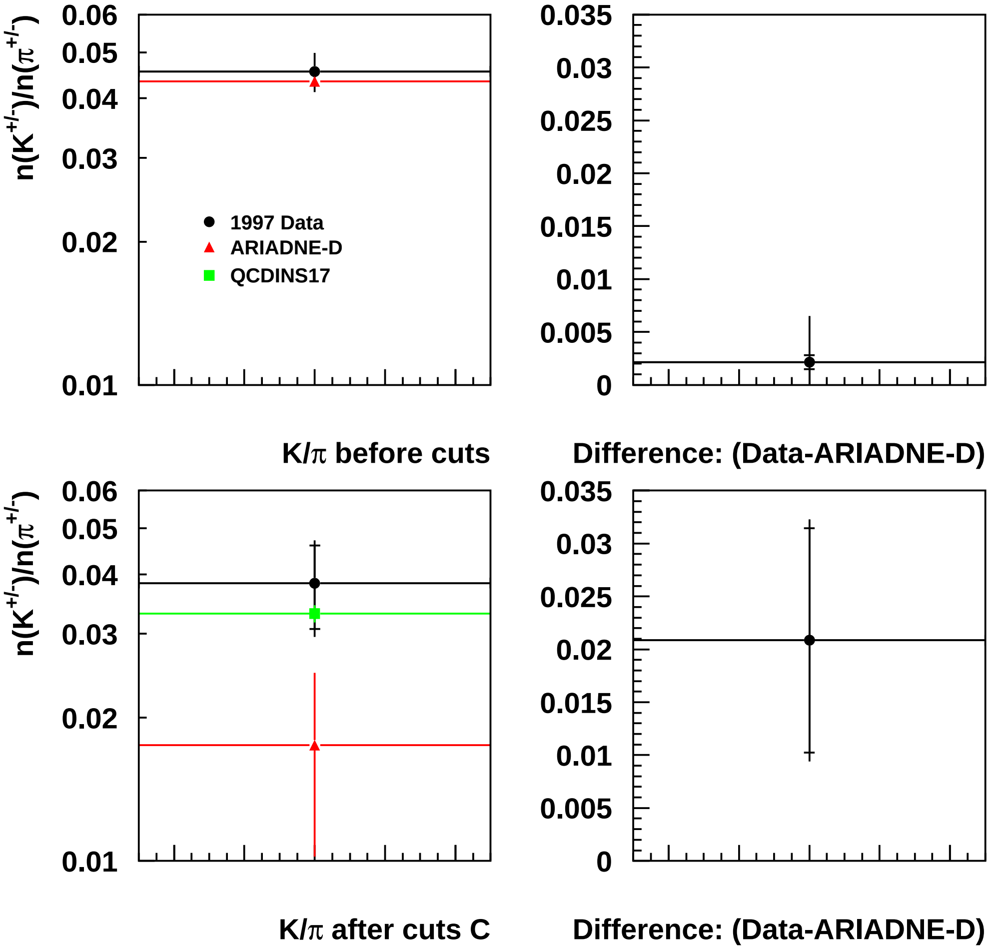

Figure 6.22: *Average Kaon/Pion rate before and after instanton enhancing cuts set C. Shown are the average rates for 1996 data and reconstructed ARIADNE-D Monte Carlo before and after the cuts and QCDINS17 Monte Carlo for the cut scenario C. Also shown are the differences between the data and ARIADNE-D Monte Carlo plots. The data have been corrected only for triggering inefficiencies.*

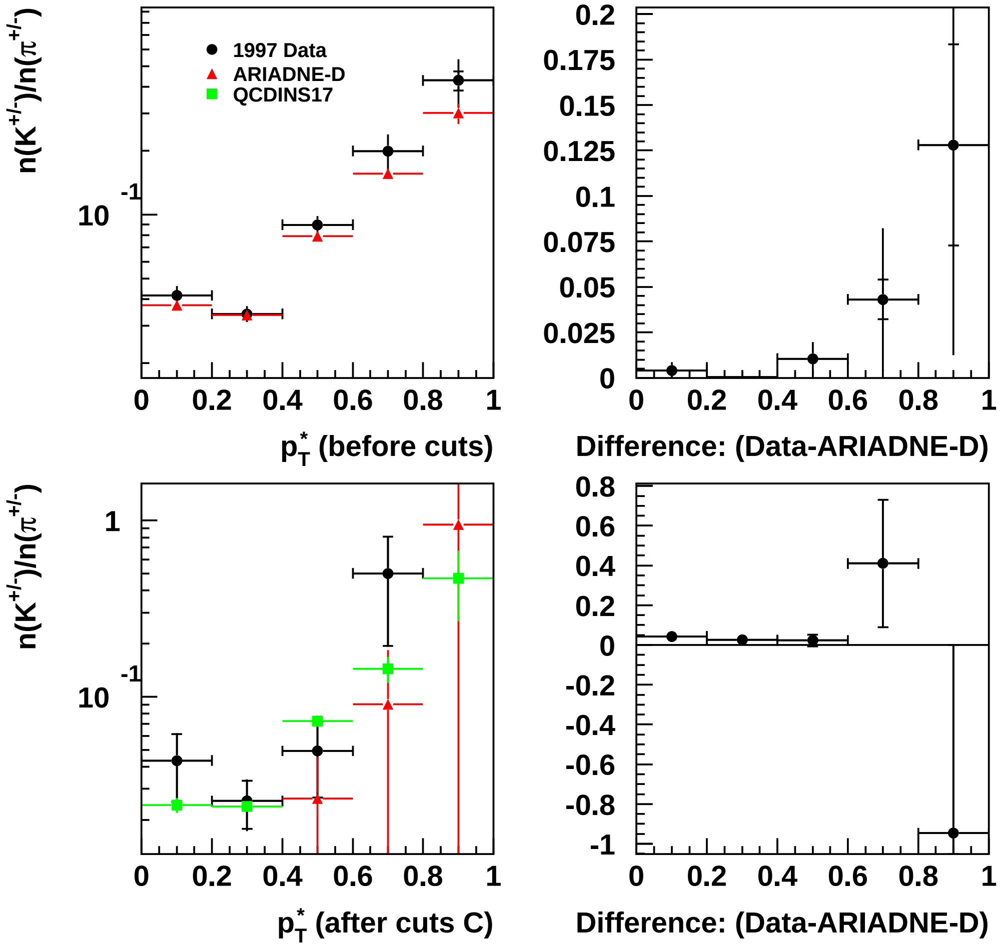

Figure 6.23: *Kaon/Pion ratio as a function of transverse momentum before and after instanton enhancing cuts set C. Shown are the average rates for 1996 data and reconstructed ARIADNE-D Monte Carlo before and after the cuts and QCDINS17 Monte Carlo for the cut scenario C. Also shown are the differences between the data and ARIADNE-D Monte Carlo plots. Plots are presented in the H1 CMS frame, the data have been corrected only for triggering inefficiencies.*

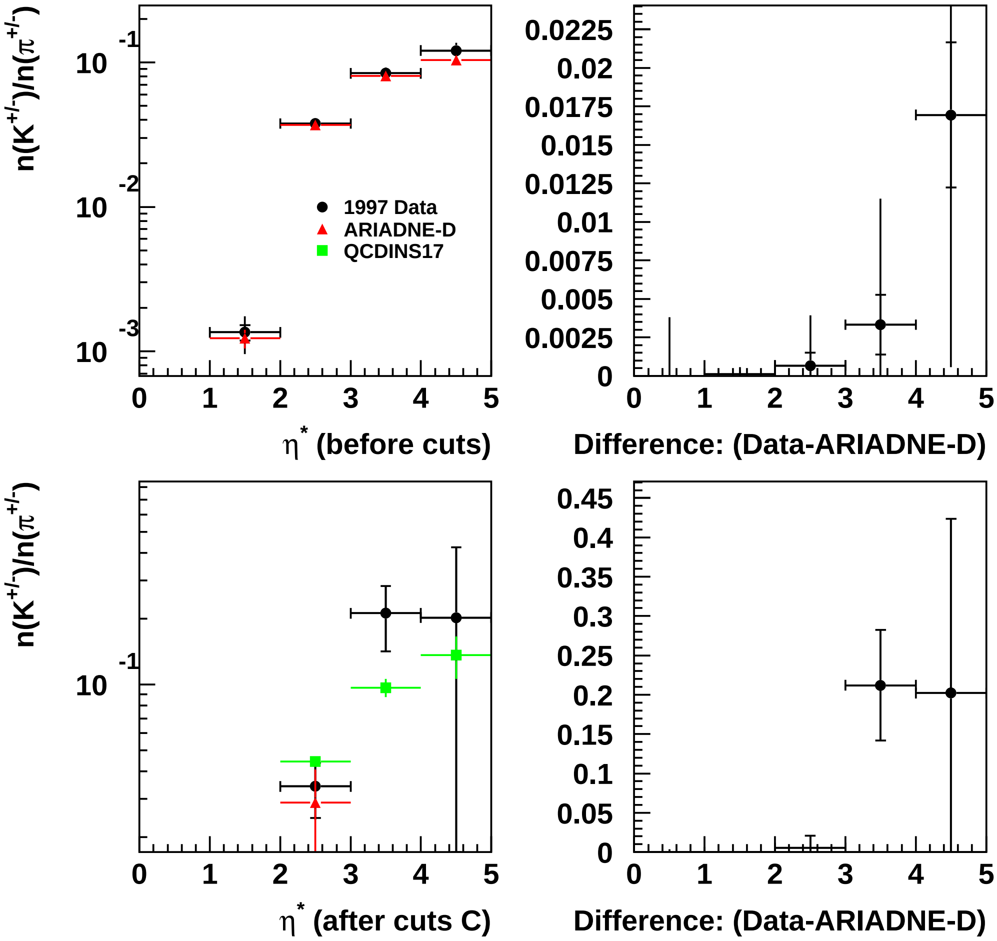

Figure 6.24: *Kaon/Pion ratio as a function of pseudo-rapidity before and after instanton enhancing cuts set C. Shown are the average rates for 1996 data and reconstructed ARIADNE-D Monte Carlo before and after the cuts and QCDINS17 Monte Carlo for the cut scenario C. Also shown are the differences between the data and ARIADNE-D Monte Carlo plots. Plots are presented in the H1 CMS frame, the data have been corrected only for triggering inefficiencies.*

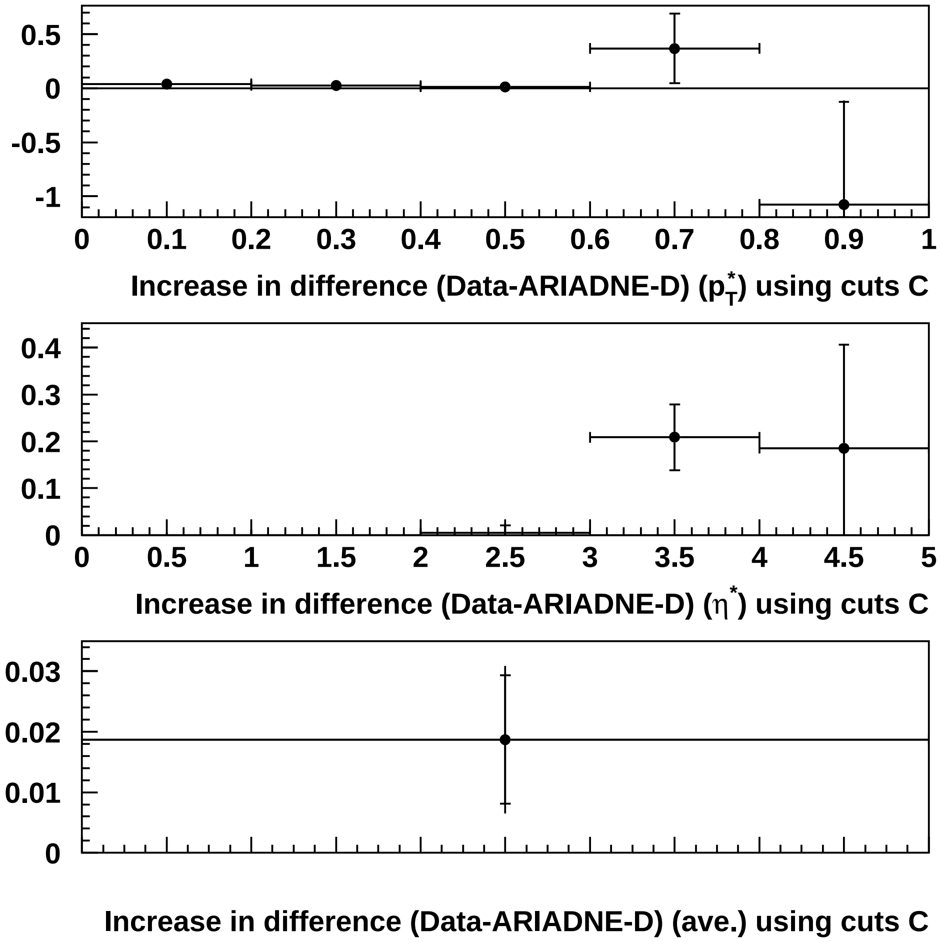

Figure 6.25: *The change in differences between data and ARIADNE-D with the addition of cut scenario C shown for all the quantities in the previous 3 figures.*

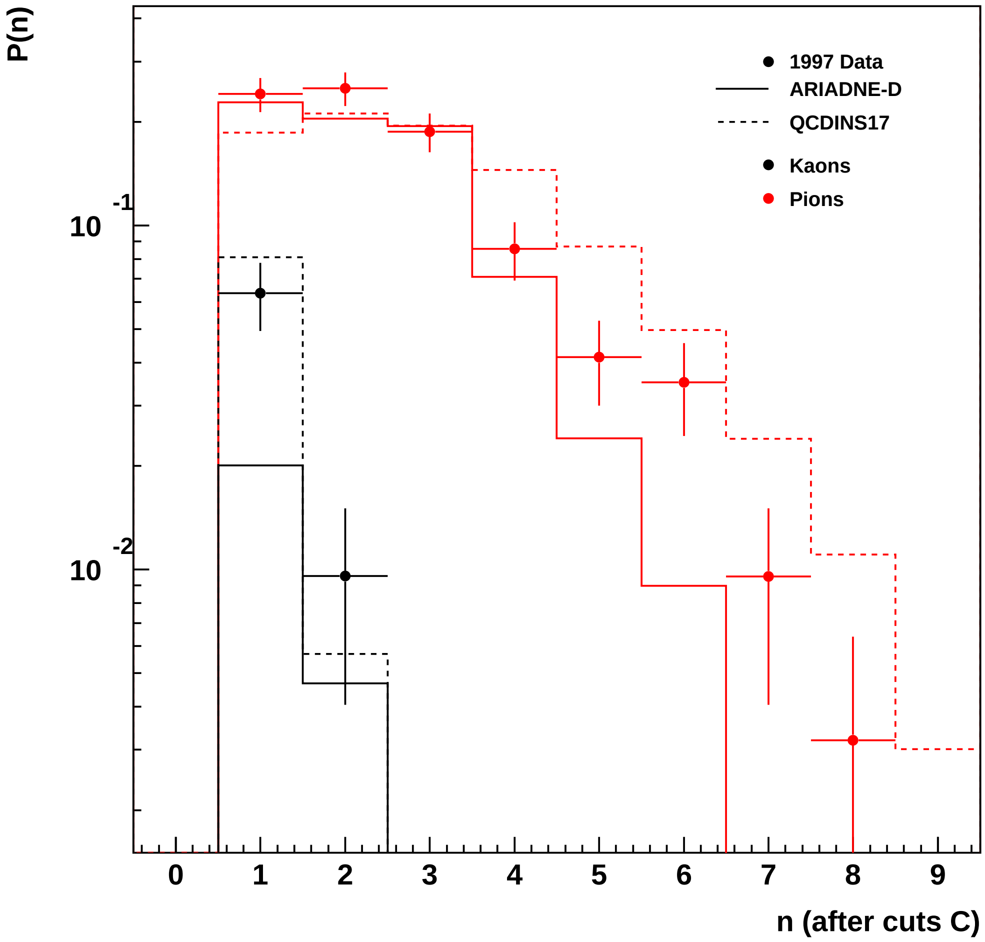

Figure 6.26: *Kaon and pion multiplicity after cut scenario C. 1996 data, ARIADNE-D and QCDINS17 Monte Carlo models shown.*

Chapter 7

Summary

Using the dE/dx technique, the first measurements at H1 of identified charged kaons, pions and protons in low Q^2 deep-inelastic ep scattering have been presented. Results obtained from the kaon studies have also been presented elsewhere [60].

Measurements have been presented of; charged kaon, pion and kaon/pion ratio transverse momentum and pseudo-rapidity spectra in the H1 proton-photon centre of mass frame in the kinematic region, $5 < Q^2 < 70$ GeV, $10^{-5} < x < 10^{-2}$, $0.1 < y < 0.6$ in 7 Q^2, x bins; proton transverse momentum and pseudo-rapidity spectra in the H1 laboratory frame in the same kinematic region and bins; the proton-antiproton asymmetry $A_B = \frac{2.(N_p - N_{\bar{p}})}{N_p + N_{\bar{p}}}$ transverse momentum, total momentum, pseudo-rapidity and charged track multiplicity spectra in the H1 laboratory frame in the same kinematic region. Also, measurements and spectra of the kaon/pion ratio have been made after applying a variety of cuts designed to enhance the possible signal due to QCD instanton induced interactions.

From the kaon and pion spectra, comparisons with different Monte Carlo models showed a sensitivity in the data to both the fragmentation and parton evolution processes involved in the DIS process. The 'BFKL-like' colour dipole model of ARIADNE was preferred over the parton showering process of LEPTO. Values for parameters in JETSET tuned to DELPHI data, including the strangeness suppression value, were preferred over the LUND default values. The HERWIG model, using the cluster fragmentation process, failed to predict these spectra in shape or yield. No significant changes in agreement with any of the models were found in the different kinematic regions studied, and the shapes of the distributions were not found to alter by much.

The proton and antiproton spectra were over-estimated by all the models, although the shape was in general modelled correctly. Again, no changes in agreement were found in the different kinematic regions studied, and the shapes of the distributions were found to change only a little. This over-estimation of the Monte Carlo predictions could be due to the suppression of baryonic production in fragmentation due to octet-anti-octet states at the parton level in these low-x regions dominated by gluon radiation.

Measurements of the proton-antiproton asymmetry were found to be in agreement with the photo-production measurement and theoretical prediction from studies involving gluonic propagation of baryon number over large rapidity intervals. However, given the large experimental uncertainties present in this analysis, no firm statement of asymmetry measurement was possible. Of the measured spectra of this variable, the total momentum spectra agreed with the photo-production measurement and the theory, in that A_B was found to decrease with total momentum. No increase with track multiplicity was observed however, although the results are not significant enough to be in contradiction with the other measurement and the theory.

After introducing cuts chosen to enhance the possible signature due to QCD instanton induced reactions within DIS; an increase in strangeness was observed from measurements of the kaon/pion ratio, this was not, however, significant to the 2σ level due to the low statistics arising from the harsh cuts applied. The instanton Monte Carlo model QCDINS, in this region of phase space also did not predict a higher than measured strangeness content of the charged hadronic final state. It is expected that the QCDINS model is very likely to be wrong here, however, for a number of reasons. Firstly, the model does not implement any quark flavours heavier than s, whereas real instanton interactions are expected to contain all quark flavours leading to a higher strangeness content of the final state. Also, QCDINS is based on the HERWIG model which described the other results poorly. Finally, due to the extremely dense initial partonic state of the instanton decay, it is likely that the standard fragmentation/hadronisation treatment is incorrect and perhaps some kind of quark-gluon plasma inspired model may be more accurate. With the increase of the theoretical understanding of instanton processes, hopefully these results may become more significant in the future.

Bibliography

[1] H1 Collaboration, I. Abt et al., Phys. Lett. 444 B (1995) 195.

[2] F. Halzen and A. D. Martin, Quarks and Leptons, Wiley & Sons, New York 1990.
M. Kuhlen 'QCD and the Hadronic Final State in Deep Inelastic Scattering at HERA', *Habilitationsschrift, Hamburg University Dec. 1997*, hep-ph/9712505 Dec. 1997.

[3] M. Gell-Mann, Phys. Lett. 8 (1964) 214.

[4] R. P. Feynman, Phys. Rev. Lett. 23 (1969).

[5] M. Breidenbach et al., Phys. Lett. 8 (1964) 214.

[6] F. Eisele, Invited talk at XVIII Physics in Collision, Frascati, Italy, 1998; hep-ex/9807028.

[7] V. N. Gribov and L. N. Lipatov, Sov. J. Nucl. Phys. 15 (1972) 438 and 675;
Yu. L. Dokshitzer, Sov. Phys. JETP 46 (1977) 641;
G. Altarelli and G. Parisi, Nucl. Phys. 126 (1977) 297.

[8] E. A. Kuraev, L. N. Lipatov and V. S. Fadin, Sov. Phys. JETP 45 (1972) 199;
Y. Y. Balitsky and L.N.Lipatov, Sov. J. Nucl. Phys. 28 (1978) 822.

[9] B. A. Kniehl et al., Nucl. Phys. B582 514-536 (2000).

[10] P. Aurenche et al., Eur. Phys. J C13 347-355 (2000).

[11] R. K. Ellis, W. J. Stirling and B. R. Webber, QCD and collider Physics, Cambridge University Press, Cambridge, 1996.

[12] G. Gustafson and Ulf Petterson, Nucl. Phys. B 306 (1988);
G. Gustafson, Phys. Lett. B 175 (1986) 453;
B. Andersson, G. Gustafson, L. Lönnblad, Ulf Petterson, Z. Phys. C 43 (1989) 625.

[13] T. Sjöstrand, Comp. Phys. Comm. 39 (1986) 347;
T. Sjöstrand and M. Bengtsson, ibid. 43 (1987) 367.

[14] A. K. Wróblewski, Proc. of the 25th Intern. Conf. on HEP, Singapore 1990, eds. K. K. Phua and Y. Yamaguchi, p. 125.

[15] JADE Collaboration, W. Bartel et al. , Zeit. Phys. C20 (1983) 187;
TASSO Collaboration, M. Althof f et al. , Zeit. Phys. C27 (1985) 27;
HRS Collaboration, M. Derrick et al. , Phys. Rev. D35 (1987) 2639;
HRS Collaboration, S. Abachi et al. , Phys. Rev. D41 (1990) 2045;
CELLO Collaboration, H. J. Behrend et al. , Zeit. Phys. C46 (1990) 397;
TASSO Collaboration, W. Braunschweig et al. , Zeit. Phys. C47 (1990) 167;
OPAL Collaboration, G. Alexander et al. , Phys. Lett. B264 (1991) 467.

[16] EMC Collaboration, M. Arneodo et al. , Zeit. Phys. C34 (1987) 283.

[17] A. Belavin, A. Polyakov, A. Schwarz and Yu. Tyupkin, Phys. Lett. B59 (1975) 85.

[18] I. I. Balitskii and V. M. Braun, Phys. Lett. B314 (1993) 237.

[19] A. Ringwald and F. Schrempp, DESY 94-197, hep-ph/9411217, Proc. of Int. Sem. 'Quarks 94', Vladimir, Russia, 1994, eds. D. Y. Grigoriev et al. , P. 170.

[20] A. Ringwald and F. Schrempp, DESY 96-203, hep-ph/9610213, Proc. IXth Int. Sem. 'Quarks 96', Yaroslavl, Russia, 1996.

[21] S. Moch, A. Ringwald and F. Schrempp, DESY 96-202 hep-ph/9609445.

[22] A. Ringwald and F. Schrempp, DESY 97-115, hep-ph/9706399, Proc. Workshop DIS97, Chicago 1997, eds. J. Repond and D. Krakauer.

[23] B. Andersson, G. Gustafson and T. Sjöstrand, Physica Scripta 32 (1985) 574.

[24] Y. Eylon and H. Harari, Nucl. Phys. B80 (1974) 349.

[25] B. Alper et al., Nucl. Phys. B100 (1975) 237.

[26] T. Akesson et al., Nucl. Phys. B228 (1983) 409.

[27] NA35 Collaboration, H. Ströbele et al., Nucl. Phys. A525 (1991) 59.

[28] H1 Collab., Conf. paper 556, 29th intern. Conf. on High-Energy Physics, Vancouver, Canada (1998).

[29] V. Artry, Nucl. Phys. B85 (1975) 442.

[30] G. C. Rossi and G. Veneziano, Nucl. Phys. B123 (1977) 507; Phys. Rep. 63 (1980) 149.

[31] G. T. Garvey, B. Z. Kopeliovich and B. Povh hep-ph/0006325.

[32] B. Z. Kopeliovich and B. Povh, Z. Phys. C75 (1997) 693.

[33] G. Ingelman, DESY-88-014, Invited talk given at 4^{th} INFN Workshop in Very High Energy Proton-Proton Physics, Erice, Italy, May 1987.

[34] HERA, A Proposal for a Large Electron Proton Colliding Beam Facility at DESY, DESY HERA 81-10 (1981).

[35] http://www.desy.de.

[36] H1 collaboration, Technical Proposal for the H1 Detector (1986); H1 Collaboration, The H1 Detector at HERA, DESY 93-103 (1993), Updated version: DESY H1-96-01 (1996).

[37] ZEUS collaboration, The ZEUS detector, Technical Proposal (1986); ZEUS Collaboration, The ZEUS Detector, Status Report (1989).

[38] W.Hoffmann,'An Experiment to Study CP Violation in the B System using an Internal Target at the HERA Proton Ring', DESY-PRC 94/02 (1994).

[39] HERMES Collaboration. A proposal to measure the spin-dependent structure functions of the neutron and proton at HERA (1990).

[40] H. Bethe, and W. Heitler, Proc. Roy. Soc. A146 (1934) 83.

[41] S. Egli et al., Guide to the simulation program H1SIM, H1 Document (1991).

[42] R. Brun et al., GEANT long writeup, CERN Program Library, W5103 (1989).

[43] European phys. Journal C Rev. Part. Phys. (1998) 25.9 160.

[44] B.Rossi, High Energy particles, Prentice-Hall, Inc., Englewood Cliffs, NJ, 1952.

[45] Thesis II.Exp.Phys.Inst. Univ. Hamburg 4/99 J. Steinhart 'Die Messung des totalen ccquer-Photopro-duktions-Wirkungsquerschnittes durch die Rekonstruktion von Lambda-c-Baryonen unter Verwendung der verbesserten dE/dx-Teilchen-identifikation am H1 Experiment bei HERA'.

[46] B. Rossi, High Energy Particles, Prentice Hall Physics series, Chap.2.

[47] V. A. Lubimov, G. P. Eliseev and V. K. Kosmachevskii, lzvestija AN SSSR (Ser.Phys.) **19** (1955) 753.

[48] Statistics for Physicists, B. Martin.

[49] R. M. Sternheimer and R. F. Peierls, Phys. Rev, B3:3681, 1971.

[50] R. Engel, Z. Phys. C66 (1995) 203;
R. Engel and J. Ranft, Phys. Rev. D54 (1996) 4244.

[51] G. Ingelman, A. Edin and J. Rathsman, Comp. Phys. Comm. 101 (1997) 108.

[52] G. Marchesini et al., Comp. Phys. Comm. 67 (1992) 465;
M. H. Seymour, Nucl. Phys. B436 (1995) 443.

[53] L. Lönnblad, Comp. Phys. Comm. 71 (1992) 15.

[54] H. Jung, Comp. Phys. Comm. 86 (1995) 147

[55] DELPHI Collaboration, P. Abreu et al., Zeit. Phys. C65 (1995) 587.

[56] H1 Collab., DESY 96-122, hep-ex/9607010.

[57] T. Carli, J. Gerigk, A. Ringwald and F. Schrempp, DESY 99-067, hep-ph/9906441.

[58] H1 Collab., “Search for QCD Instanton Induced Events in Deep-Inelastic Scattering at HERA”, cont. paper to ICHEP2000, abstract 972.

[59] A. Ringwald and F. Schrempp, to be published in Comp. Phys. Commun. (1999), hep-ph/9911516.

[60] H1 Collab., Contributed Paper 157h, International Europhysics Conference on High Energy Physics (HEP99), Tampere, Finland, July 1999